

## Chapter 2

# Experimental and Model Spatiotemporal and Spatial Patterns in Electrochemical Systems

### 2.1 Simple Examples of Dissipative Pattern Formation

In Chaps. 4–6 of volume I, we analyzed the experimental manifestations and the relevant models of temporal dynamic instabilities, i.e., oscillations and multistability characterized by the total (average) current or the potential of the working electrode. In the present chapter, we describe the spatiotemporal and spatial patterns that develop due to nonlocal and global couplings, according to theoretical background outlined in Sect. 1.2. This means, among others, that in the formation of such patterns the inhomogeneous distribution of the electric field at the interface, causing *migration* currents flowing parallel to the electrode surface, will be taken into account. Also, the role of *diffusion* in generating a particular type of patterns will be described. Concerning another type of transport, the *convection* can also be a source of spatial self-organization in electrochemical systems due to its possible self-organized nature under appropriate conditions. However, the patterns of convective origin will be described separately in Chap. 5, as the mechanism of their formation is different from those operating in the case of diffusion–migration systems. Thus, for the purposes of the present chapter we shall assume that the convection does not exist or at least does not play any significant role in the pattern formation discussed. As indicated in Sect. 1.2, the substantial progress in understanding the mechanisms of the formation of such nonconvective dissipative patterns took place only in recent decades, when this challenging task was undertaken by the Berlin group, gathered around Ertl, Krischer, and coworkers in the Fritz-Haber Institute of Max-Planck Society. The success of these investigations was possible not only because of the development of appropriate theory, but also due to employing the modern techniques of analysis of the state of surfaces, as the surface plasmon spectroscopy [1].

Before description of recent achievements in this area, let us mention and comment selected historical examples of spatiotemporal patterns in electrode processes. In 1948, Bonhoeffer has published the paper [2]: “Activation of passive iron as a model for the excitation of nerve.” The title referred to the experimental fact that if a piece of passivated iron immersed in concentrated nitric acid is touched

momentarily with a zinc rod, the iron may become active and the zone of activation will spread over the whole piece of iron. The final state of iron, i.e., active or passive, depends on the concentration of nitric acid (repassivation occurs for intermediate concentrations). In a more sophisticated version of this experiment, when the iron wire was used, and for that intermediate acid concentration, one might observe a spreading wave front of activation, followed by a spreading wave front of repassivation. But in fact, as Bonhoeffer remembers in his paper, this impressive phenomenon was first reported already by Wilhelm Ostwald around 1900 who also suggested that its course resembles the progress of excitation of nerve. Inspired by Ostwald, Heathcote has studied this phenomenon more thoroughly [3, 4] and has found that the iron could not be reactivated if one touched it with zinc rod just after repassivation, but after certain delay, just like the nerve after excitation exhibits certain “dead,” or refractory period, typical of *excitable* characteristics (see Sect. 1.1.2). These analogies were later analyzed by Lillie (cf. e.g., [5–7]) who has reported, among others, the dependence of the velocity of the active zone propagation on the thickness of the surrounding layer of electrolyte, indicating in this way the role of local currents.

Today, we of course know that properties of the Fe/HNO<sub>3</sub> system and the principle of the nerves conductivity are based on very different detailed mechanisms. Concerning the latter process, its most famous four-variable theoretical model, formulated by two Nobel Prize winners A. L. Hodgkin and A. F. Huxley (1952), was based on the various permeability of K<sup>+</sup> and Na<sup>+</sup> ions through the membrane of the neural cell. Due to complexity of the original approach, the mathematically more tractable version, reduced to two dynamic variables, was later elaborated by R. FitzHugh and J. S. Nagumo (cf. e.g., [8, 9]). For the case when the neural cell is not perturbed by external current, but the diffusion associated with axial current in the axon is considered, the following system of equation was derived [9]:

$$\frac{\partial u}{\partial t} = f(u) - v + D \frac{\partial^2 u}{\partial x^2} \quad (2.1)$$

$$\frac{\partial v}{\partial t} = bu - \gamma v \quad (2.2)$$

where:

$$f(u) = u(a - u)(u - 1) \quad (2.3)$$

$u$  is directly related to the membrane potential,  $0 < a < 1$  and  $b$  and  $\gamma$  are positive constants. The course of nullclines of (2.1) and (2.2) reveals typical excitable characteristics (cf. Sect. 1.1.2).

It is appropriate here to indicate the basic weakness of this approach which assumes only diffusion as the cause of the propagation of neural excitation, while in this process there are involved ions placed in the inhomogeneous electric field. Therefore, the coefficient  $D$  in (2.1) is rather an *effective* transport coefficient, named

also sometimes the “diffusion” coefficient [9]. Neglecting the obvious contribution from migration in a strict way relating its rate to the gradient of electric field does not allow us to estimate correctly the rate of the impulse propagation along the neuron. In this context, the recent developments of understanding the pattern formation in electrochemical systems, when migration is considered an essential transport, offer a chance to a progress in a more quantitative model of neural systems.

But today we also realize that completely different systems, if defined in terms of appropriately chosen mathematical equations that reflect the “core” of their nonlinear dynamics, exhibit striking qualitative similarities or universalities. The above-mentioned excitability, observed for both the onset of traveling zone of activity on a passivated iron wire and the excitation of propagating nerve impulse, is a good example of that. Later, Bonhoeffer confirmed the excitable characteristics of the passivated iron system: the assembled electrochemical system consisted of Fe wire (cathode) and Pt wire (anode) dipped in nitric acid and connected to the external power source producing current pulse of desired magnitude and duration. For nitric acid of sufficiently high concentration, the Fe wire became strongly passivated and then its activation (followed by repassivation) was induced by the current pulse, but only if the electric charge injected exceeded certain threshold value. The refractory state after the activation was also observed and explained as due to the formation of nitrous acid which removal from the electrode environment required some time, and also due to the formation of oxide layer on the iron surface after its repassivation, which disappeared gradually during the period of recovery of the ability to the next activation. The next important step in developing the studies of this phenomenon was described by Franck [10]. In the experimental arrangement shown in Fig. 2.1, it was possible to monitor the propagation of the activation zone on the surface of Fe wire immersed in the solution of either  $\text{HNO}_3$  or  $\text{H}_3\text{PO}_4$ . In fact, these works can be considered the precursors of later serious studies of spatiotemporal patterns on the electrode surfaces.

More recently, studies of spatiotemporal propagation of the electrochemical reaction along an iron electrode in sulfuric acid solution have been undertaken by Nakabayashi et al. [11, 12] in order to correlate the current oscillations with the development of a spatiotemporal pattern on the electrode surface. The propagation of the reaction front of an oxide formation and reduction along the iron wire was monitored by means of a 16-channel platinum potential probe array. A pulse of the current oscillation was found to consist of both a sequential propagation of the oxide reduction, which makes the rise of the current, and a random formation of the oxide at the electrode surface for current decay. The traveling velocity of the oxide reduction increased as the potential of iron electrode became more cathodic. An important observation was that the oscillation waveform and the propagation speed of the reduction front were changed if serial resistance was inserted in the circuit. Moreover, if the propagation was blocked, e.g., by an insulator coating of the electrode, the rising current was disturbed and modulated, having independent occurrence of the reduction propagation at each separated branch of the electrode. These results suggested a coupling between the ohmic potential drop in the solution and the reaction propagation along the electrode surface [12] and are further developed in

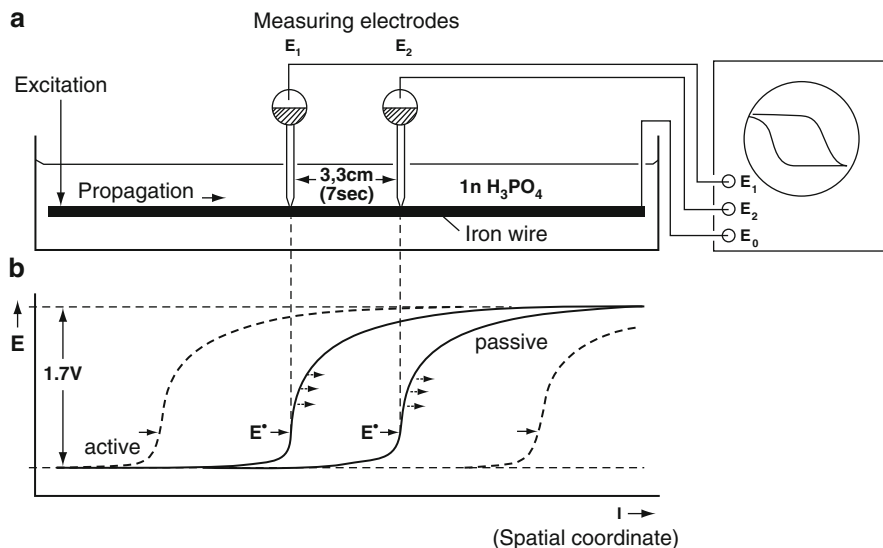


**Fig. 2.1** An example of the instability-driven propagation of activation zone along the passivated iron (a) experimental setup and (b) local profiles of the electric potential associated with the passage of the activation wave through both sensing electrodes. Reprinted with translation into English from [10], with kind permission of Deutsche Akademie der Naturforscher Leopoldina—Nationale Akademie der Wissenschaften

Sect. 3.1.4, devoted to coupled Fe/H<sub>2</sub>SO<sub>4</sub> oscillators. The works cited earlier include also instructive spatiotemporal maps of the propagation of the oxide reduction along the iron electrode, correlated with the shape of the oscillatory peak.

For a chemically similar system, consisting of low-carbon steel plates, covered with thin (0.5 mm) layer of oxygen-containing nitric acid, inducing the corrosion, Agladze, Steinbock et al. [13, 14] have described the development of two-dimensional patterns in the form of pulses, rotating spirals, and serpentes, propagating with the velocity of the order of millimeters per second. The corrosion could be initiated locally by breaking the passivation film or, as in classical Bonhoeffer experiments, by touching the surface of the plate with a zinc rod for ca. 1 s. These patterns could be observed visually as traveling brownish bands on the passivated grayish steel. Generally, the pattern formation in the Fe–HNO<sub>3</sub> reaction system depended significantly on the concentration of nitric acid. The morphology of spiral waves resembled analogous phenomena for the excitable Belousov–Zhabotinsky system, however with a striking quantitative difference: in the Fe–HNO<sub>3</sub> system, the recovery times were substantially shorter than excitation times.

The simplest chemical mechanism underlying dissolution of propagating waves in the above Fe–HNO<sub>3</sub> system is the following [13]. In contact with concentrated HNO<sub>3</sub>, the dissolution of Fe is hindered due to formation of passivating surface film which contains considerable amount of water of hydration. The local damage of this film causes the Fe oxidation to Fe<sup>2+</sup> and this triggers the flow of Fe<sup>2+</sup> ions into the nearby solution layer. In this way, the local electrochemical cell is formed in which

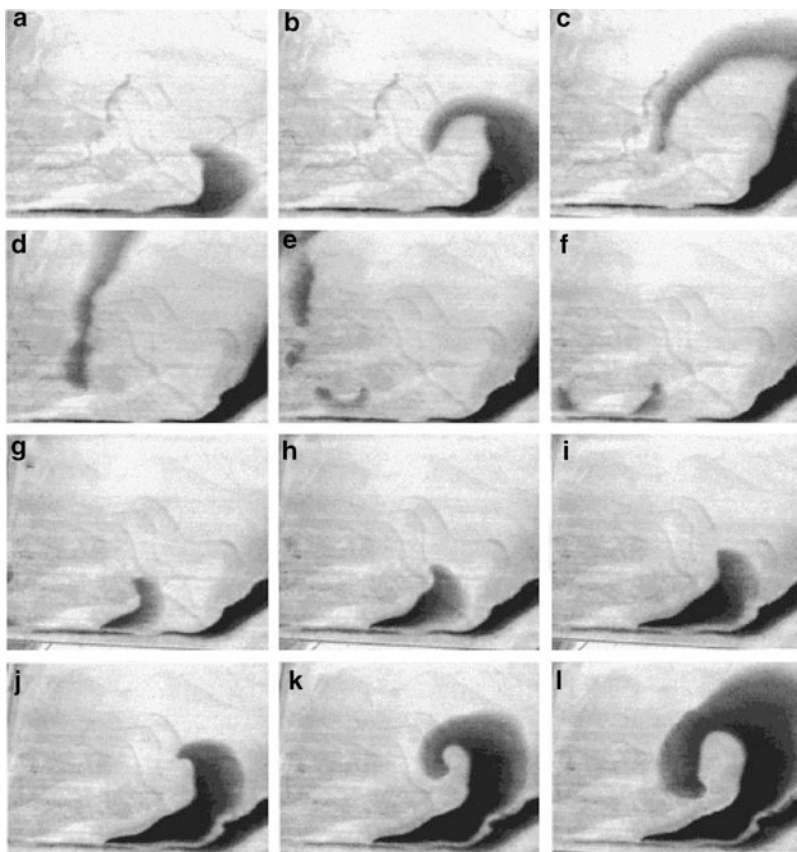
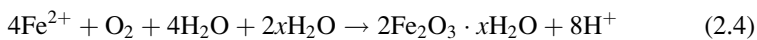
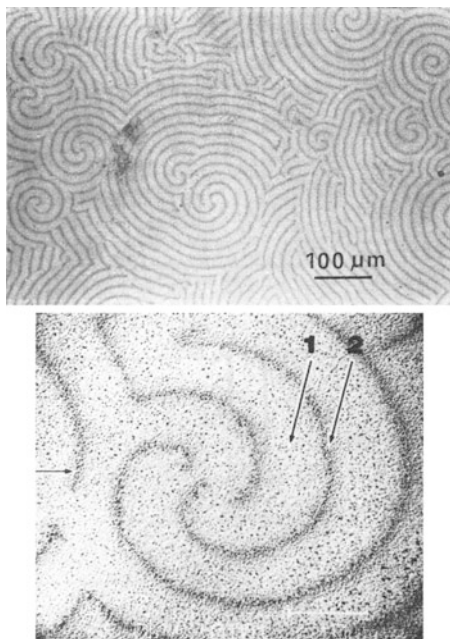


**Fig. 2.2** Propagation of waves and rotation of spirals in the iron–nitric acid system. The sequence shows 12 consecutive snapshots of the steel surface obtained at 0.7 s intervals. The wave is initiated at the lower left corner of the horizontal steel plate a few seconds prior to the snapshot (a). Under the given experimental conditions, the spiral waves have a rotation period of approximately 6 s. Experimental parameters: 11.9 M nitric acid; temperature of the solution and steel plate, 0 °C; thickness of the solution layer 0.5 mm; field of view:  $5.9 \times 4.6 \text{ cm}^2$ . All experiments are carried out with low-carbon steel under open circuit conditions. Reprinted with permission from [13]. Copyright 2000 American Chemical Society

the local defect in the passivation film is the anode. In consequence, the  $\text{H}^+$  ions migrate away from this area, in order to meet the electroneutrality condition. The local increase in pH destabilizes the adjacent passivation film and additional  $\text{Fe}^{2+}$  is released into the solution. The spatiotemporal progress of this process means the formation of the traveling wave. Noteworthy, this process is again dynamically similar to the nerve excitation. The difference lies in the recovery process. In the  $\text{Fe}/\text{HNO}_3$  system, this recovery is due to pH equilibration between the bulk solution and a thin layer adjacent to the dissolving surface. Also, in order to explain the formation of visually observed rust, one has to take into account the key role of dissolved oxygen in the recovery process:

**Fig. 2.3** *Top*: The surface of a silver-antimony alloy coating deposited at current density  $1.3 \text{ A dm}^{-2}$ ; *bottom*: Surface region of the alloy coating deposited at current density  $1.3 \text{ A dm}^{-2}$ . Secondary electron image. Concentration of antimony in the electrolyte: 0.04 M. Reprinted from [17], Copyright 1989, with permission from Elsevier



Further examples of patterned Fe electrodisolution include, among others, the spatiotemporal period doubling for a circular Fe electrode in contact with 1 M  $\text{H}_2\text{SO}_4$  electrolyte [15]. An attempt to model the spiral waves in this type of systems was described by Koper and Sluyters [16]. Spiral patterns were experimentally observed by Kristev et al. [17] for electrodeposition of Ag–In or Ag–Sb alloys within the range of limiting current, under galvanostatic conditions (Fig. 2.3).

In turn, Gladyshev and Kovaleva [18] have described patterns associated with the anodic oxidation of ternary amalgams, composed of mercury, dissolved alkaline metal and its hydride, formed during parallel electroreduction of alkali metal ions and hydrogen ions on mercury cathode. Anodic polarization of such amalgams causes hydrogen evolution with the formation of dispersed bubbles in the mercury phase. Under appropriate conditions of anodic oxidation, the chaotic oscillations ( $f = 0.5\text{--}2 \text{ Hz}$ ) imposed on the basic, monotonously increasing current were observed and, simultaneously, on the mercury surface one observed circular, concentric waves, running from the center to the peripheral zone of the electrode. The circular patterns were surrounded with very fine hydrogen bubbles. It is possible that nucleation and evolution of hydrogen bubbles in the mercury phase is responsible for the formation of these patterns.

As mentioned earlier, the theoretical treatment of the dissipative spatial or spatiotemporal electrochemical patterns was outlined in Sect. 1.2. The main point

is that between different sites of the electrode there emerge spatial couplings, obviously dependent on cell geometry, which have to be taken into account, in addition to the criteria of instability existing for spatially homogeneous systems. A concise summary of possible couplings is given below. There are two principal modes of the spatial coupling. A first type is the *migration coupling*. If the distribution of the electric potential was ideally homogeneous, the vector of migration of charge carriers would be oriented only normal to the electrode surface (this normal direction will further be assumed as concordant with the direction of  $z$  axis of the Cartesian coordinate system). However, if different sites of the electrode differ with the local electric potential, the local migration currents exhibit also corresponding spatial distribution. The vector of migration of ions acquires now the components parallel to the electrode surface ( $x, y$  directions), since the current flows in those directions due to the local difference in electric potentials. In this way different sites of the electrode do not remain independent, but become coupled through the migration. Such coupling has substantial consequences: if the working electrode potential (interfacial potential drop) changes at a certain position, it will affect the distribution of the potential across the entire electrolyte. This, in turn, will change the local migration current densities at the working electrode. One should emphasize that migration coupling is termed “nonlocal” one, in order to emphasize its greater extent, compared to only local nature of diffusion coupling. On the other hand, the closer the counter electrode (CE) to the working electrode (WE), the more localized becomes this coupling.

The second type of coupling, named the *global coupling* between different sites of the electrode surface, is caused by the feedback in the electronic circuit, working either in the potentiostatic or galvanostatic mode, determining the different particular feedback mechanism. For the *galvanostatic* operation mode, any local fluctuation of the faradaic current at the electrode surface changes the imposed fixed total current. In order to compensate for this difference, the galvanostat provides the additional, charging (capacitive) current which causes the change of the working electrode potential. In this way, all the electrode sites become affected with the initial small fluctuation of the current, therefore this mode of coupling is indeed global in nature. In the *potentiostatic* operation mode, the local fluctuation of the working electrode potential affects the distribution of the electric potential in the entire electrolyte, so also at the position of the reference electrode (RE). The potentiostat feels this alteration as the deviation of the electrode potential from the programmed fixed value and charges the WE electrode to a new value, changing the entire distribution of the electric potential throughout the solution. If the WE and RE electrodes are of the same size and parallel to each other, the entire WE surface experiences the change of the potential, meaning the global nature of the effect. In a more realistic case, the analogous situation is obtained in this way that the working electrode is a thin annulus, and the reference electrode is located on the axis of the ring. In spite of certain similarity in the mechanism of the creation of the global coupling under both operation modes, there is between them a very important difference from the dynamical point of view. In the galvanostatic mode, due to global coupling

the interfacial potential drop of various electrode sites becomes equalized. In the potentiostatic mode these differences are amplified. Therefore for the galvanostatic mode, the *synchronization* of various sites occurs and we call that situation an effect of the *positive global coupling*, leading to the stabilization of the electrode state. For the potentiostatic mode, the opposite effect—desynchronization means *negative global coupling*, destabilizing the electrode state. The latter effect is particularly strongly pronounced if WE and RE are positioned close to each other, as in the case of application of a Haber-Luggin capillary, minimizing the ohmic potential drop between WE and RE [19–21]. In fact, Otterstedt, Hudson et al. [27] were the first who reported such spatiotemporal phenomena for the anodic dissolution of Co (see Sect. 2.3). The Co electrode had a shape of a disk or a ring and the tip of the Luggin capillary was placed in its center. In conclusion, the dependence of the range of the coupling on the cell geometry means that it can be tuned experimentally by variation of the relative positions and shapes of the working, reference, and counter electrodes.

Finally, the interactions between various couplings and the negative differential characteristics (of N-NDR or S-NDR type) may give rise to different spatiotemporal or spatial patterns. These theoretical backgrounds will now be illustrated with appropriate experimental examples.

## 2.2 Patterns in $\text{S}_2\text{O}_8^{2-}$ Electroreduction

From Sect. 4.1 of volume I we know that the electroreduction of  $\text{S}_2\text{O}_8^{2-}$  is an example of the process with the N-NDR characteristics in the current–potential response. In other words, it is a system of the activator–inhibitor type, in which the electrode potential is an activator (autocatalytic variable) and the chemical variable (concentration of the electroactive species) is an inhibitor, engaged in the slow negative feedback loop. Pattern formation occurs if such process is coupled to migration. More precisely, this interplay engages the activator—the electrode potential which due to migration flows along the electrode surface. Under such conditions, the pulses or spiral waves, propagating over long distances without attenuation, are generated. The model case of the propagation of the pulse in an electrochemical bistable system was shown in Fig. 1.17. One should also remember that, contrary to the reaction–diffusion systems (RDS), when the stationary traveling fronts move with constant velocity, in the electrochemical systems of the above characteristics the acceleration of the front was reported. This acceleration was experimentally observed, e.g., for the peroxodisulfate reduction at the rotating ring Ag electrodes, being the first experimental evidence for such phenomenon [22]. The experimental setup is shown in Fig. 2.4.

The measurements were made for the bistable region of the  $\text{S}_2\text{O}_8^{2-}$  electroreduction, i.e., for the coexisting high-current (active) and low-current (passive) states. The potential microprobes measured the potential in front of the electrode as a function of the angle and time. Figures 2.5, 2.6 clearly show the acceleration in

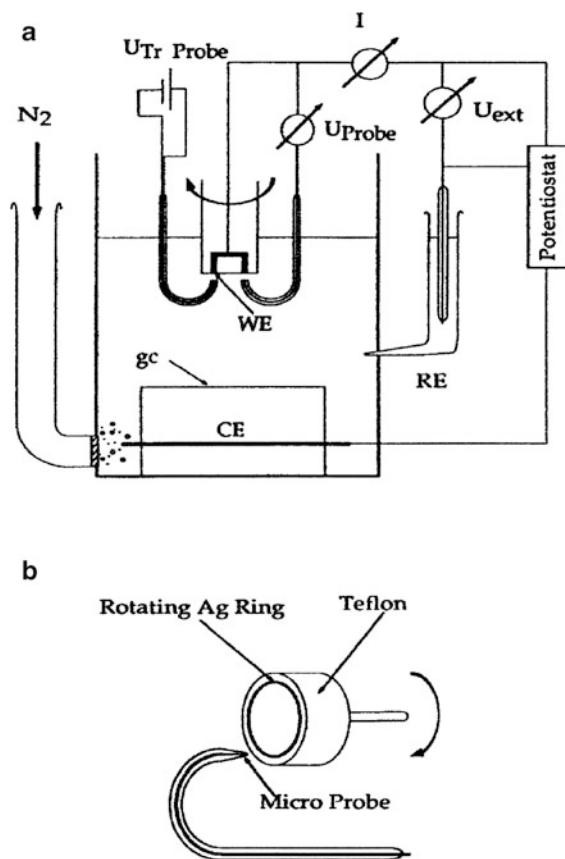


**Fig. 2.4** (a) Scheme of the experimental setup; WE working electrode, CE counter electrode, RE reference electrode (standard calomel electrode), gc glass cylinder. Between WE and RE the voltage  $U_{\text{ext}}$  was held constant. The local potential in front of WE was measured by two micropotential probes. In some experiments one of them was exchanged by a trigger probe. (b) Enhanced sketch of working electrodes and microprobes. Reprinted with permission from [22] <http://link.aps.org/abstract/PRE/v51/p3997>. Copyright 1995 by the American Physical Society

the propagation of the front, formed as a result of transition from the passive to the active state.

The role of migration coupling in the acceleration of the front was experimentally proved by the reported increase in the average front velocity with increasing solution conductivity ( $\sigma$ ).

The fact that oscillations and transitions in the bistable regime of the  $\text{S}_2\text{O}_8^{2-}$  electroreduction are associated with wave phenomena was further confirmed by the observations made by means of the surface plasmon spectroscopy [23] which also allowed to monitor the fast surface dynamics of this process. Onto one side of the glass prism of high refractive index, a 50-nm-thick Ag film was evaporated.

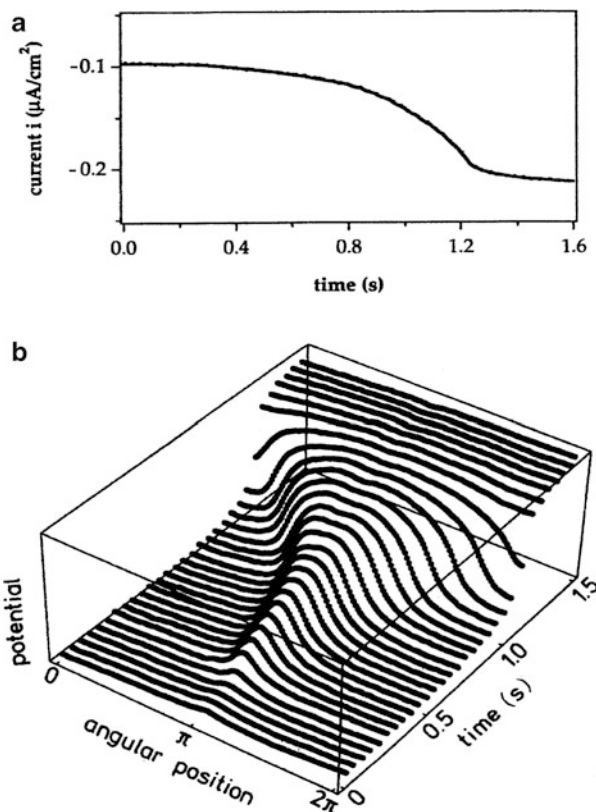


**Fig. 2.5** (a) Time series of the total current  $i$  and (b) spatiotemporal plot of the local potential during a transition from the passive (low current density) to the active (high current density) state in the bistable regime at  $U_{\text{ext}} = -1.36$  V,  $f = 20$  Hz,  $[\text{Na}_2\text{S}_2\text{O}_8] = 0.1$  mM,  $[\text{Na}_2\text{SO}_4] = 0.1$  mM, and pH 5. The circumference of the electrode is equal to 3.46 cm. Reprinted with permission from [22] <http://link.aps.org/abstract/PRE/v51/p3997>. Copyright 1995 by the American Physical Society

This Ag film served as a working electrode, whereas the glass prism permitted the excitation of surface plasmons by a p-polarized He–Ne laser beam which was passed through the prism onto the Ag film with a certain angle of incidence. The excitation of surface plasmon (SP) occurs in a narrow interval of the angle of incidence, at which the energy and momentum of the incoming photons and surface plasmons are matched. Experimentally, this excitation manifests itself as a strong decrease in intensity of the reflected laser beam. Furthermore, this phenomenon is potential dependent, so if the potential drop is different at two different locations at the electrode, the intensity of the reflected laser beam at a certain angle of incidence is also different. More precisely, for the system considered here, the intensity in the images is affected by the change in coverage of specifically adsorbing anions (which directly reflect the changes of the electrode potential) and a change in roughness (or a partial oxidation) of the Ag electrode.

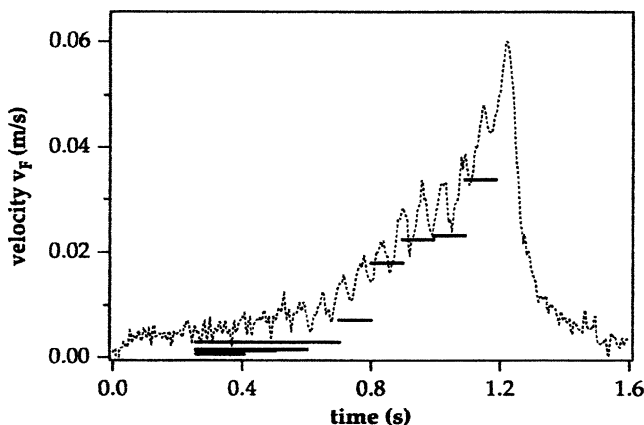


**Fig. 2.6** Front velocity versus time for the transition displayed in Fig. 2.5. The *bars* show the mean velocity obtained from the micropotential probes. The *dashed line* displays the velocity obtained from the derivative of the current shown in Fig. 2.5a. Reprinted with permission from [22] <http://link.aps.org/abstract/PRE/v51/p3997>. Copyright 1995 by the American Physical Society

Figure 2.7 shows exemplary comparison of the temporal variations of the current and the corresponding images, recorded by CCD camera, which illustrate the distribution of the interfacial potential drop. One notices that when the cathodic current of  $\text{S}_2\text{O}_8^{2-}$  reduction rises (at  $t = 48$  ms), a new state is formed in the lower right-hand corner of the electrode surface. As a function of time, this zone expands across the electrode and highest intensity of this phenomenon, occurring eventually almost homogeneously on the surface, is obtained some time after the moment at which the current passed through its maximum. Then the intensity slowly decreases. Although the interpretation of intensity images may contain some uncertainties, their analysis (including also studies in the bistable regime) led to conclusion that the characteristic length of the patterns was determined by the temporal dynamics of the potential drop across the double layer at high mass transport, and by the dynamics of the concentration of  $\text{S}_2\text{O}_8^{2-}$  at the electrode at low mass transport. Furthermore, the relatively high velocity of the fronts (from several  $\text{cm s}^{-1}$  to several  $\text{m s}^{-1}$ ) and their dependence on the uncompensated electrolyte resistance is a strong premise for the important role of migration transport in the spatial coupling as a cause for their spatial progress.

At this point it is useful to invoke an interplay of a negative global coupling, favoring the pattern formation and the, induced by this inhomogeneity, migration coupling that acts in an opposite direction. Then, in the case of bistable system, when one part of the electrode remains in the active state, and the other part in the passive state, the migration coupling initially predominates, being slightly opposed global coupling, but gradually increasing extent of negative global coupling may induce the situation when both couplings balance each other, giving rise to stationary patterns consisting of high and low potential domains [19]. An experimental

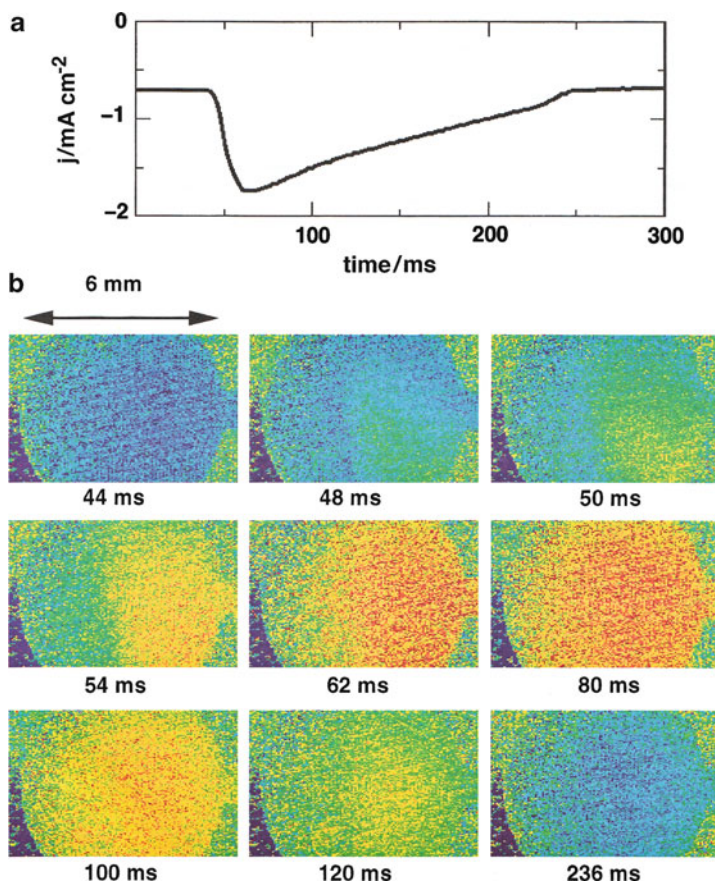


**Fig. 2.7** (a) Time trace of the global current during the oscillation (the oscillation frequency was about 2 Hz) (b) Images of the electrode during the oscillation obtained with the SP microscope. Electrolyte 2 mM  $\text{Na}_2\text{S}_2\text{O}_8$ , 0.1 mM  $\text{Na}_2\text{SO}_4$ , 0.1 M NaOH,  $\text{N}_2$  saturated, impinging jet stirring. Reprinted from [23], Copyright 1996, with permission from Elsevier

illustration of such interplay of couplings was reported by Grauel et al. [24] for the electroreduction of  $\text{S}_2\text{O}_8^{2-}$  at Ag ring electrodes, for the parameter values close to or corresponding to the bistable characteristics of that process, and with the Luggin-Haber capillary minimizing the ohmic potential drop. Figure 2.8 shows the distribution of the electrode potential, varying as a function of time, along the ring Ag electrode (i.e., for the angle varying from 0 to  $2\pi$ ).

Comparison of these maps with the  $I$ - $E$  characteristics of the  $\text{S}_2\text{O}_8^{2-}$  electroreduction shows that for the potential values lying within the N-NDR region (Figs. 2.8b, c), the potential distribution along the ring electrode is particularly inhomogeneous and takes a form of patterns, consisting of two domains, the one characterized with the relatively positive potential (“active” domain) and the other one—with the relatively negative potential (“passive” domain), compared to the

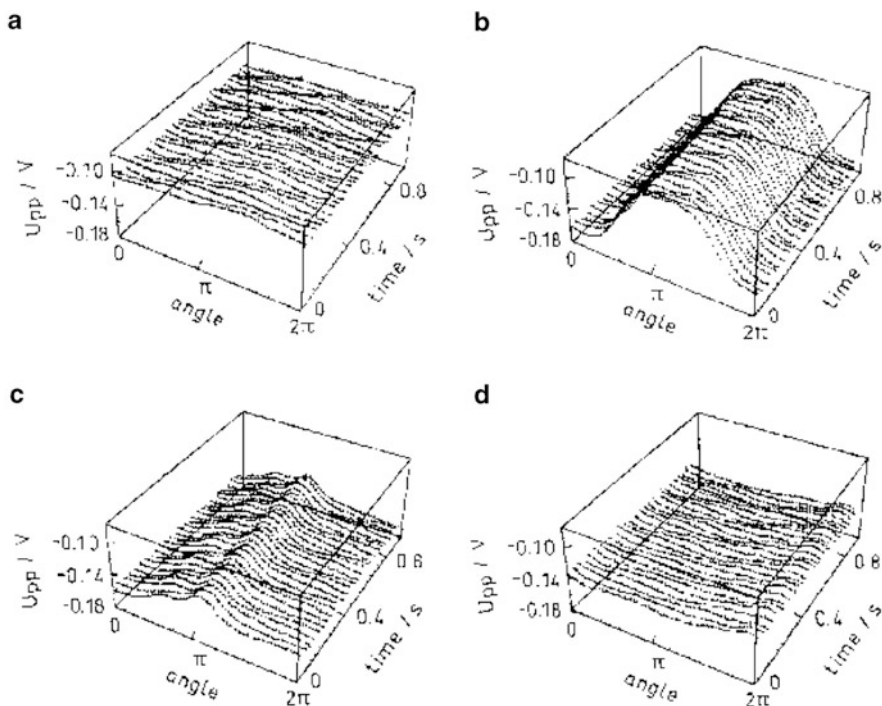


**Fig. 2.8** Space-time plot of the local potential measured at four different values of the external potential: (a)  $-1.2$  V, (b)  $-1.13$  V, (c)  $-1.1$  V, (d)  $-1.0$  V. Reprinted with permission from [24]. Copyright 1998 American Chemical Society

potential of the NDR region. Furthermore, if the voltage was kept constant, the patterns appeared to be stable, i.e., invariant with time.

It was also found experimentally that insertion of sufficiently large external resistor to the circuit of the working electrodes caused the disappearance of spatial patterns. This is because external serial resistor introduced a positive global coupling which counteracted the negative global coupling and thus the formation of patterns. These experimental results were successfully modeled in terms of the appropriate equivalent circuits, where variation of external resistance tuned the relative contribution of the negative and positive global couplings [24].

## 2.3 Patterns in Co Electrodeposition

Other experimental examples of the electrochemical accelerated fronts include the dissolution of Co [25, 26] and Fe [11, 12] (see Sect. 2.1) electrodes. We shall briefly describe here the phenomena reported for the dissolution of the ribbon cobalt electrodes in buffered phosphate solutions [26]. The experimental setup is shown in Fig. 2.9.

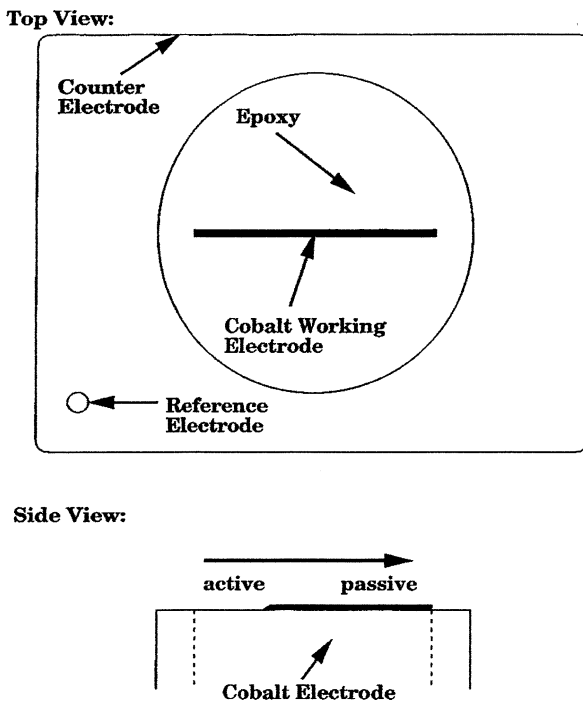


**Fig. 2.9** Top and side views of the experimental setup. Reprinted with permission from [26] <http://link.aps.org/abstract/PRE/v54/p3744>. Copyright 1996 by the American Physical Society

The saturated calomel reference electrode was used and the rectangular copper wire served as a counter electrode. In one of the experiments, the Co electrode was initially passivated by applying sufficiently positive potential which was then moved to the value more negative than the Flade potential. Due to slow rate of the film dissolution, the depassivation of the electrode would take some time, but it was locally accelerated by scratching the surface at one end of the ribbon. The particularly interesting sequence of dynamical events happened if the electrode potential was close to the Flade potential. The resulting small active region immediately began to move toward the center of the ribbon and another active region formed spontaneously at the other end of the electrode, also starting to propagate towards the ribbon center. When both fronts of active zones meet, they annihilate. Then, after a short delay, two new active regions form, one from each end of the ribbon, and they again propagate towards the center.

In one of the experiments corresponding to such conditions, the set of 12 auxiliary reference electrodes was placed along the Co ribbon which was initially passivated by applying sufficiently positive potential which was then stepped to the value slightly more negative than the Flade potential, and the ribbon electrode was locally activated by placing there the drop of acid. The development of spatiotemporal patterns, visualized as maps of equipotential lines, is shown in Fig. 2.10.

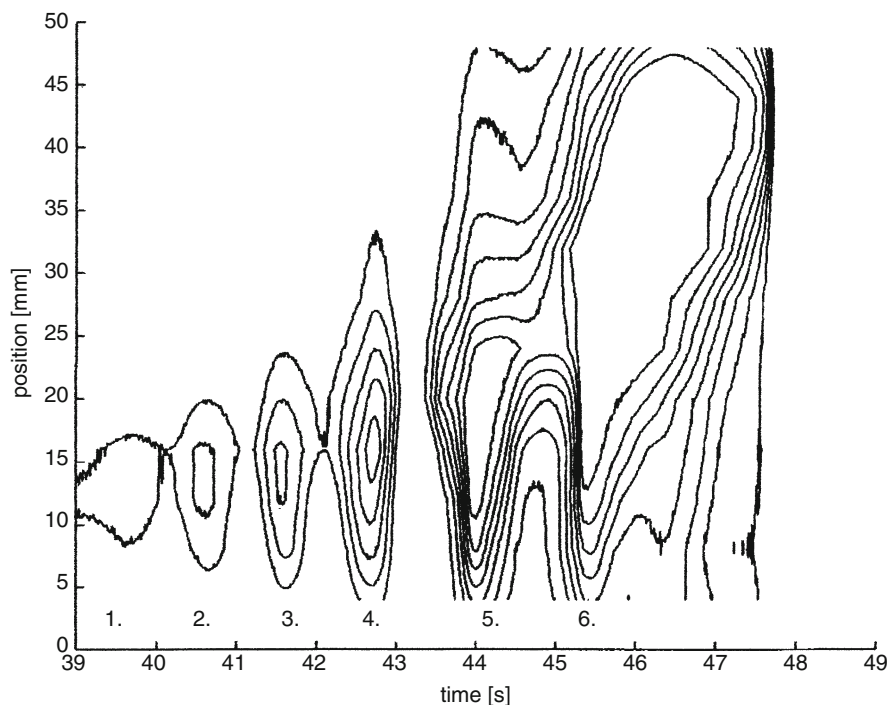


**Fig. 2.10** Position–time plot of selected equipotential lines as derived from the signals obtained from 12 auxiliary reference electrodes positioned equidistantly along the ribbon. Time denotes the time elapsed after stepping the potential down from 1,200 to 1,056 mV vs. SCE, and placing the drop of acid on the ribbon at position 0 mm. The numbers denote the maxima in the corresponding current–time curve (see Fig. 2.11) <http://link.aps.org/abstract/PRE/v54/p3744>. The outside equipotential lines correspond to a potential of 300 mV cathodic with respect to the applied potential of 1,056 mV vs. SCE. Subsequent lines are 50 mV apart. Reprinted with permission from [26] <http://link.aps.org/abstract/PRE/v54/p3744>. Copyright 1996 by the American Physical Society

It is important to note that in these experiments the leading edge of active zones moved with the velocity increasing in time, so the observed phenomena were one more example of the accelerating fronts.

It is also interesting that if the electrode potential is slightly more positive than the Flade potential, the system exhibits excitable characteristics—not with respect to homogeneous, but *spatially inhomogeneous* fluctuations. According to the basic characteristics of spatiotemporal excitability (cf. Sect. 1.1.2), the too small local fluctuation, which physically means formation of local active area, is damped, while a disturbance exceeding certain threshold expands along the entire electrode. The current, initially enhanced due to local activation, now increases significantly more and when the active area reaches the end(s) of the electrode, this current drops to its original value. In this case, the experimental realization involved Co wire of diameter 1 mm, placed against the Co ribbon, brought into the passive state by sufficiently anodic polarization. Since the Co wire has no protective film, an

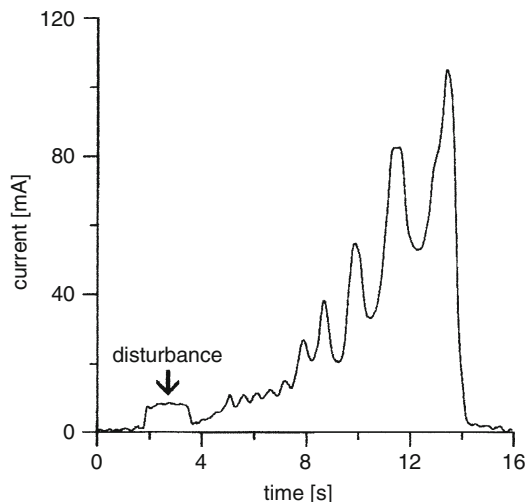
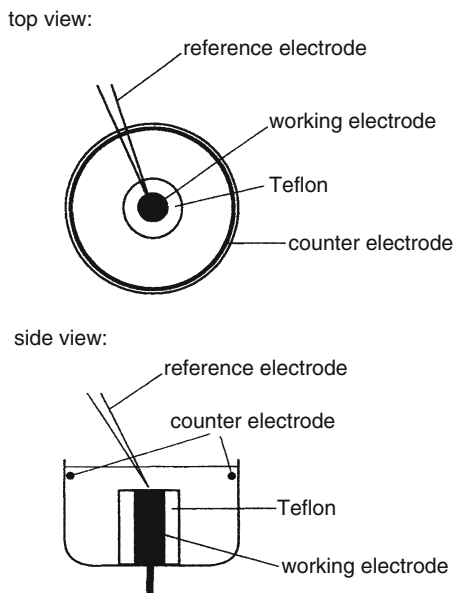


**Fig. 2.11** Current–time curve with modulation following initiation of activation in the passive region: 1.25 M phosphate buffer, pH 1.67, applied potential 1,150 mV/SCE. Passivation for 15 s. Disturbance at the end of the ribbon. Reprinted with permission from [26] <http://link.aps.org/abstract/PRE/v54/p3744>. Copyright 1996 by the American Physical Society

oxidation reaction occurs on it immediately after its potential is brought to that of the ribbon. Oxidation on the wire occurs with a simultaneous local reduction of the passive film on the ribbon Co electrode. The single active region, produced in this way, travels along the ribbon, reaches its end(s), and the system returns to the original passive state. Figure 2.11 shows the corresponding temporal variations of the current observed after activation of Co ribbon at one of its ends.

This  $I$ – $t$  shape can be explained in the following way. The Co ribbon was first passivated for 15 s and then disturbed with the cobalt wire, for ca. 2.5 s, at position close to its end. The initially low current increased then for the time when the disturbance was maintained and after that slightly decreased. As the perturbation was sufficiently large, the active zone produced began to expand as it traveled, since the activation was faster than the passivation; accordingly the current increased significantly. During this travel, the active zone grew and shrank (it “breathed”) and therefore the current exhibited oscillatory variation. Eventually the active zones reached the end of the Co ribbon and the current permanently fell to a very low value, corresponding to the original passive state of the electrode. It is interesting to consider this alternate increase and decrease of the width of the active region when the electrode potential is close to the Flade potential. This phenomenon means that the trailing edge of the active region propagates intermittently in the reverse direction, and that the velocity of this reverse motion is significantly higher than the primary forward velocity of the leading edge. This modulation leads to an additional (intermittent) acceleration of the leading edge and explains an increase in the total current.

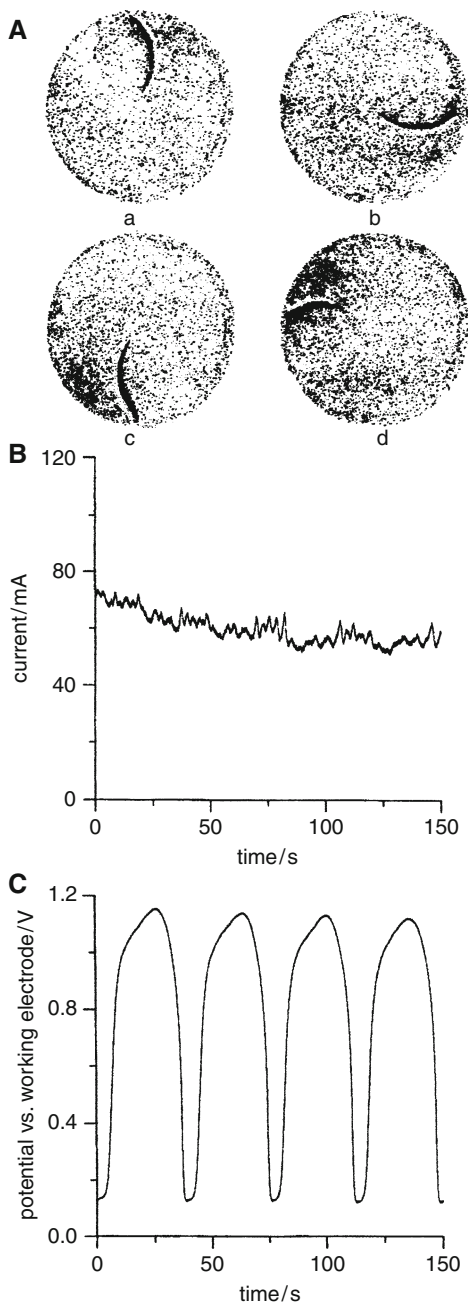
**Fig. 2.12** Experimental setup for studies of spatiotemporal patterns on Co electrode. Reproduced from [27] by permission of the Royal Society of Chemistry



When the shape of the cobalt electrode was changed to the disk or the ring geometry [27], the rotating waves were recorded during the anodic oxidation of such electrodes in buffered phosphate solutions media. The experiments were performed under potentiostatic conditions. The three-electrode arrangement, with Co disk of a 12.5 mm diameter, is shown in Fig. 2.12; the ring electrode was obtained by sealing the center part of the disk with adhesive tape leaving an outer ring with a width of 1.25 mm. The reference electrode approached the working electrode with a Haber-Luggin capillary, placed ca. 1 mm away from the surface in the center of Co disk. The copper wire encircling the Co disk at the same height was used as a counter electrode.

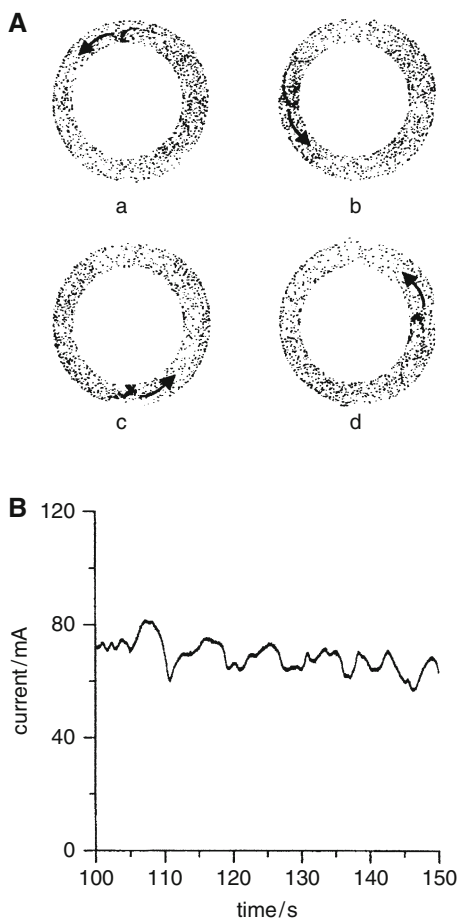
Depending on particular experimental conditions, such system can exhibit either bistability, or oscillations, or modulated electrochemical waves. Here we shall briefly describe the formation of spatiotemporal patterns. The experiment starts from stepping the electrode potential from the rest value to a value between 500 and 1,000 mV (i.e., below the Flade potential). Under such conditions, the inhomogeneous distribution of the electrode potential already manifests itself: the center of the Co electrode (close to the tip of the RE) is in active state, while its rest, peripheral area, attains a passive state. Next the potential is stepped to an appropriate, more anodic value, at which most of the Co electrode becomes passivated, while the anodic current significantly decreases. However, further evolution of the electrode surface state is by no means trivial. A small circular active area, starting from the center of the disk, begins to develop, with the diameter growing and moving towards the rim of the electrode; accordingly, anodic current increases. It is possible to observe the border between the passive and active zone visually. At certain moment of the ring development it becomes asymmetric and breaks up into

**Fig. 2.13** (A) Video images of a clockwise rotating wave at 850 mV vs. SCE (first rotation); (a–d): sequence of snapshots for every quarter of the rotation. (B) Current–time curve of the rotating wave at 850 mV vs. SCE. (C) Potential between the working electrode and an additional calomel reference electrode with a capillary placed at the rim of the working electrode *ca.* 1 mm away from the surface. Reproduced from [27] by permission of the Royal Society of Chemistry



two branches. Of these two branches, one remains stationary and the other one moves in a clockwise or counterclockwise manner around the tip of the reference electrode, with the period of 30–50 s. Figure 2.13 shows the exemplary video

**Fig. 2.14** (A) Digitized video images of a single counterclockwise rotation wave on the electrode at 700 mV vs. SCE; period of rotation: 9 s; (a–d): sequence of snapshots for every quarter of rotation; the arrow denotes position and direction of propagation of the wave. (B) Current–time curve of the single wave on the ring electrode. Reproduced from [27] by permission of The Royal Society of Chemistry



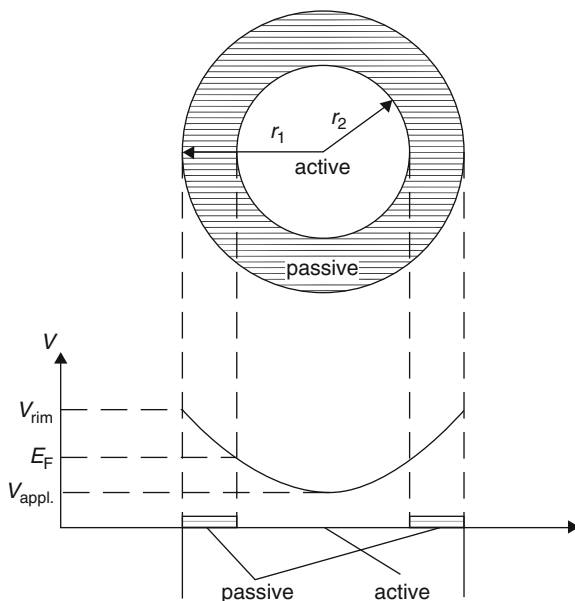
images of the clockwise rotating wave, compared with the temporal dependence of the current and of the potential of the working electrode, measured with an additional reference electrode. The variations of this potential indicate the transitions between the passive and the active state during the passage of the front.

When, in another experiment, the potential was established at more anodic value (+950 mV), the modulated system's behavior is observed, with the activation front moving in the reverse direction. Finally, if the Co disk is modified into the ring electrode, the rotating waves were reported (Fig. 2.14). Also in this case a modulation of the oscillatory characteristics, visualized on the  $I$ – $t$  dependences, can be observed.

In the preliminary explanation of these phenomena, one should consider the spatial distribution of the potential drop along the electrode radius, caused by the geometrical arrangement of the working and the reference electrodes (Fig. 2.15).

If in certain region of the electrode, the potential is lower than the Flade potential, this part of the electrode remains an active state, otherwise it attains the

**Fig. 2.15** Qualitative dependence of the potential drop on the radial position and hypothetical coverage with a passive layer,  $V_{\text{rim}}$ —potential at the rim of the working electrode;  $E_F$ —Flade potential;  $V_{\text{appl}}$ —applied potential. Reproduced from [27] by permission of The Royal Society of Chemistry



passive state. In an ideal circular geometry, the boundary between the active and passive regions is circular and for such steady state the current should be constant, determined largely by the active part of the surface (which in turn depends on the external voltage applied). The dynamic situation which develops for the case of rotating waves, shown in Fig. 2.14, corresponds to a quasi-steady state: the active area remains constant as the pulse rotates around the disk. At the border between the active and the passive regions there occurs a significant difference in the local current density and hence in the ohmic potential drop in the electrolyte. Figure 2.15 shows local potential gradients associated with the propagation of rotating waves. Locally, when the electrode potential is shifted to the value more negative than the Flade potential, electrodisolution of passive layer occurs and the advance of the wave is compensated by repassivation in the back of the wave. Evidently, the gradient of electrode potential causes the coupling between different sites of the electrodes and causes the side migration of ions which is involved in the propagation of waves.

## 2.4 Spatial Patterns in the $\text{Ni}/\text{H}_2\text{SO}_4$ Oscillator

In Sect. 6.1.4 of volume I, the temporal instabilities and bifurcation analysis of the  $\text{Ni}/\text{H}_2\text{SO}_4$  oscillator, classified as typical HN-NDR system, were described. Here, as the introduction to the coupled  $\text{Ni}/\text{H}_2\text{SO}_4$  oscillators in Sect. 3.1.6, we describe the formation of spatiotemporal patterns during the transpassive nickel dissolution in sulfuric acid medium, reported in the pioneer work by Lev et al. [28].

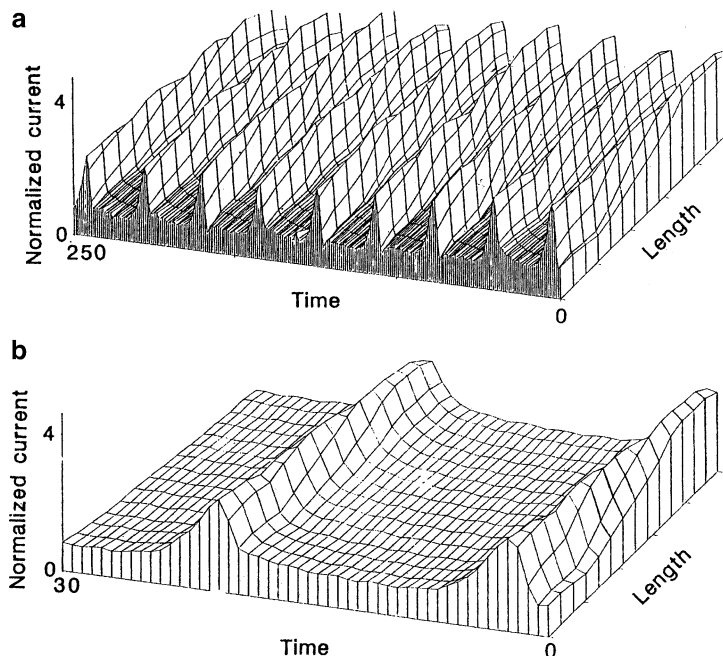


**Fig. 2.16** Traveling waves during almost potentiostatic oscillations: (a) Three-dimensional representation of local current distribution. (b) Enlarged section. Operating conditions: 20-cm nickel wire in 6 N sulfuric acid, 1.67 V relative to saturated calomel electrode. Current normalized relative to  $65 \text{ mA cm}^{-2}$ , distributed homogeneously. Timescale in scans ( $50 \text{ scans s}^{-1}$ ); length scale covers the whole wire. Reproduced by permission from Macmillan Publishers Ltd. [28], Copyright 1988

The electrochemical cell of dimensions  $200 \times 200 \times 40 \text{ mm}$ , constructed of plexiglass, held two parallel nickel wires, 0.63 mm in diameter and 200 mm in length, situated 12 mm apart. A calomel reference electrode was situated 40 mm behind the counter electrode at the center of the cell. Like in experiments by Osterwald described in Sect. 6.1.4 of volume I, the operational mode of the electrochemical experiment could have been switched quickly between the potentiostatic and galvanostatic regimes. It is important to note how the operational mode affected the morphology of induced spatiotemporal patterns.

The spatial distribution of local currents was recorded by 15 Ag–AgCl micro-reference electrodes equally spaced along the working electrode, relative to a common calomel electrode situated near the reference electrode [28]. Figure 2.16 shows typical trains of waves (sequence of pulses) that set in, under *almost potentiostatic* conditions, after destabilization of a homogeneous current distribution through the external, serial  $1 \Omega$  resistor. This is the presence of that small resistance, and in consequence of ohmic potentials drops, which does not allow to call the experiment to be truly potentiostatic. The pulses started at the right-hand side of the electrode and traveled at nearly constant velocity of ca.  $4.5 \text{ m s}^{-1}$  to the

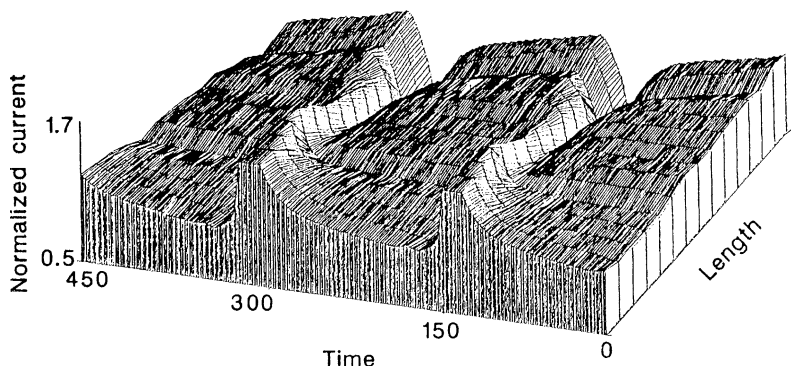


**Fig. 2.17** Local current distribution of antiphase oscillations during galvanostatic operation. Operating conditions: 20-cm nickel wire in 2 N sulfuric acid, current is  $16.25 \text{ mA cm}^{-2}$ ; local current normalized relative to the current density at  $15.5 \text{ mA cm}^{-2}$  as measured under potentiostatic conditions ( $I = (v_g - v_0)/(v_p - v_0)$ ), where  $v_0$ ,  $v_g$ , and  $v_p$  are the micro-electrode potential at rest, under galvanostatic and under potentiostatic conditions, respectively. Time and length scales are the same as in Fig. 2.16. Reproduced by permission from Macmillan Publishers Ltd. [28], Copyright 1988

other end of the electrode. This shows good global synchronization among the local oscillators.

Particularly interesting are the antiphase oscillations, shown in Fig. 2.17 which require an analysis in view of more recent understanding of various kinds of spatial couplings operating in electrochemical systems. One should note here that these antiphase oscillations occurred under galvanostatic conditions, where positive global coupling should counteract the pattern formation. This means that in the oscillatory region the effect of positive global coupling is not as straightforward as it could be inferred from the simple theory [19]. More detailed experimental and theoretical studies of these phenomena, the latter ones in terms of appropriately extended Haim et al. model (cf. Sect. 6.1.4, volume I), are reported in [29] and [30], respectively.

## 2.5 Modeling the Spatiotemporal Patterns in Electrodeposition Processes

### 2.5.1 The Two-Dimensional Model for Bistable and Oscillatory Process

The progress in understanding of the mechanism of formation of spatiotemporal patterns led to the elaboration of models which allowed to simulate such patterns during metal electrodeposition, for various electrochemical cell geometry, electrolyte conductivity, and double layer capacitance. For example, Bîrzu et al. [31] have

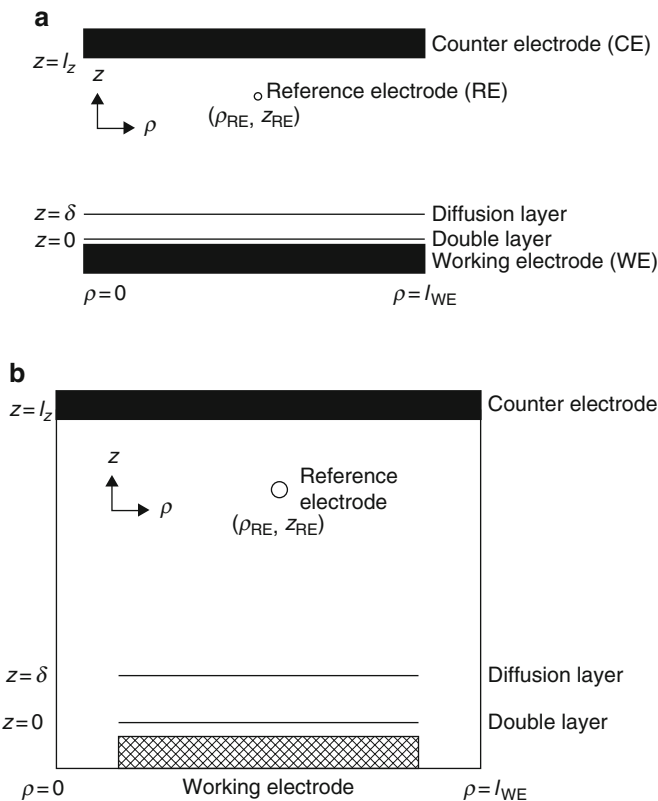


**Fig. 2.18** Schematics of the two geometries with working and counter electrodes and a point-like reference electrode: **(a)** Ring geometry,  $l_{WE}$  is the circumference of the ring; **(b)** Ribbon electrode embedded in insulator,  $l_{WE}$  is the length of the ribbon plus insulating side regions. Reproduced from [31] by permission of the PCCP Owner Societies

developed a numerical model for the bistable and oscillatory process occurring during metal electrodissolution, for assumed two-dimensional geometry, involving ring or ribbon working electrode and a point-like reference electrode located in the electrolyte between the working and the counter electrodes (Fig. 2.18).

Concerning the electrochemical mechanism, this model invokes the principles of the Frank-FitzHugh approach (Sect. 6.1.2.2, volume I) in which the dependence of the Flade potential on pH varying near the electrode surface was one of the important factors deciding the active/passive system's dynamics. The interfacial potential drop (electrode potential) and the concentration of  $H^+$  ions at the electrode surface were assumed as two dynamical variables. The oscillations were then caused by the interplay between diffusion and migration of protons with the pH dependence of the Flade potential. In terms of the Nernst concept of the diffusion layer of thickness  $\delta$ , the respective equations are:

$$\frac{\partial [\text{H}^+]}{\partial t} = \frac{2D_{\text{H}^+}([\text{H}^+]_{\text{bulk}} - [\text{H}^+]_{\text{WE}})}{\delta^2} + \frac{2\mu[\text{H}^+]_{\text{WE}}}{\delta} \left( \frac{\partial \phi}{\partial z} \Big|_{z=0} \right) \quad (2.5)$$

$$C_d \frac{\partial \phi}{\partial t} = \kappa \left( \frac{\partial \phi}{\partial z} \Big|_{z=0} \right) + \frac{A}{\exp[-\alpha(-\phi_{\text{dl}} + V_{\text{f}}([\text{H}^+]_{\text{WE}}))] + 1} \quad (2.6)$$

where  $D_{\text{H}^+}$  is the diffusion coefficient of  $\text{H}^+$  ions,  $\mu$  is their migration coefficient,  $C_d$ —differential double layer capacitance,  $\kappa$ —solution conductivity,  $\phi_{\text{dl}}$ —interfacial potential drop at the working electrode,  $V_{\text{f}}([\text{H}^+])$ —the pH-dependent Flade potential, while  $A$  and  $\alpha$  are the appropriate constants defining the magnitude of the maximum faradaic reaction current and the slope of the active–passive transition, respectively. These equations served as two of boundary conditions which were used in solving the Laplace equation ( $\nabla^2 \phi = 0$ ) for the entire system. The significance of the calculations lies mainly on the indication how important is the localization of the reference electrode on the patterns emerging in the model system, both for the bistable and oscillatory regions of the electrode process. In particular, for the oscillatory regime the direction of the passivation wave could even be reversed by changing the location of the reference electrode to the position relatively apart from the working electrode surface. In this case, the passivation wave starts at the center of the working electrode and moves towards the edges, while the activation waves start at the edges and move toward the center. If the reference electrode is moved closer to the WE, the activation and passivation waves both start at the outer edges and move towards the center.

## 2.5.2 The Extension to Three-Dimensional Model

### 2.5.2.1 Cell Geometries and Basic Bifurcation Scenarios

A logical development of the two-dimensional approach was the extension of the above model to the three-dimensional geometry, keeping the assumption of the point-like reference electrode (Fig. 2.19) [32].

This modification allowed to model the rotating waves on a ring electrode, antiphase oscillations, spatially homogeneous oscillations, nonuniform stationary state, and the transitions between these regimes. Furthermore, in [33], the accelerating fronts, rotating waves, and homogeneous oscillations were modeled, in relation to experimental studies of electrodisolution of cobalt and iron, in buffered phosphoric acid and sulfuric acid/ $\text{Na}_2\text{SO}_4$  solutions, respectively, under potentiostatic conditions.

Further development of these model studies involved simulation of patterns in the three-dimensional space, for the *excitable* characteristics of the electrochemical system [34]. These numerical simulations not only showed again how important is the role of the cell geometry (electrodes arrangement) in the type of patterns that

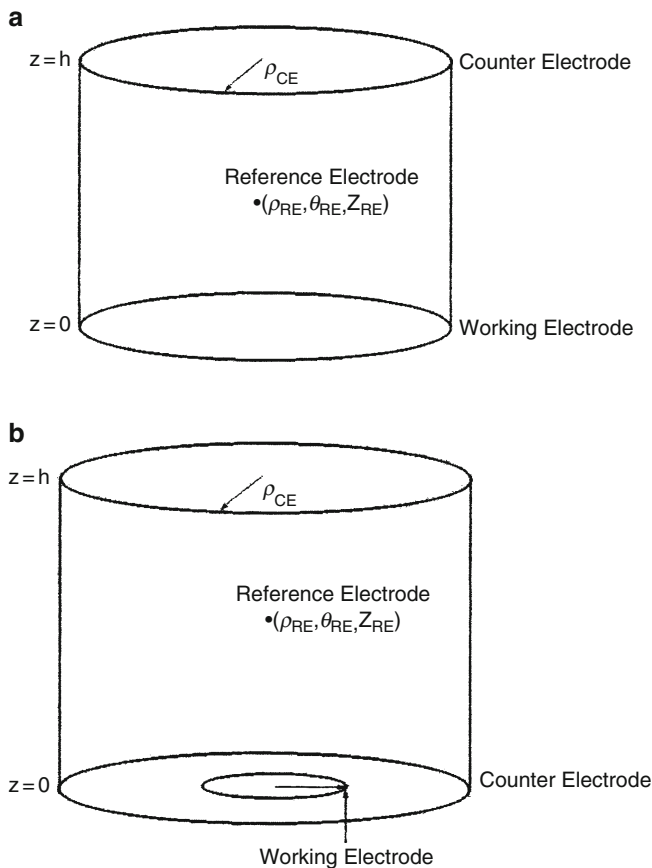


**Fig. 2.19** Scheme of electrode arrangement. (a) Three-dimensional geometry. The counter electrode in the same radius as the working electrode,  $\rho_{WE}$  at a distance  $h$  from each other. (b) Three-dimensional geometry. The working electrode, with a radius  $\rho_{WE}$  and the counter electrode of radius  $\rho_{CE}$  are in the same plane. Reprinted from [32], Copyright 2001, with permission from Elsevier

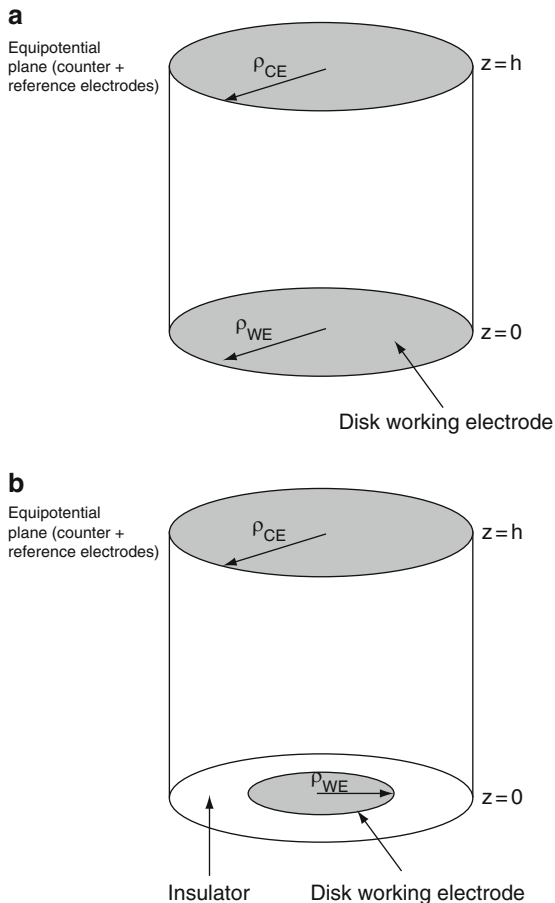
can emerge under given conditions. Not less important are the conclusions indicating that the response of the excitable electrochemical system for the appropriate perturbation can be *remarkably different* from those reported for nonelectrochemical reaction diffusion system. As described in Sect. 1.2.2, the main reason for that is the difference in the range of coupling that exists in such systems: in chemical ones it is only diffusion, i.e., a short-range (or local) coupling, engaging the closest neighborhood of the given site, while in electrochemical systems, the coupling is dominated by migration which, as involving the electric field, is a long-range, or nonlocal type of coupling. The simulations were performed for two cell geometries as shown in Fig. 2.20.

**Fig. 2.20** Cell geometries used in the simulations.

(a) Geometry 1: the disk WE occupies the entire lower plane of the cylindrical cell.

(b) Geometry 2: the WE is embedded in an insulator.

The CE is modeled as an equipotential plane, the RE is assumed to be located in the plane of CE [34]. Reproduced by permission of the PCCP Owner Societies



As in earlier studies, the working electrode symbolizes the metal phase that exhibit active (high anodic current)/passive (low anodic current) transitions under potentiostatic conditions. In the case of geometry (a), every part of the working electrode has the same electric potential, but for geometry (b) it is of course not the case. Since the effective resistance at the rim of the disk is smaller than in the center (see Sect. 1.2), the electrode potential is higher at the rim of the disk than in the center.

Transition from the active to passive state is marked with the region of the N-shaped negative differential resistance (N-NDR). Similarly as in the classical Frank-FitzHugh model, the main carrier of the current in the solution are  $H^+$  ions, so the local pH at the electrode surface is different, depending on whether the electrode is in active or passive state. The destabilization of the system towards the bistability or oscillatory behavior occurs due to the interaction of the NDR characteristics with these changes of local solution pH, meaning the dependence of the Flade potential on pH (being as high as  $117 \text{ mV pH}^{-1}$ ). The calculation details

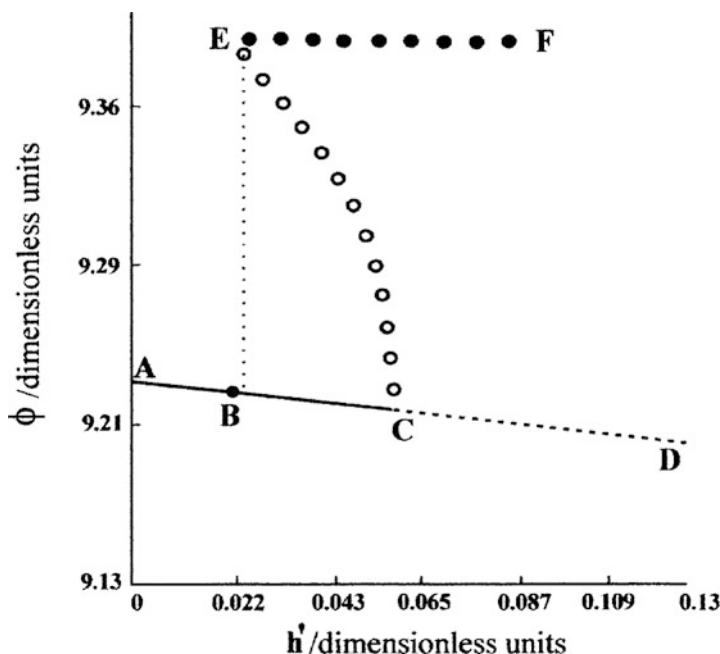


**Fig. 2.21** Bifurcation diagram of the uniform system (a) as a function of the scaled cell height. Existence regions of the different limit sets: AC—stable (excitable) stationary state; CD—unstable stationary state; CE—unstable limit cycle; EF—stable limit cycle; EC—coexisting range of the stable stationary state and the stable limit cycle. The solid and hollow dots give the maximum of the amplitude of the stable and unstable limit cycles, respectively. C—location of a subcritical Hopf bifurcation. See [34] for underlying equations and parameter values [34]. Reproduced by permission of the PCCP Owner Societies

the interested reader will find in original reference [34], while below we briefly summarize the most representative results of calculations.

Obviously *uniform* steady states exist only for geometry (a) and not for geometry (b) of the cell. Figure 2.21 shows the bifurcation diagram of the uniform system, constructed in terms of scaled height of the cell:  $h' = (h - h_0)/h_0$ , with  $h_0 = 0.023$  cm.

Furthermore, for the uniform system, Fig. 2.22 shows the representative, different phase portraits, that were constructed from the nullclines of the electrode potential and proton concentration dynamics, for two different heights of the cell  $h$ , after transformation of the variables to the dimensionless ones. The portrait on Fig. 2.22a, corresponding to  $h$  smaller than that for Fig. 2.22b, shows the dynamics typical of excitable behavior—after a small (but exceeding certain threshold) perturbation the system makes a large excursion in the phase space, before it returns to the steady state being a stable focus, thus in the form of damped oscillations. In turn, Fig. 2.22b is a phase portrait for the cell height ca.

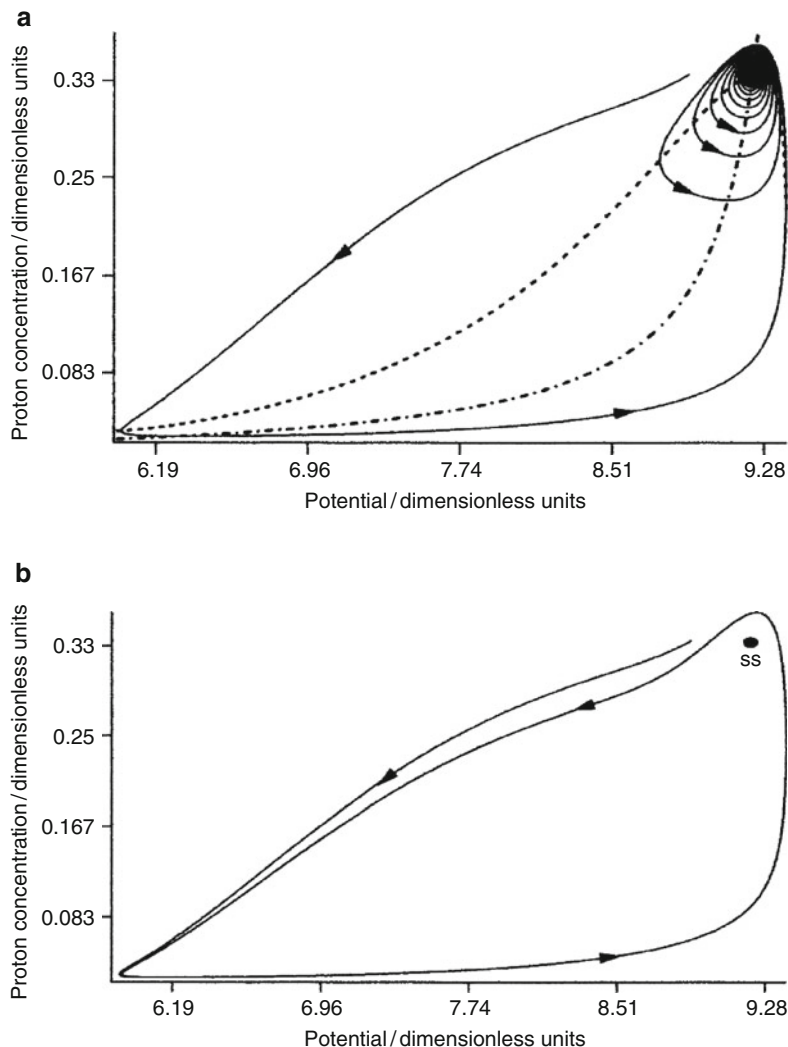


**Fig. 2.22** (a) Phase portrait of the excitable uniform system.  $h' = 0.022$ . The *dashed* and *dashed-dotted* lines represent the nullclines for the electrode potential and the proton concentration, respectively. Their intersection is the excitable stationary state: after a small perturbation from the stationary state, the system makes a large excursion before returning in an oscillatory manner to the steady state (*continuous* line). (b) Phase portrait for a similar perturbation from the stationary state as in (a) but for  $h' = 0.043$ . At this value of  $h'$  the stable stationary state (denoted SS) coexists with a stable limit cycle. See [34] for the parameter values [34]. Reproduced by permission of the PCCP Owner Societies

twice as high as for Fig. 2.22a. In this case, the system is no longer excitable, but the perturbed steady state loses its stability in the subcritical Hopf bifurcation and the resulting asymptotic regime is the continuous trip along the limit cycle.

Applying this bifurcation scenario to the inhomogeneous potential distribution means that upon increasing cell height ( $h$ ) the subcritical Hopf bifurcation will occur at different values of  $h$  for different radial positions—first in the center of the disk and only for sufficiently high values of  $h$  it will reach the rim of the disk. Numerical simulations involving the spatial coordinate have shown that the two cell geometries considered yield substantially different spatiotemporal patterns.

### 2.5.2.2 Patterns in an Inhomogeneous Case

The principal scheme of evolution of spatiotemporal pattern in this case, when the system is excitable, is the pulse generation, the propagation scheme of which depends on the ratio of radii of the working and the counter electrodes:  $\rho_{WE}/\rho_{CE}$ . If this ratio is relatively small, the single perturbation of the initially passive (and excitable) state of the entire electrode causes the appearance and expansion of active region, which moves from the excitation point to the opposite side of the disk, where it vanishes and the whole electrode surface returns to the initial steady state (Fig. 2.23a). Simultaneously, the temporal variation of the anodic current indicates a large-amplitude peak followed by small oscillations with a vanishing amplitude, as the asymptotic steady state is a stable focus (Fig. 2.23b).

When the radius of the working electrode is appropriately increased, with the  $\rho_{WE}/\rho_{CE}$  ratio kept constant, the system dynamics changes to the coexistence of a stationary nonuniform steady state and a limit cycle. However, in this case, if a single perturbation of the initial passive steady state is not large enough to cause a transition to the limit cycle, it can trigger quite a complex dynamics: a propagation of multiple pulses with pulse reflection (Fig. 2.24). Note, for example, pictures 9–13 which show how, at certain stage of the system's evolution, the traveling pulse reaches the right edge of the disk electrode, then splits and send back a new pulse that travels to the opposite edge where it disappears.

Other modes of perturbations were also studied, leading to different responses of the model system. When the system of the same characteristics as in Fig. 2.24 was perturbed at two locations, symmetric with respect to the center of the disk, a pair of pulses developed and further evolution indicated the onset of periodic oscillations, which constituted the front-like transitions between fairly uniform active and passive states (Fig. 2.25), with total current periodically oscillating as a function of time.

Furthermore, if instead of a single perturbing pulse, an intense, continuous perturbation was applied at one location (again for the same other parameters, as in Fig. 2.24), the onset of asymmetric periodic oscillations was observed. The detailed description of this and other modes of evolution of the system's state in an inhomogeneous case, the reader will find in the original reference [34].

### 2.5.2.3 Patterns in a Homogeneous Case

Considering the system geometry from Fig. 2.20a, i.e., for the homogeneous case, one should emphasize the substantially different response for the single local perturbation (Fig. 2.26).

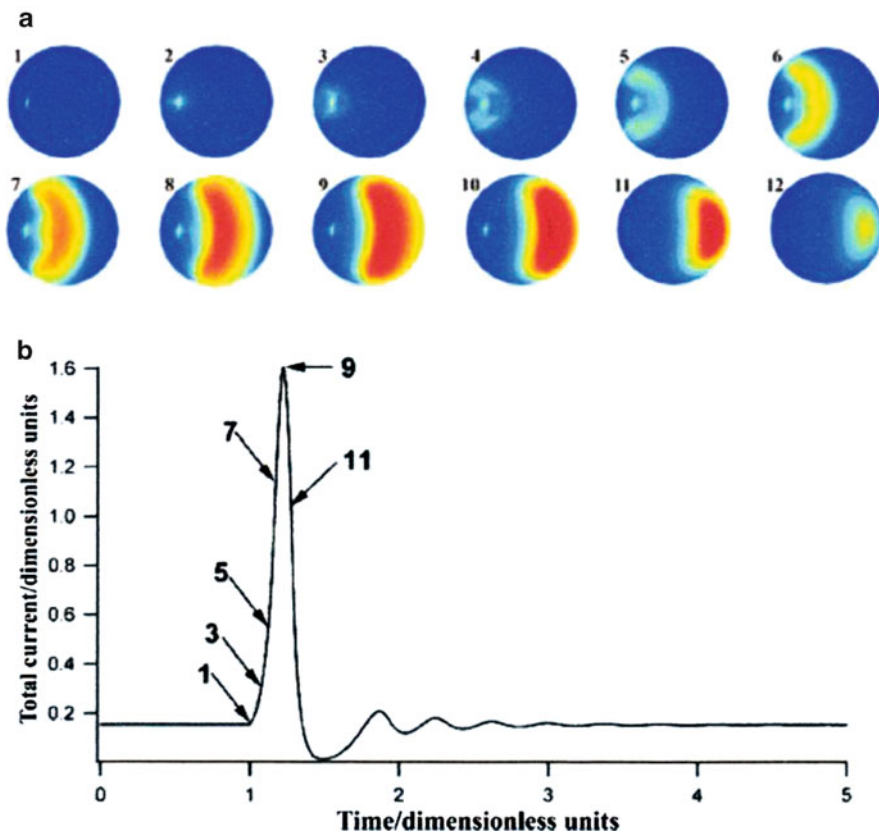


**Fig. 2.23** (a) Pulse propagation for *geometry 2* and the excitable state between A and B in Fig. 2.21. The excitable stationary state was perturbed by imposing a potential value of 7.74 on a grid element centered at  $(0.67 \rho_{WE}, \theta = 0^\circ)$ , during 0.25 time units. The images show the potential on the disk WE at different times; *blue* represents high potential (passive) and *red* low potential (active). (b) Total current. The perturbation starts at approximately 1 time unit. The arrows point to the moments of time corresponding to the frames from (a). Parameter values:  $\sigma'$  (proportional to  $\sigma/hA$ ) = 0.262;  $\gamma'$  (proportional to  $\mu\delta/Dh$ ,  $\mu$ —mobility of  $H^+$  ions,  $\delta$ —thickness of the diffusion layer in front of WE,  $D$ —diffusion coefficient of  $H^+$ ) = 10.51;  $h' = 0.0696$ ;  $\rho_{WE}/\rho_{CE} = 0.8$ ;  $h/\rho_{CE} = 0.309$ ; other parameters as in Fig. 2.21 [34]. Reproduced by permission of the PCCP Owner Societies

The active region that appears in this place spreads faster towards the edge of the electrode than towards the center (Frame 2) and, what seems to be most surprising, once the more activated region has touched the edge of the electrode, the activation spreads fast along the entire rim of the disk (Frame 3), the activation of the remaining electrode occurring then from the rim towards the center. This activation is followed by passivation that starts at the electrode rim and spreads over the entire electrode. Subsequently, the system relaxes back to the excitable steady state. It is particularly important to note that this behavior of the model electrochemical system is essentially different from that expected for the nonelectrochemical,

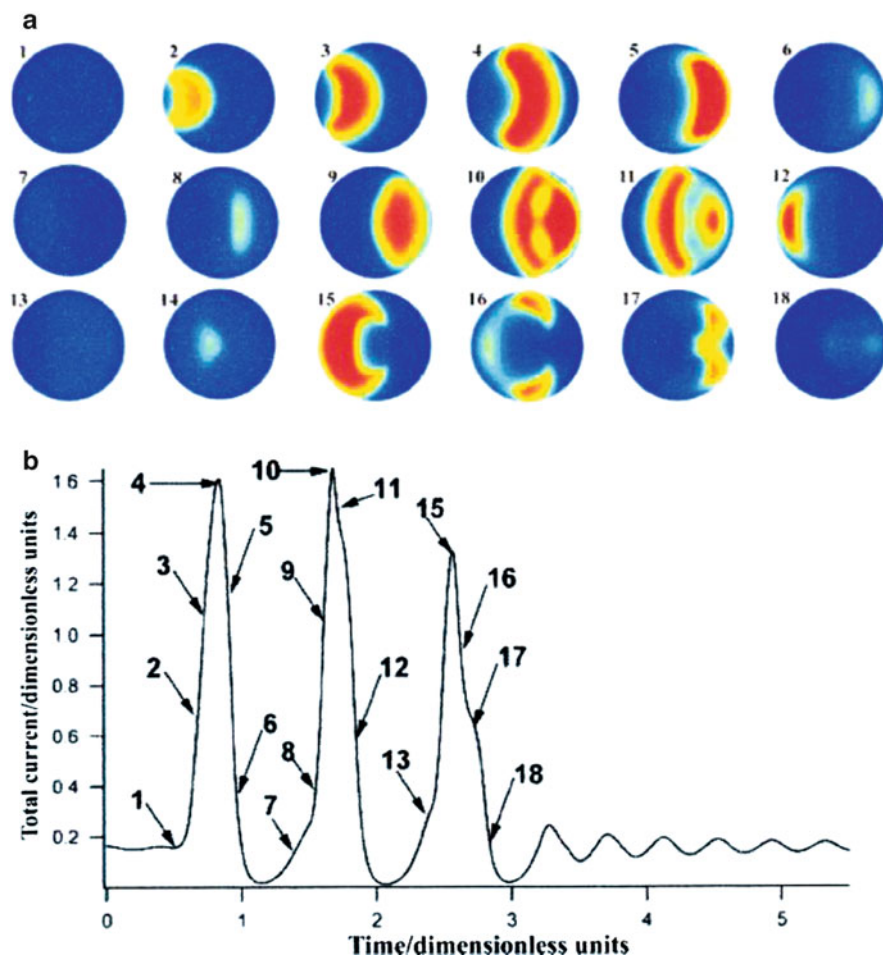


**Fig. 2.24** (a) Multiple pulse propagation with pulse reflection. With respect to Fig. 2.23, the radius of the cell was increased,  $h/\rho_{CE} = 0.1545$ , the other parameters are the same as in Fig. 2.23. The images show the potential on the disk at different times. (b) Total current corresponding to (a). The perturbation starts at approximately 0.5 time units [34]. Reproduced by permission of the PCCP Owner Societies

reaction-diffusion system (RDS), for which a single, circular, propagating pulse would form, locally extinguished upon reaching the system's boundary. This difference illustrates the specific role of the migration (nonlocal) coupling in the generation of the specific system's dynamics, compared to the diffusion (local) coupling.

Furthermore, if larger working electrode is considered, it appears that above critical value of its radius, the system does not relax back to the uniform steady state, but complex spatiotemporal motion prevails, like that shown in Fig. 2.27.

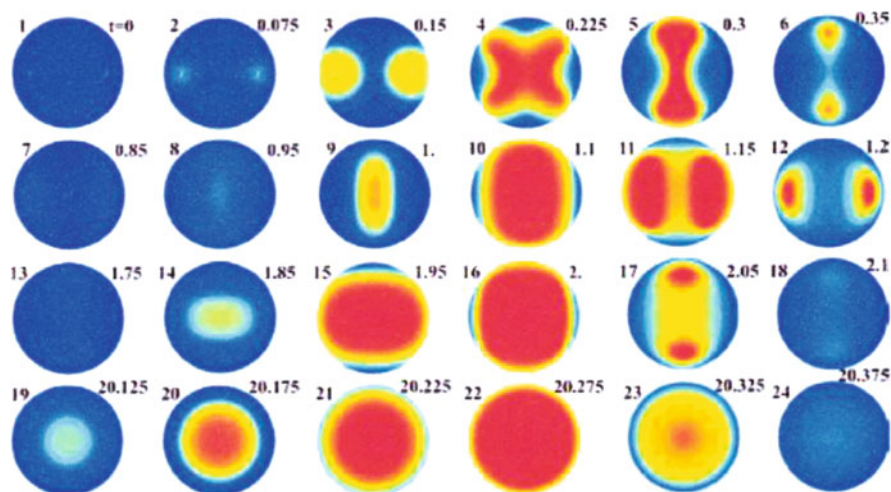


**Fig. 2.25** Onset of periodic oscillations. The images show the potential on the disk WE at different times, marked in the upper right side of each frame. Same conditions as in Fig. 2.24, but a second perturbation that is symmetrical with respect to the center is applied [34]. Reproduced by permission of the PCCP Owner Societies

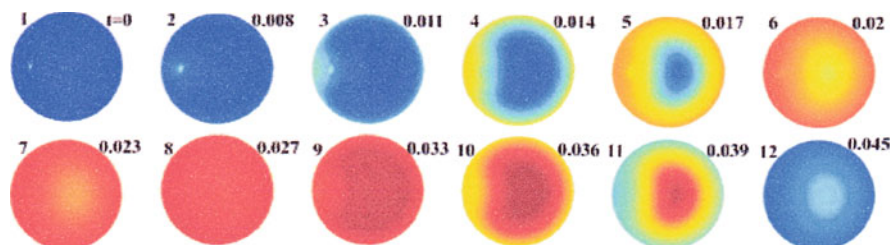


**Fig. 2.26** Pulse propagation for *geometry 1* and asymmetric perturbation of the excitable stationary state. The images show the potential on the disk WE at different times, marked in the upper right side of each frame. Parameter values:  $\sigma' = 0.275$ ;  $\gamma' = 11$ ,  $h' = 0.022$ ,  $h/\rho_{WE} = 0.369$ . Other parameters as in Fig. 2.21. The perturbation was imposed on a grid element centered at  $(0.675 \rho_{WE}, \theta = 0^\circ)$  where  $\phi_{dl}$  was set to 7.738, between 0.25 and 0.35 time units [34]. Reproduced by permission of the PCCP Owner Societies

This is a striking manifestation of the dependence of spatiotemporal dynamics emerging from the excitable steady state on the boundary conditions. Further studies involved, among others, the effect of circular perturbation which resulted in the self-sustained target pattern-like structures, with preserved angular symmetry.

Concluding, the above results show, in terms of appropriate model calculations, the significant role of the cell geometry (in this case—of the way the working electrode is embedded in the electrochemical cell) in the spatiotemporal dynamics of the evolution of the state of the electrode surface in the active/passive region. If the working electrode is surrounded by the insulator, i.e., when the WE radius is

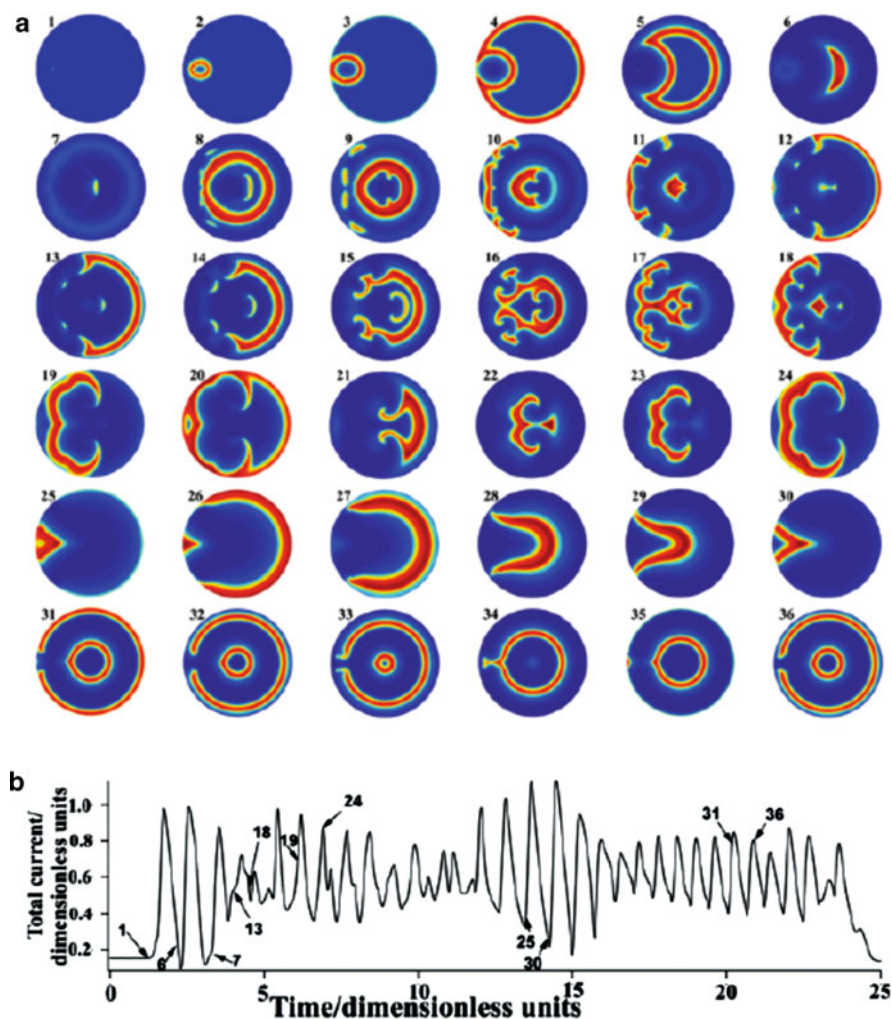


**Fig. 2.27** (a) Pulse propagation for geometry 1 and asymmetric perturbation of the excitable stable stationary state (the corresponding electrode potential and proton concentration at the stationary state are  $\phi^0 = 9.224$ ;  $[\text{H}_{\text{WE}}^{+}]^0 = 0.338$ ). The images show the potential on the disk WE at different times. Parameter values:  $\sigma' = 0.275$ ;  $\gamma' = 11$ ,  $h' = 0.022$ ,  $h/\rho_{\text{WE}} = 0.0369$ . Other parameters as in Fig. 2.21. The perturbation was imposed on a grid element centered at  $(0.686 \rho_{\text{WE}}, \theta = 0^\circ)$ , where  $\phi_{\text{dl}}$  was set to 7.738, between 1.25 and 1.375 time units. (b) Total current corresponding to (a) [34]. Reproduced by permission of the PCCP Owner Societies

smaller than that of the counter electrode, the rim of the electrode is kept in more passive state than the center. This situation, in cooperation with such specific dynamical characteristics, like the coexistence of the limit cycle with the stationary state and the proximity of the subcritical Hopf bifurcation gives rise to complex spatiotemporal dynamics, dependent also on the magnitude and duration of the

perturbation imposed. For the apparently simpler electrode configuration, in which the radii of the WE and CE are equal, the response of the excitable state appears to be fundamentally different from that expected for the chemical, RDS. In the latter ones, the characteristic parameters of spiral waves or target patterns are determined by the kinetic parameters of the process, rather than by the boundary conditions, as long as the domain size is much larger than the characteristic pattern size. In the case of an electrochemical system considered earlier, we have seen the surprising strong dependence of the spatiotemporal behavior on the boundary conditions. This is because the properties of migration coupling depend strongly on the boundary conditions in the plane of the working electrode [34].

### 2.5.3 Modeling the Electrochemical Turbulence

The same geometries of the electrochemical cell, as shown in Fig. 2.20, were more recently used by Bîrzu and Krischer [35] in the modeling of a two-dimensional electrochemical turbulence (i.e., *spatiotemporal chaotic dynamics*) during the oscillatory electrodisolution of metal disk electrodes. Note the reversed terminology: the terms “Geometry I” and “Geometry II,” used in the captions to figures below, will refer now to the “inhomogeneous case” and “homogeneous case,” respectively.

We shall briefly describe here the main results. The assumed electrode process exhibited not sinusoidal, but relaxation oscillations which means that the system’s parameters were far away from the point of the supercritical Hopf bifurcation. As the bifurcation parameter there was chosen the system’s size, defined as the ratio between the cell radius and cell height:  $w = (\rho_{WE}/h)$ , meaning the “aspect ratio” of the cell. Finally, only the migration (nonlocal) coupling was assumed to exist in the system. The spatiotemporal patterns were developed in two dimensions parallel to the working electrode surface. The set of two dynamical variables consisted of the interfacial potential drop at the working electrode (an activatory variable)  $\phi_{di}$  and the concentration of  $H^+$  ions at this electrode in the solution,  $[H^+]$  (an inhibitory variable).

#### 2.5.3.1 Turbulence in an Inhomogeneous Case

The series of numerical simulations was performed for increasingly larger working electrodes, i.e., for increasing values of bifurcation parameter  $w$ . For sufficiently small electrode ( $w = 0.764$ ) the quasi-periodic course of oscillations of total current vs. time was obtained, and no corresponding irregular patterns, but only a simple spatial pattern was generated (Fig. 2.28).

With increasing cell aspect ratio, the spatially coherent patterns became unstable and irregular spatiotemporal states developed, with the typical transient regime depicted in Fig. 2.29.

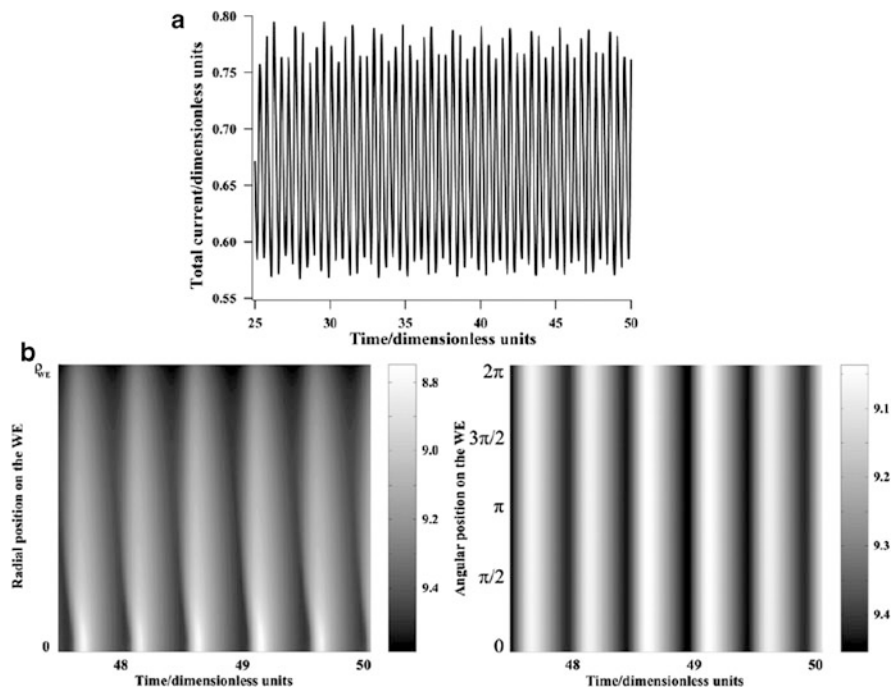


**Fig. 2.28**  $\rho_{WE}/h = 0.764$ . Geometry I: spatially coherent dynamics. (a) Asymptotic time series of the total current. (b) Asymptotic radial (*left*) and angular (*right*) temporal evolution of  $\phi_{dI}$ . The angular evolution is shown at  $\rho = 0.5\rho_{WE}$ . (*white* denotes active states and *black* passive ones) [35]. Reproduced by permission of the PCCP Owner Societies

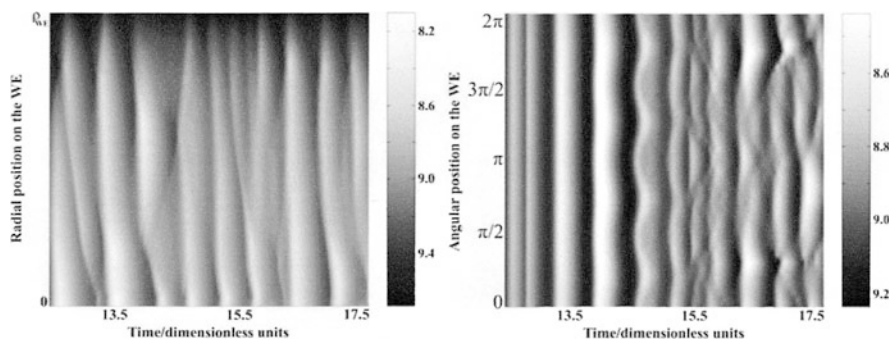


**Fig. 2.29**  $\rho_{WE}/h = 3.182$ . Geometry I: spatiotemporal evolution of the radial and angular dependence of  $\phi_{dI}$  around the angular symmetry breaking. The angular evolution is shown at  $\rho = 0.5\rho_{WE}$  [35]. Reproduced by permission of the PCCP Owner Societies

Figure 2.30 shows the snapshots of amplitude and phase for four different, increasing aspect ratios of the cell. These images, which show the symmetric transition states and the fully turbulent (chaotic) regimes, confirm that the system's dynamics becomes more chaotic as the system size increases [35].

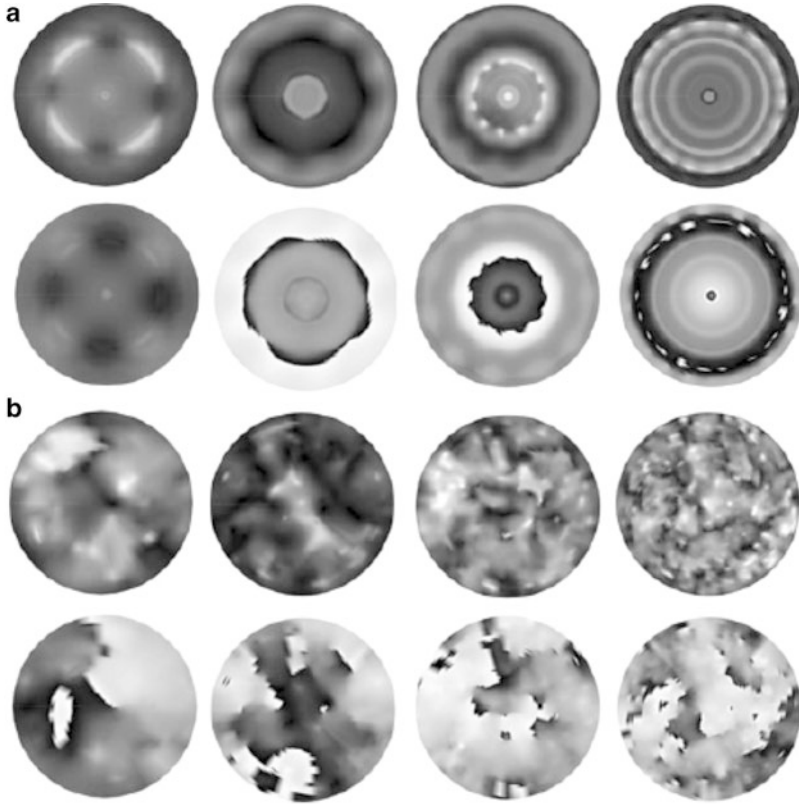


**Fig. 2.30** Geometry I: Snapshots of amplitude (*upper row*) and phase (*lower row*) for four different electrode sizes (**a**) during the symmetric transients and (**b**) in the defect turbulent regime.  $\rho_{WE}/h = 3.182$  (*first column*), 4.773 (*second column*), 6.366 (*third column*) and 9.549 (*last column*) [35]. Reproduced by permission of the PCCP Owner Societies

The term “defect turbulent regime” in the caption of Fig. 2.31 refers to the idea that the spatial disorder is generated by the so-called defects (meaning the singularities in the field of the oscillation phase).

### 2.5.3.2 Turbulence in a Homogeneous Case

Model calculations show that even for the homogeneous case (“Geometry II”), although the local oscillatory dynamics does not vary with position, the long-term dynamics may also exhibit irregularity in time and space [35] (see Fig. 2.31) which is presumably caused by the strong spatial coupling along the angular direction close to the rim of the electrode.

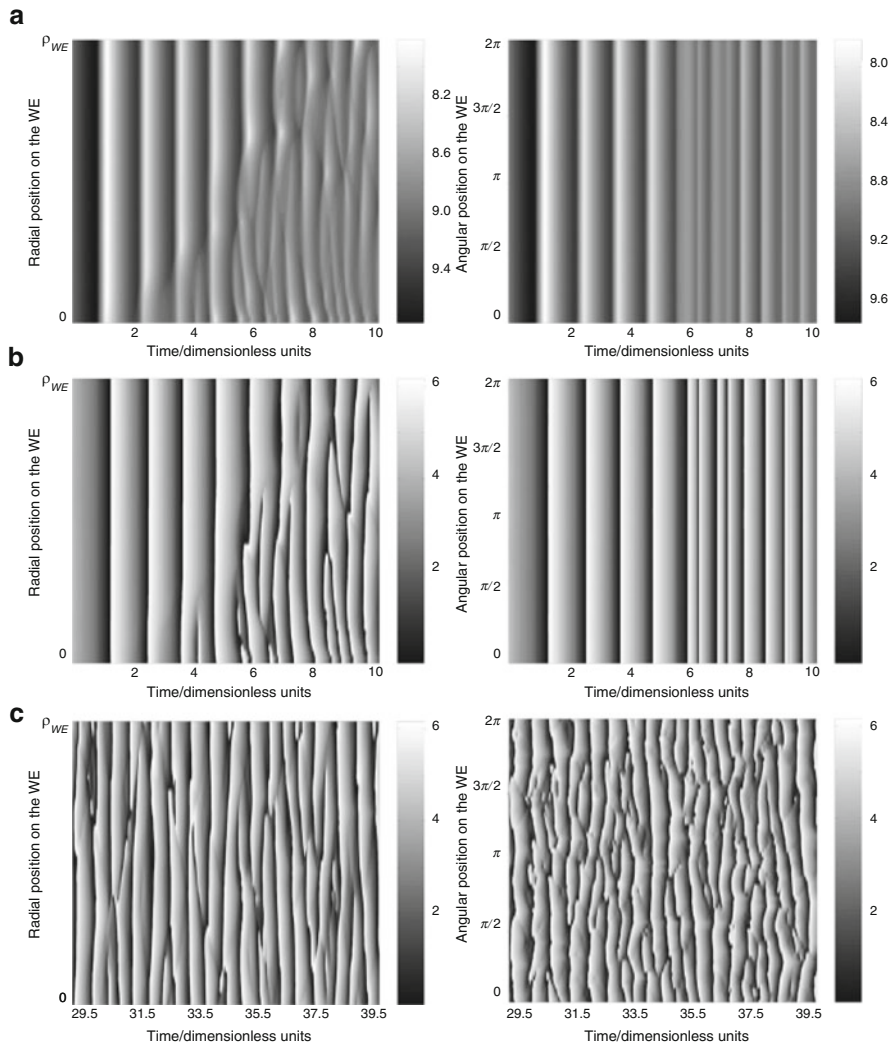


**Fig. 2.31**  $\rho_{WE}/h = 6.366$ , Geometry II: (a) radial (*left*) and angular (*right*) cut of  $\phi_{dI}$  for the first ten time units. (b) Radial and angular cut of the oscillation phases for the first ten time units. (c) Same as (b) but for the asymptotic dynamics [35]. Reproduced by permission of the PCCP Owner Societies

The reader interested in more detailed interpretation of these phenomena and their quantitative analysis in terms of such tools of analysis of spatiotemporal data, as the Karhunen–Loève decomposition [36], is advised to consult the original paper [35].

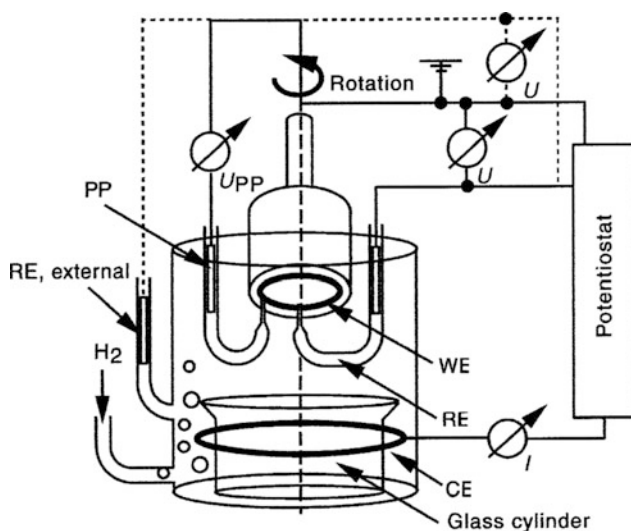


**Fig. 2.32** Scheme of the electrochemical cell. WE: working electrode, RE: reference electrode (note that either the RE in the Haber-Luggin capillary with the tip on the axis of the ring or the external RE was used). CE: counter electrode, PP: potential probe [37]. Reproduced by permission of the PCCP Owner Societies

## 2.6 Patterns in $H_2$ Oxidation

In complement to temporal instabilities in electrochemical oxidation of  $H_2$  at Pt electrodes (section 5.1, Vol. I), in this section we shall discuss the formation of spatiotemporal patterns in this process, as described by Krischer, Varela et al. in a series of papers [37–41]. In most experiments the specially designed setup was used, which included the ring Pt electrode as the working electrode, at which electrooxidation of  $H_2$  occurred, while the series of microprobes located along this ring allowed to measure the actual spatial distribution of the electric potential (Fig. 2.32).

Essential results of these studies, which confirm theoretical predictions about the conditions of formation of spatiotemporal patterns, can be summarized in the following way.

For the bistable region of the  $H_2$  electrooxidation, when the distance between the WE and RE was relatively large or medium, the transitions between the two homogeneous states occurred through nucleation and growth of the globally stable state from the initially metastable one.

For the bistable region, but for the closest WE–RE distance, when the negative global coupling manifested itself strongly, stationary (nonequilibrium) patterns were observed, consisting of two domains, i.e., with high currents (where Pt surface was bare) and low currents (where Pt–O domains existed on surface), respectively, with the difference in the double layer potentials of two domains reaching more than 1 V! [37].

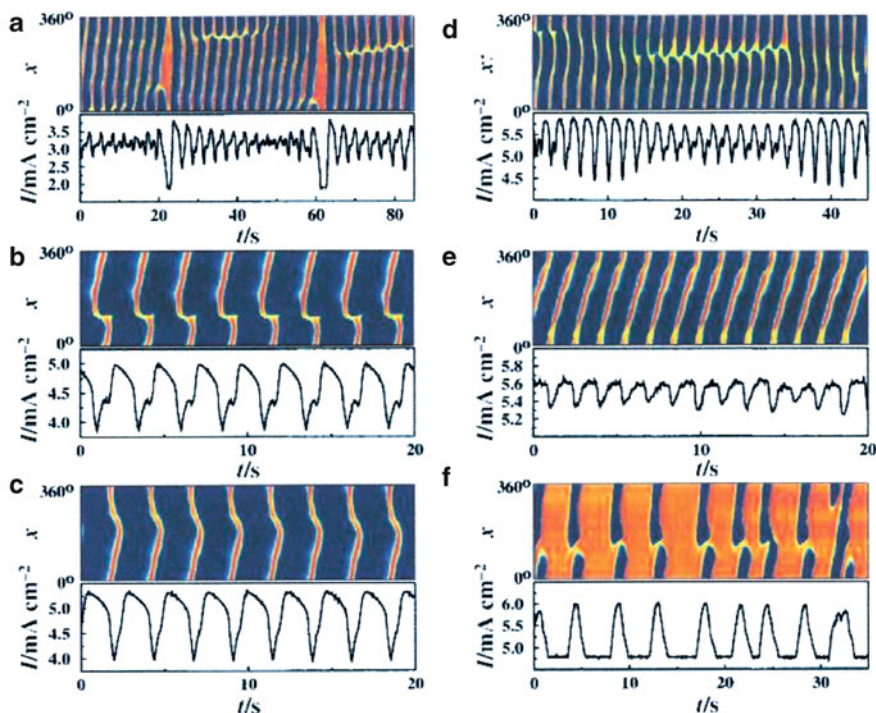


**Fig. 2.33** Position–time plots of the local double layer potential and corresponding time series of the global current under potentiostatic conditions with the reference electrode [RE(2)] placed at a distance of 13 mm from the plane of the WE for different values of the external voltage  $U$ : (a) 1.06, (b) 1.37, (c) 1.5, (d) 1.67, (e) 1.76 and (f) 1.86 V vs. SHE. Reproduced from [38] by permission of The Royal Society of Chemistry

In the presence of poisoning, electro-sorbing ions (i.e., after addition of 0.1 mM HCl and 0.025 M CuSO<sub>4</sub> to the 0.5 mM H<sub>2</sub>SO<sub>4</sub> solution saturated with H<sub>2</sub>), and under potentiostatic conditions, the system's dynamics was studied again for the three positions of the RE with respect to WE, corresponding to zero, intermediate, and maximum global coupling. In the first case, when only migration (nonlocal) coupling could operate, spatially inhomogeneous oscillations were reported and attributed to a spatial bifurcation of the homogeneous limit cycle; the systems appeared to be Benjamin–Feir unstable [42, 43]. In the other extreme case, corresponding to strongest global coupling, the spatiotemporal dynamics was qualitatively different—the quasi-harmonic oscillations of the total current (with the shape dependent on the external potential) were accompanied with the pulse propagating around the ring in a fairly uniform manner. This was the change of the width of the pulse during one rotation around the ring which caused these current oscillations. Finally, at intermediate distance between the RE and WE, a particularly rich dynamics were observed, depending on the external voltage (see Fig. 2.33) [38].

In Fig. 2.33 the following dynamic behaviors are shown: (a) low-voltage, complex spatiotemporal patterns, made up of a sequence of behaviors, that appear

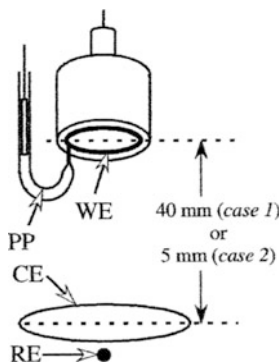


**Fig. 2.34** Experimental setup for studies of chaotic patterns in  $\text{H}_2$  electrooxidation: WE, working electrode (mean circumference: 85 mm; width: 1 mm), CE: counter electrode, RE: reference electrode ( $\text{Hg}/\text{Hg}_2\text{SO}_4$ , sat.), located below the plane of the CE, PP: potential probe. The WE was rotated at 20 Hz and the spatiotemporal evolution of the interfacial potential was obtained by the PP with a resolution of 50 points per rotation. See [41] <http://link.aps.org/abstract/PRL/v94/p174104>. Copyright 2005 by The American Physical Society

“isolated” at larger values of  $U$ ; (b) periodical generation of two pulses, of which only one propagates effectively in one direction, while the other one, which is about to travel into the opposite direction, stops soon and their meeting leads to mutual annihilation; this behavior was considered the formation of a novel pattern type—the “asymmetric target pattern”; (c) similarly to (b), periodical generation, at the position  $0^\circ=360^\circ$ , of two pulses which however now travel in opposite directions and meet in the center of the ring where they annihilate each other (a kind of one-dimensional analog of the “target pattern”); (d) the combination of cases (b) and (c)—the system switches back and forth between the target and the asymmetric target pattern; (e) a pulse traveling around the electrode with slightly changing velocity; (f) a front-like, non-periodic excitation travels once around the ring before it is extinguished again at a certain position [38]. These experimental observations of asymmetric target patterns were supported by perfectly concordant results of numerical simulations in terms of appropriate model [40]. These calculations clearly revealed that the nonlocal migration coupling was crucial for the endogenous persistence of the perturbation that caused the asymmetry.

Furthermore, for the  $\text{H}_2$  oxidation, also in the presence of  $\text{Cu}^{2+}$  and  $\text{Cl}^-$  poisons, Varela et al. [39] have reported the complex hierarchy of patterns, involving, among others, nested spatial (and temporal) symmetry breakings of the emerging domains, the scenario being presumably a universal route leading to a substructuring of space in systems which experience a global coupling and possess at least two adjacent regions in the parameter space that exhibit dynamical instabilities.

Chaos, i.e., “electrochemical turbulence” was also reported in the  $\text{H}_2$  electrooxidation. In these experiments, the distance between WE and the CE was varied, with the tip of RE located always *just below* the CE and such configuration minimized the global coupling, leaving only migration (nonlocal) coupling as the operating one (Fig. 2.34). Experiments were conducted for two different distances

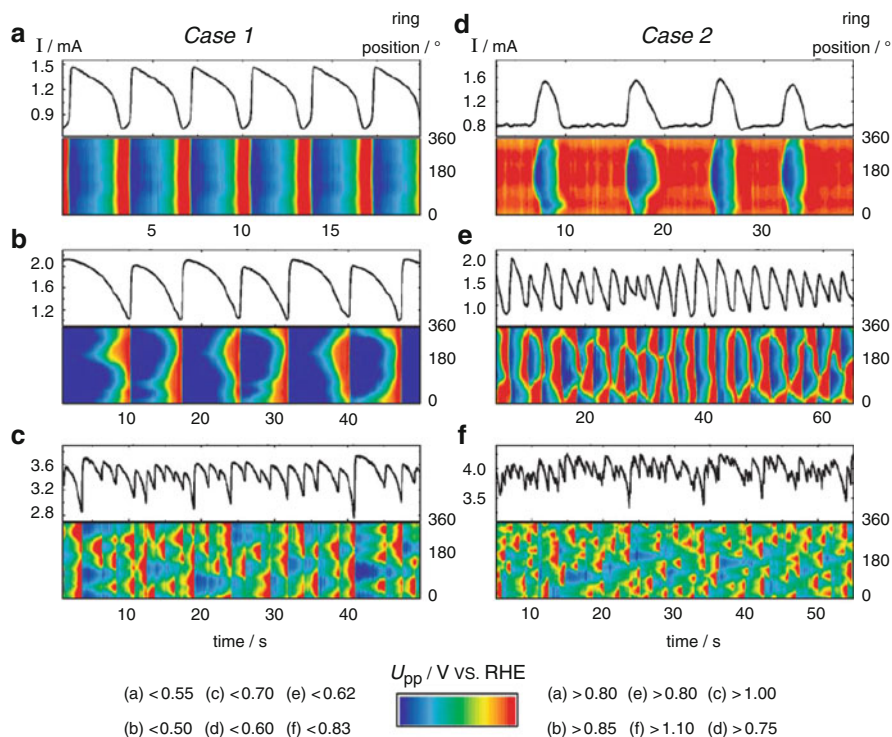


**Fig. 2.35** Global current time series and spatiotemporal evolution of the interfacial potential,  $\phi_{dl}$ , as a function of position on the ring and time for different values of the applied voltage  $U$  and electrode placement corresponding to case 1 [plates (a), (b), and (c)] and case 2 [(d), (e), and (f)].  $U$ : (a) 1.06 V, (b) 1.19 V, (c) 2.14 V, (d) 0.82 V, (e) 0.89 V, and (f) 1.54 V. Electrolyte: H<sub>2</sub>-saturated, aqueous 0.5 mM H<sub>2</sub>SO<sub>4</sub> solution containing 0.1 mM HCl and 0.01 mM CuSO<sub>4</sub>. A continuous flow of H<sub>2</sub> was maintained throughout the experiments. Reprinted with permission from [41] <http://link.aps.org/abstract/PRL/v94/p174104>. Copyright 2005 by The American Physical Society

between the WE and CE: 40 mm (case 1) and 5 mm (case 2) to realize different coupling ranges.

For this experimental arrangement, Fig. 2.35 shows the global current–time series and spatiotemporal evolution of the interfacial potential (denoted by  $\phi_{dl}$ , as usual as an alternative for  $E$ ) for two WE–CE distances (case 1 and case 2) and different voltages. In particular, Figs. 2.35c, f show irregular oscillations of total current and associated irregularities in pattern formation.

In the analysis of these phenomena, it was advantageous to transform the potential values into amplitude and phase variables. Then, for strongly irregular data there were found the locations, at which the amplitude vanished and the phase changed abruptly. It was possible to determine the density of such space–time defects which was increasing with voltage, starting from zero and indicating a transition into a defect turbulent regime. In turn, the irregular phase

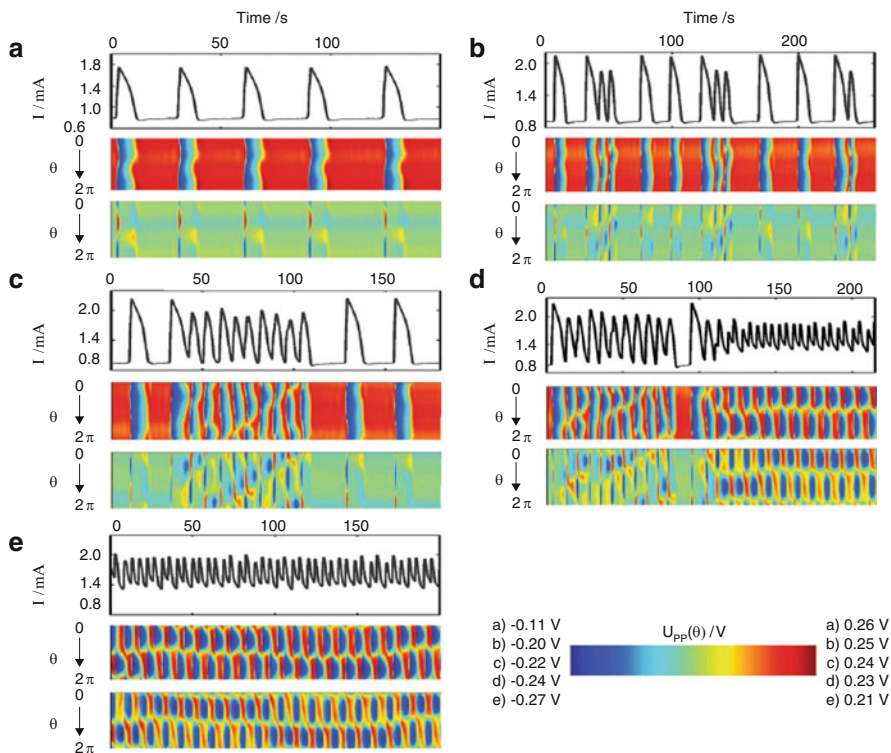


**Fig. 2.36** For global coupling strength  $|\rho| \approx 0.3$ : Time series of the global current (*upper plates*), spatiotemporal evolution of the interfacial potential drop (*middle plates*), and spatiotemporal evolution of the inhomogeneous part of the interfacial potential drop (*lower plates*) for weak global coupling about five different values of the applied voltage  $U$ : (a) 1.02 V, (b) 1.11 V, (c) 1.14 V, (d) 1.17 V, (e) 1.18 V. Cell resistance  $R_\Omega = 510 \pm 20 \Omega$ , compensated resistance  $R_c = 160 \pm 20 \Omega$ . Electrolyte composition: 0.5 mM  $\text{H}_2\text{SO}_4$ , 0.1 mM  $\text{HCl}$ , and 0.01 mM  $\text{CuSO}_4$ ,  $\text{H}_2$ —saturated. Rotation rate of the electrode  $\omega = 20$  Hz. The transformation of the measured interfacial potential drops ( $U_{pp}$ ) into the color code is given at the bottom. The values to the left and right of the color bar denote the minimum and maximum  $U_{pp}$  values, respectively [39]. Reproduced by permission of the PCCP Owner Societies

modulation dominated, in the absence of defects, at lower voltages. So, irregular series shown in Fig. 2.36 are the experimental manifestation of a transition from the phase to defect turbulence. For the sake of generalization, it is important to note that quite analogous sequence of events was previously found in theoretical treatment of spatiotemporal chaos, done in the framework of the complex Ginzburg–Landau (CGLE) equation for diffusively coupled oscillators close to a supercritical Hopf bifurcation. In terms of this analysis, the one-dimensional system enters the region of spatiotemporal chaos via the above-mentioned Benjamin–Feir (BF) instability which first leads to phase turbulence followed by defect turbulence (phase dislocations) upon farther driving system away from the BF point [44]. The present analysis proves that similar scenario occurs also for

the system with nonlocal (nondiffusive) coupling which is, in addition, far from a supercritical Hopf bifurcation.

Furthermore, the H<sub>2</sub> electrooxidation in the presence of poisons was studied under conditions favoring the existence of a global coupling [39] which was this time introduced either by placing the RE between the WE and CE, on the axis of WE (cf. Fig. 2.21) or by compensating part of the cell resistance with an external negative impedance device (NID). Experimental conditions were chosen so that the migration coupling induced the spatiotemporal chaos (see above). Two parameters were varied systematically—the strength of global coupling and the externally applied voltage. Without global coupling, increasing  $U$  led to a transition from a spatially modulated limit cycle, via a phase turbulent regime, to space–time defect turbulence, while the presence of even weak global coupling suppressed the occurrence of defect turbulence, with the formation of regular two-phase clusters (domains). The strength of global coupling substantially affected the transition scenarios and the final dynamical states reached at high values of  $U$ . At appropriately high strength of global coupling, a second type of two-phase cluster was observed, as well as two types of irregular cluster patterns, with the irregularly moving boundaries, and accompanied with the emergence and disappearance of clusters through splitting and merging the boundaries, respectively. At even higher coupling strengths, the five-phase clusters were stabilized and finally, when the coupling was the highest, the cluster patterns transformed into strongly modulated pulses. Of a rich set of dynamical modes, shown in [39] we shall choose here, as an example, the simplest case of weak global coupling [expressed quantitatively as the value of parameter  $|\rho| = 0.3$  (which varies from 0 to 1)] illustrated by Fig. 2.36. Initially, at low value of  $U$ , nearly periodic relaxation oscillations of the global current, synchronized with the interfacial potential of the entire electrode, are observed, as in the case described in the previous section. However, further system evolution following the increase in  $U$  is now completely different due to the presence of a negative global coupling. Instead of formation of space–time defects, a transition to a two-phase cluster took place: two domains formed on the electrode, which oscillated with identical frequency but 180° out of phase. Locations within each of the two domains oscillated with approximately identical amplitude and phase. Of other type of clusters found under global coupling conditions, two were found as novel ones.

In conclusion, it is evident that H<sub>2</sub> electrooxidation on Pt, particularly in the presence of Cl<sup>−</sup> and Cu<sup>2+</sup> ions, is a source of variety of spatiotemporal regimes. The reader interested in analysis of rich sets of experimental data as well their theoretical treatment is advised to consult the respective original references.

At the end of this section, we shall mention that the spatiotemporal patterns emerging during H<sub>2</sub> electrooxidation have been used by Krischer et al. to compare two essential methods of inducing the global coupling: either by close position of RE to WE or by insertion of an external resistor in series to the WE, in the potentiostatic experiment. A certain difference between these two ways of creating such coupling consists in that in the latter case it is easy to adjust the coupling strength by varying the external resistance, for the given cell resistance, but in the

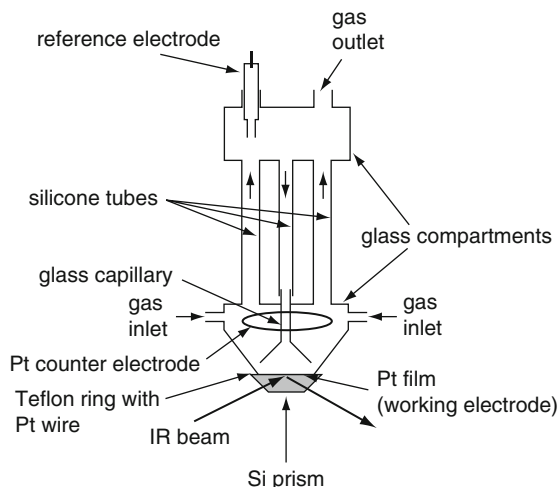
former case this strength is a more complicated function of RE position, cell geometry, and electrolyte conductivity (see, e.g., the approach presented in [52]). In a more recent paper, Krischer et al. [45] have presented an alternative approach to this problem, in terms of general equivalent circuit of an electrochemical cell and by introducing the subcircuit of the negative impedance device (NID). Theoretical considerations, verified experimentally by the studies of  $\text{H}_2$  oxidation on Pt ring electrode, in the presence of  $\text{Cu}^{2+}$  and  $\text{Cl}^-$  poisons, proved that the same strength of global feedback can be caused by two equivalent methods of compensation of the cell resistance: either by placing the tip of the reference electrode close to the WE (using Haber-Luggin capillary) or by inserting the serial negative ohmic resistance, of the absolute value equal to the cell resistance. This finding is important, since the use of external negative resistor exerts the same coupling effect independently of the relative arrangement and geometry of the electrodes, which dependence was the main problem in case of using the Haber-Luggin capillary (see Section 1.2.2). In fact, in both cases, the cyclic voltammograms, the (low-amplitude) current oscillations, and spatiotemporal evolution of the electrode potential during  $\text{H}_2$  electrooxidation were found almost identical. In other words, the global feedback realized through the external, electronic ohmic drop compensation is always strictly global, i.e., all locations of the electrode are coupled with the same strength. Such application of NID was further used by Plenge et al. [46], this time for the  $\text{IO}_4^-$  electroreduction on the 50 nm thick, rectangular Ag(111) electrode evaporated onto a glass plate. This process, in neutral supporting electrolyte ( $\text{NaClO}_4$ ), is characterized with the N-NDR region. The spatial patterns were monitored with surface plasmon spectroscopy. Upon inserting the appropriate negative impedance, the surface plasmon images indicated correlation between the current oscillations and nonuniform changes of the optical properties of the interface. A striking result was that the two halves of the electrode oscillated alternately in a harmonic manner, the resulting pattern resembling the standing wave born in a wave bifurcation.

Finally, a recent theoretical study by Baba and Krischer [47] of the model of oscillatory electrooxidation of hydrogen in the presence of poisons under galvanostatic conditions led to generation of mixed-mode (MMO) oscillations for low preset currents, in the homogeneous case. For spatially extended systems, there were formed cluster patterns exhibiting interesting features resulting from a combination of the properties of the homogeneous oscillations in the model and spatial coupling (see original reference for details)

## 2.7 Patterns in CO Oxidation

In Sect. 3.9 of volume I, the effect of spatiotemporal dynamics on the impedance spectra was described, taking as a model system the bulk electrooxidation of CO on a rotating Pt electrode which process is characterized with an S-NDR region in the

**Fig. 2.37** Electrochemical cell used for IR measurements. A chemically deposited Pt film was used as the working electrode. The radiation totally reflected at the metal/liquid interface is analyzed. The geometrical area of Pt film in contact with the electrolyte is approximately 175 mm<sup>2</sup>. Reprinted with permission from [50]. Copyright 2008 American Chemical Society



current–potential curve [48]. Such characteristic was found to occur due to the interaction between the competitive Langmuir–Hinshelwood mechanism and the mass transport of CO towards the electrode. It was also found experimentally that direct measurements of the S-shaped polarization curve, under controlled conditions, could not explicitly indicate the NDR region which could be suggested only by current–potential curve at fast galvanodynamic scans [49] (cf. Sect. 5.2, volume I). For the purposes of this section, it is important to note that one reason for this was found the formation of spatial patterns on the electrodes. The emergence of such patterns was recently proved by Morsch et al. [50] by means of spatially resolved infrared spectroscopy used for the detection of electrode areas covered and free of CO. IR measurements were performed during galvanostatic oxidation of CO on Pt film electrode in a setup shown in Fig. 2.37.

Representative results of the experiments are shown in Fig. 2.38. It is shown that the way in which Pt electrode is covered with CO depends on imposed current. For applied current up to 1.3 mA, Pt surface is completely covered with CO (symbolized red color). When the current is increased up to 1.8 mA, the studied area splits into regions still covered with CO (red zone) and (almost) free of CO (blue zone). The area of CO-free region increases with applied current. Finally, for currents higher than 1.8 mA, the low coverage state spreads over the entire probed region. Detailed quantitative analysis reveals also, on some pictures, broad transition regions between the CO-covered and CO-free zones.

Careful reader of Sect. 1.2 will realize that electrooxidation of CO on Pt, as the process exhibiting S-NDR characteristics, could be a candidate for the formation of spatial structures which exactly meet the criteria of electrochemical Turing patterns. In fact, such patterns were obtained for this system, they are described further in Sect. 2.10.

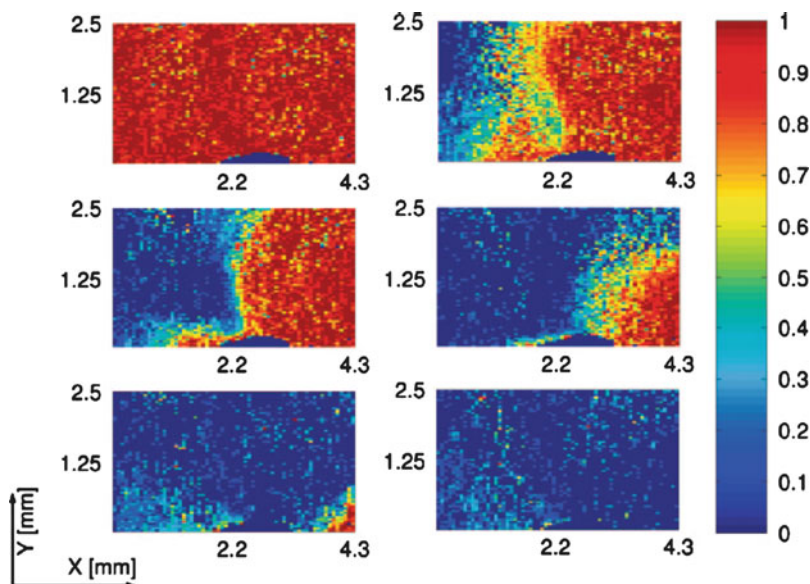


**Fig. 2.38** Integrated CO peak plotted versus space for the following currents: 0.30, 1.40, 1.50, 1.70, 1.75, and 1.80 mA (left to right and top to bottom). Red indicates a high coverage, and blue a CO free surface. Note that the blue region in the middle of the lower edge indicates an area where the film hardly showed any CO peak even for complete coverage. Therefore, this region was set to 0 in all images. Reprinted with permission from [50]. Copyright 2008 American Chemical Society

## 2.8 Patterns in HCOOH Oxidation

The oscillatory oxidation of formic acid on Pt electrodes, being a HN-NDR type oscillator was described in detail in Chap. 5 of volume I. Under appropriate conditions, this process can also give rise to spatial and spatiotemporal patterns. In 1999, Christoph et al. [51] have reported an interesting phenomenon, observed during the potentiostatic oxidation of formic acid on a Pt ring (see Fig. 2.39), under conditions when the electrode process exhibited bistability, i.e., the coexistence of the passive (OH-poisoned, low-current) and active (high-current) states. An appropriate perturbation at one location of the ring caused the emergence of a wave on the opposite side, thus the *remote triggering* of the electrochemical wave was observed.

The Pt working electrode was initially prepared in the passive state by scanning the voltage to a high value of 750 mV (vs. Hg/Hg<sub>2</sub>SO<sub>4</sub> reference electrode placed in the center of the ring) and then the voltage was lowered to a value close to (just before) the value of 220 mV at which the return to the active state would occur; in this way the rather metastable state was created. When the perturbation, in the form of a positive pulse, was applied to trigger Pt electrode (+3 V vs. the working electrodes potential), the system switched locally to the active (low-potential) state and, as expected, two fronts of activation started to propagate along opposite

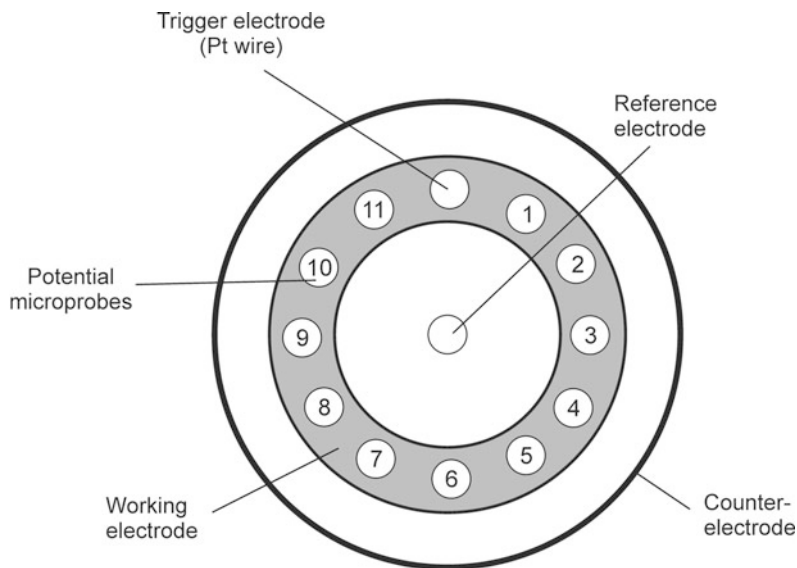


**Fig. 2.39** Schematic view of the electrode setup. The potential microprobes (1 through 11) are separated by  $30^\circ$  angles, and the perturbations were applied with a Pt wire. After [51]. Reprinted from [51] with permission of AAAS

directions of the ring until they met after ca. 200 ms. However, if the negative pulse was applied, instead of expected local stabilization of the double layer potential, its value increased only slightly at positions 1 and 11, but at the opposite site (electrode No. 6) activation occurred, followed by decelerated front propagation. This is the above-mentioned *remote triggering* of the wave.

Of course, such remote response is an experimental proof for a long-range (nonlocal) coupling between different parts of the working electrode, realized through the ionic migration in the solution, under the influence of the electric field. The almost instantaneous manifestation of this coupling is a consequence of a significant difference in time scales of two processes which is the condition for occurrence of such effects: while switching the electrode surface to the active state, requiring the removal of passivating OH species, requires ca. 100 ms, the electric field effects spread with the velocity of light, i.e., require less than  $10^{-9}$  s across the system. Numerical calculations based on theory developed earlier by Christoph et al. [52] and involving the coupling function  $H$  [see description of Eqs. (2.7)–(2.10) for more details] fully confirmed the role of long-range migration coupling in the reported experimental phenomena. Such calculations clearly show how the local perturbation causes the onset of the front propagation from this place, but at a remote distance the perturbation of the reversed direction is induced.

In the course of further studies, Strasser et al. [53] have described the formation of *standing wave oscillations* of the interfacial potential across the ring polycrystalline Pt electrode, monitored by means of equispaced potential microprobes along the electrode, as for the construction shown in Fig. 2.39, with the exception for the absence of the triggering electrode. The Hg/Hg<sub>2</sub>SO<sub>4</sub> reference electrode was placed in the Luggin capillary, the tip of which was located in the center of the working

electrode ring, thus in a configuration ensuring the same potential distribution between the RE and the working electrode, independently of the azimuthal angle. A concentric Pt wire ring served as a counter electrode. Each of 11 potential microprobes consisted of a glass tube with a microcapillary (100–200  $\mu\text{m}$  diameter), hosted a Hg/Hg<sub>2</sub>SO<sub>4</sub> reference electrode and was filled with 0.5 M Na<sub>2</sub>SO<sub>4</sub> solution.

Under such potentiostatic conditions that the oxidation current of formic acid exhibited spontaneous oscillations, the distribution of the electrode potential along the ring electrode exhibited inhomogeneities, both in time and space, with one half of the electrodes in high-potential (passive) state, and the other half—in the low-potential (active) state, periodically interchanging in time. The whole pattern had a form of a standing wave, with the spatial node located close to the position of electrode number 6, for which the amplitude of the oscillations was very low (Fig. 2.40).

The correlation between the shape of period-2 cycle observed in the course of total current and the variation of the electrode potential along the entire ring is shown in Fig. 2.41. This comparison clearly shows that large total currents are associated with pronounced spatial inhomogeneities along the working electrodes, whereas low catalytic activity (low current) correspond to nearly homogeneous potential profiles.

By varying the concentration of a supporting electrolyte (i.e., the solution conductivity) and the external potential one can obtain various patterns, including aperiodic temporal variations of total current associated with corresponding turbulent spatio-temporal patterns along the electrode (but even in this complex regime, the antiphase behavior between opposite points along the working electrode was maintained).

Finally, upon insertion of sufficiently high serial resistance ( $R_{\text{ex}} > 4 \Omega$ ) the synchronization of the potential profile was observed, i.e., any spatial patterns practically ceased and the total current exhibited oscillations correlating with the temporal variations of the electrode potential.

The reader familiar with the content of Sect. 1.2 will realize that conditions of both the pattern formation (potentiostatic control with the reference electrode approaching the WE with the Luggin capillary) and the pattern destruction (increasing external resistance) corresponds exactly to the situation when negative global coupling operates and turns into positive one. Thus, the construction of the theoretical model [53] of the observed experimental phenomena refers to the essential mathematical description of this kind of coupling, in a formalism developed earlier by Christoph et al. [52, 54]. This approach introduces the spatial coupling function  $H_B$  which represents the coupling between two points  $x$  and  $x'$  along the working electrode, and due to the symmetry of the ring electrode geometry it is here the function of  $|x - x'|$ . In terms of this approach, the dynamics of the interfacial potential drop at the working electrode is described in terms of the following dependence:

$$C_d \frac{\partial \phi_{\text{dl}}}{\partial t} = -i_f(\phi_{\text{dl}}) + \frac{U - \phi_{\text{dl}}}{R_{\text{tot}}} + \sigma \int_0^1 H_B(|x - x'|) [\phi_{\text{dl}}(x', t) - \phi_{\text{dl}}(x, t)] dx' \quad (2.7)$$

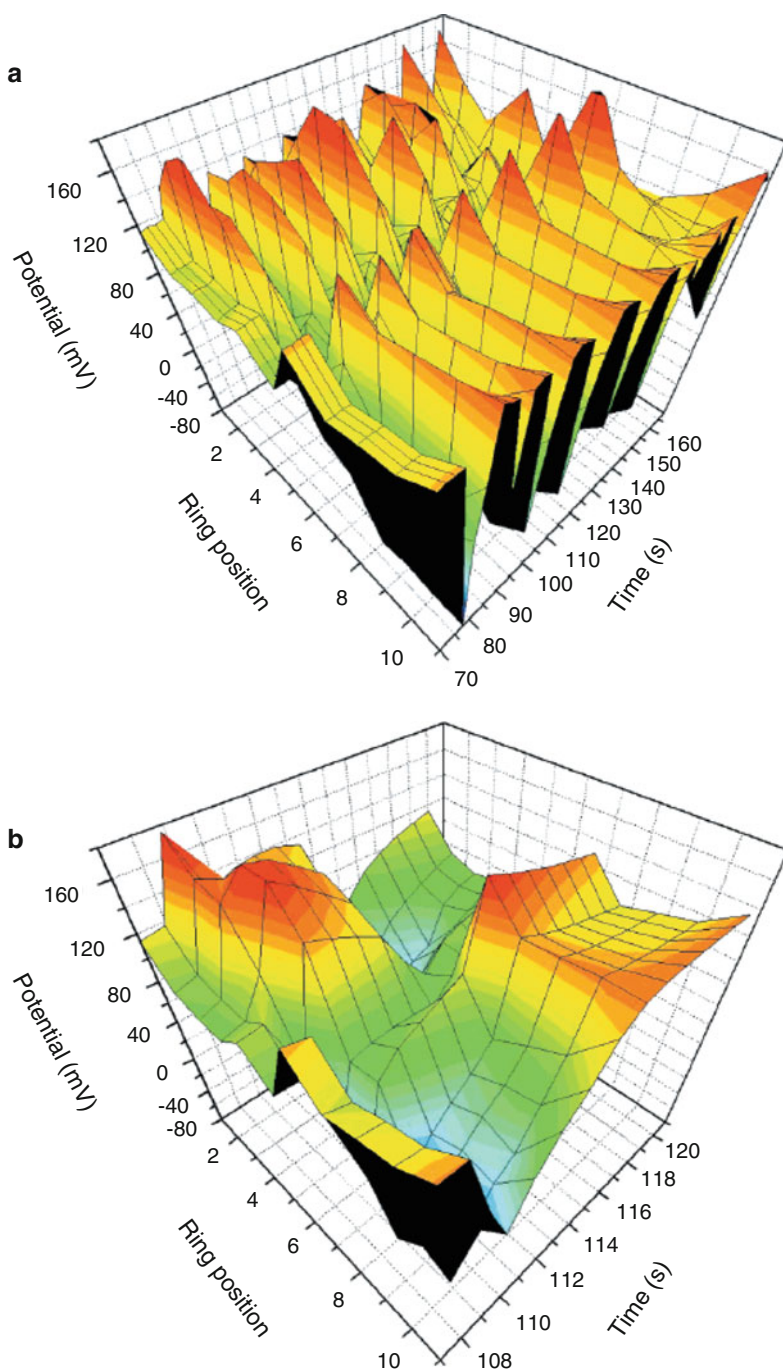


**Fig. 2.40** (a) Spatiotemporal evolution of the local potential in front of the Pt WE during formic acid oxidation under oscillatory total currents. The potential distribution displays an oscillatory standing wave pattern.  $U_{\text{ex}} = 325$  mV, 0.05 M HCOONa/0.025 M  $\text{H}_2\text{SO}_4$ , no stirring, the

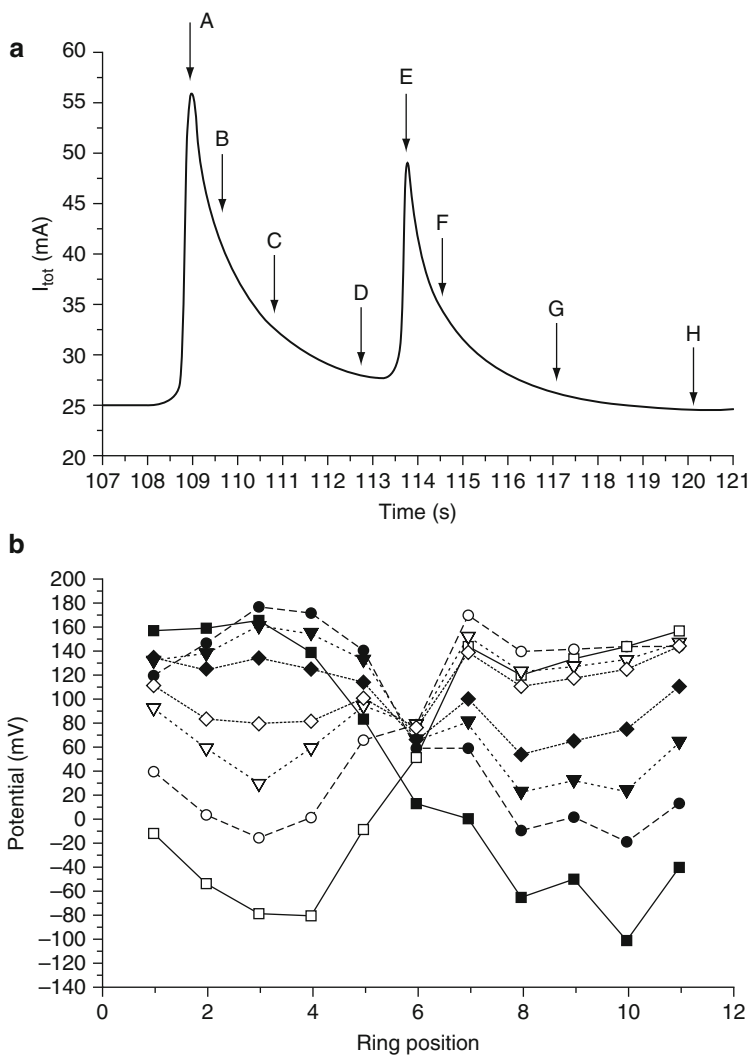


**Fig. 2.41** (a) Blowup of a period-2 cycle in total current  $I_{\text{tot}}$ . The letters indicate eight time instances for which the spatial profiles are given in (b). (b) Spatial potential profiles at subsequent time distances corresponding to a. A (filled squares), B (filled circles), C (filled triangles), D (filled diamonds), E (open diamonds), F (open triangles), G (open circles), and H (open squares). Reprinted with permission from [53]. Copyright 2000 American Chemical Society

**Fig. 2.40** (continued) oscillations have been induced by a homogeneous 200 ms/+200 mV potential pulse applied to the WE. (b) Blowup of one spatiotemporal period given in (a). Reprinted with permission from [53]. Copyright 2000 American Chemical Society

where  $i_f$  is the faradaic current,  $U$  is the external voltage (vs. the reference electrode), and  $R_{\text{tot}}$  is the total resistance. The integral part constitutes the mathematical formulation of a spatial coupling which vanishes for the homogeneous electrode state (since then  $\phi_{\text{dl}}(x', t) = \phi_{\text{dl}}(x, t)$  for any  $x$  and  $x'$ ). On the other hand, for the inhomogeneous state, the value of coupling function quantitatively describes the effect that any location  $x'$  affects the dynamics at the position  $x$ . The value of  $H$  is determined by parameter  $B$  which depends on the external serial resistance  $R_{\text{ex}}$ , on the aspect ratio of WE and RE ( $\beta$ ), being the distance between RE and WE normalized to diameter of the WE, on the inner diameter of the annulus ( $A$ ) and the solution conductivity ( $\sigma$ ):

$$H_B(|x - x'|) = H_0(|x - x'|) + \frac{h^2 B}{1 + hB} \quad (2.8)$$

with

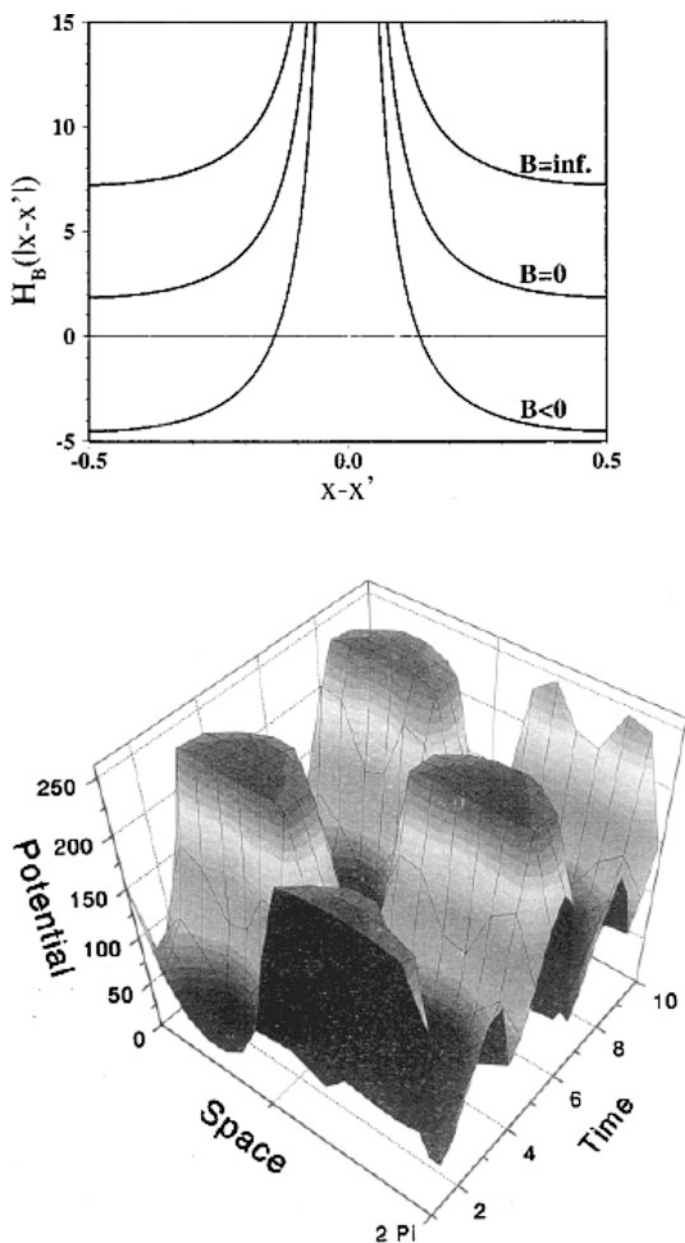
$$h = - \int_0^1 H_0(|x - x'|) dx' \quad (2.9)$$

and

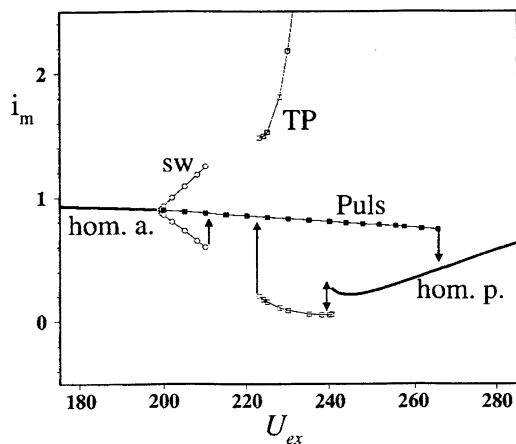
$$B = R_{\text{ex}} \pi \sigma (1 - A^2) - \sqrt{1 + \beta^2} + \sqrt{A^2 + B^2} \quad (2.10)$$

Figure 2.42a shows the course of the  $H_B(|x - x'|)$  function for three different values of parameter  $B$ :  $B = 0$  (or slightly negative), approximating the condition of the absence of external resistance, with large distance between WE and RE;  $B < 0$  for sufficiently small distance between WE and RE, creating conditions for significant negative global coupling and  $B > 0$ , corresponding to the presence of a sufficiently large external resistance. In fact, the negative sign of  $H$  indicates the regions of the working electrode subject to negative global coupling which is thus manifesting itself for  $B < 0$  at the remote locations of the WE. Accordingly, Fig. 2.42b shows the theoretical oscillating *standing wave* of the interfacial potential, calculated from the model involving two dynamical variables: the interfacial potential (fast variable) and the surface concentration of an electroactive species (slow variable), for  $B < 0$  (see caption for detailed values of particular parameters).

From the point of view of nonlinear dynamics, the birth of the oscillatory standing wave occurs via the *wave bifurcation* (Turing's second bifurcation) of the stationary state that precedes the Hopf bifurcation. Most probably this is the first report on the formation of oscillatory standing waves in electrochemical systems. These and other dynamical regimes are collected on a one-parameter bifurcation diagram constructed from the dependence of the maximum/minimum total current density  $i_m$  of the respective patterns on the external voltage  $U_{\text{ext}}$ , at constant total dimensionless resistance  $R_{\text{tot}}$  (Fig. 2.43); the region of occurrence of standing wave region is there abbreviated by sw. The wave bifurcation occurs at  $U_{\text{ex}} \approx 200$ , the first Hopf



**Fig. 2.42** (a) Coupling function  $H_B$  for different values of the parameter  $B$ ;  $H_B$  represents the coupling between two points  $x$  and  $x'$  along the interface with distance  $x-x'$ . (b) Calculated oscillating standing wave of the interfacial potential in the two-variable reaction–migration model past a wave bifurcation. For the mathematical form of the function and the parameters, see original reference. Reprinted with permission from [53]. Copyright 2000 American Chemical Society



**Fig. 2.43** One-parameter bifurcation diagram of the model discussed, at  $R_{\text{tot}} = 40$ . The maxima and minima of the total current density  $i_m$  of the occurring patterns are plotted against the dimensionless outer applied potential; sw—oscillatory standing waves, hom. a. = homogeneous active stationary state. TP—target patterns, Puls = pulse solution branch, hom.p. = homogeneous passive stationary state. All other parameters as for Fig. 2.42b. See [53] for further details. Reprinted with permission from [53]. Copyright 2000 American Chemical Society

bifurcation—at  $U_{\text{ex}} \approx 217$ , and a second Hopf bifurcation—at  $U_{\text{ex}} \approx 241$  (both indicated by the arrows). In certain regions of external voltage, one observed also bistability: target patterns/pulse and pulse/homogeneous passive stationary state.

It is useful to comment in more detail the existence of the wave bifurcation in the above system. In principle, this is a second bifurcation predicted by Alan Turing in his seminal paper [55], after the first one predicting the stationary patterns, described in Section 1.1.4. In this second bifurcation, oscillatory standing waves are born, like in the experimental system and its model described earlier. One should note, however, that in chemical reaction-diffusion systems (RDS), for the wave bifurcation to occur two dynamical variables (species) are not sufficient—there should be present at least a third species, with a diffusion coefficient determining the intrinsic wavelength of the time-dependent solution of differential equations [56–58]. The present electrochemical system is analyzed in terms of two-variable model, so apparently the wave bifurcation should not occur. However, one can prove [53] that for electrochemical systems with negative global coupling, both Turing bifurcations require *one variable less* than in RDS, i.e., 1 and 2 instead of 2 and 3, respectively. The instabilities occur then with the largest possible wavelength because of the very fast coupling. As a further consequence of that, those complex behaviors that were predicted for three-variable RDS (i.e. target patterns, traveling pulses) should be obtained for the two-variable electrochemical reaction–migration system. The bifurcation diagram, shown in Fig. 2.43, confirms that conclusion. Another example is the electrodisolution of Co in acidic media [27, 52].

In further studies, Lee et al. [59] have analyzed the oscillatory oxidation of formic acid on a Pt electrode modified by Bi deposition, using the ring Pt electrode. In the presence of Bi adatoms, the current density increased about five times, since less adsorbed CO was then formed, being presumably removed by Bi–oxygen species. In spite of this modification of one of the reaction pathways, the galvanostatic oscillations, born via the Hopf bifurcation, were observed. Accordingly, impedance measurements indicated the hidden negative differential resistance, confirming that the oscillator falls into Class IV category (HN-NDR systems). The electrochemical source of this hidden NDR is presumably caused by the fast oxidation of Bi adatoms:  $\text{Bi}_{\text{ad}}\text{OH}^- \rightarrow \text{BiO}_{\text{ad}} + 2\text{e}^- + \text{H}^+$ . Cyclic voltammetric experiments revealed also the explicit NDR region which is presumably caused by, increasing with positive potential, adsorption of oxygen (this NDR gives rise to oscillations in the CV experiment in the presence of sufficient ohmic potential drops).

An interesting extension of these experiments was achieved again by placing 11 microprobes of the potential along the ring Pt electrode (cf. Fig. 2.39), in order to monitor the spatiotemporal evolution of the interfacial potential [59]. Figure 2.44 shows the temporal current response and a two-dimensional space–time plot of the local potential along the Pt ring electrode, for constant outer potential ( $U$ ) applied. In particular, black and white zones mean that the narrow pulse domain of high activity (relatively low interfacial potential) is continuously traveling on the ring surface.

Comparison of Fig. 2.44a, c shows that the oscillations of the total current are associated with the periodical change of the size and shape of the traveling potential pulse (caused by imperfection of the electrode). This is an impressive result which shows the role of spatial inhomogeneities in the evolution of temporal dynamics.

Very recently, Christoph et al. [60] have developed theoretical and experimental studies of the oscillatory oxidation of formic acid on a thin Pt ribbon electrode which also showed the spatiotemporal self-organization. The source of the system's inhomogeneity is the enhancement of the current density near the edges of ribbon (as for all disk electrodes), so the interfacial potential drop is inhomogeneously distributed. The theory underlining the spatiotemporal phenomena involves the spatial distribution of both the faradaic and migration current in the three-dimensional space, assumed as a geometry of a ribbon electrode. The dual-path mechanism of the formic acid oxidation (cf. Chap. 5, volume I) was further incorporated in the model, i.e., the CO is treated as a surface poison which is removed by interaction with  $\text{OH}_{\text{ads}}$  formed at sufficiently positive potentials. For the detailed mathematical construction, the reader is advised to inspect the original reference. Here only exemplary results of the calculations of the spatiotemporal evolution of the interfacial potential drop are shown (Fig. 2.45).

For comparison of these theoretical predictions with the experiment, a specially designed electrode arrangement was assembled. A smooth polycrystalline Pt ribbon with a width of 4.0 mm and a length of 58.0 mm was used as the working electrode (WE). The counter electrodes (two Pt coils) were placed 80 mm above the WE. The tip of the Luggin capillary hosting a  $\text{Hg}/\text{Hg}_2\text{SO}_4$ ,  $\text{K}_2\text{SO}_4$  (saturated) reference electrode was placed at the symmetric axis above the center of the ribbon in various

**Fig. 2.44** (a) Current profile at constant outer potential ( $U$ ) of + 150 mV; (b) contour plot (two-dimensional) of the local interfacial potential during the current oscillations; and (c) time sequence of traveling pulse along the ring Pt electrode. *Black* and *white* represent the activating and passivating state of the Pt electrode, respectively. Electrolyte is 0.1 M HCOONa/0.033 M H<sub>2</sub>SO<sub>4</sub> [59]. Reprinted from [59], Copyright 2001, with permission from Elsevier

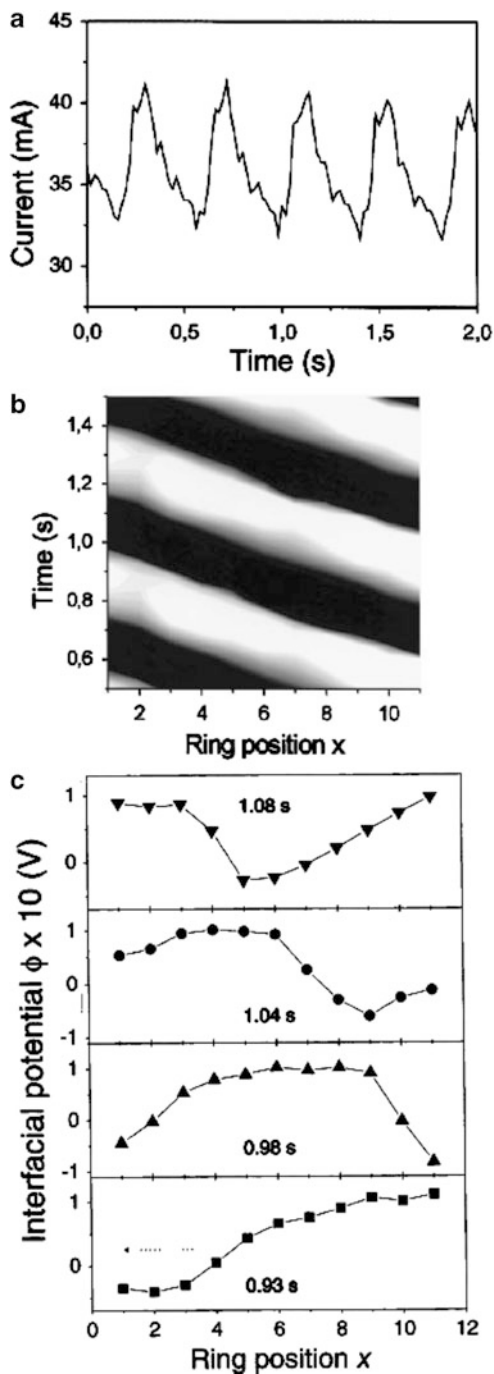
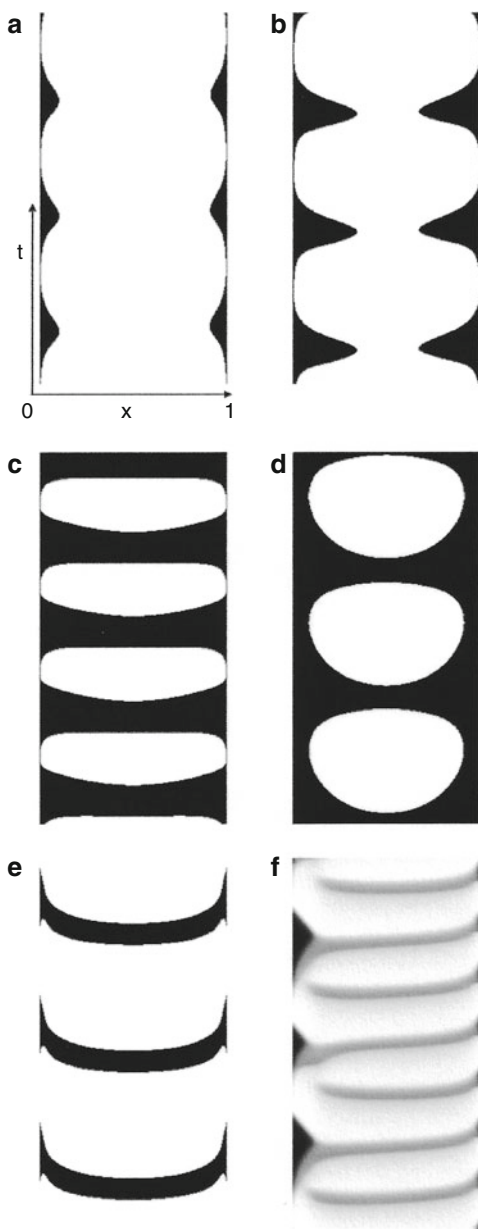


**Fig. 2.45** Spatiotemporal evolution of the double layer potential on a thin ribbon electrode for a distant position of the RE. Simulations were carried out with 200 equidistant grid points using the Euler algorithm. The passive phase corresponds to the *black color regions* unless stated otherwise, external voltage  $E_0$  is given in the units of mV, the average resistance  $\langle \rho \rangle$  in units of  $\Omega \text{ cm}^2$ . (a) In-phase edge oscillations ( $\langle \rho \rangle = 50$ ,  $E_0 = 440$ ); (b) larger edge oscillations at increased outer potential ( $\langle \rho \rangle = 50$ ,  $E_0 = 442$ ); (c) spatially inhomogeneous oscillations on the entire electrode ( $\langle \rho \rangle = 50$ ,  $E_0 = 454$ ); (d) center oscillations with stationary edge areas ( $\langle \rho \rangle = 30$ ,  $E_0 = 428$ ); (e) oscillations with active and passive fronts emerging from the center (target pattern with source point  $x_{\text{SP}} = 0.5$  at  $\langle \rho \rangle = 300$ ,  $E_0 = 640$ ); (f) coexisting asymmetric mixed oscillations. The passive state ( $E \approx E_0 \equiv U$ ) near the (*left*) edge at  $x = 0$  is depicted with black color, whereas the passive/active phase of the limit cycle is described with *gray/white color* ( $\langle \rho \rangle = 300$ ,  $E_0 = 640$ ). See [60] for more details. Reprinted from [60], Copyright 2009, with permission from Elsevier



distances. The pulse electrode (PE), a Pt wire of 2 mm length (with remaining part sealed in glass), was placed above the WE up to ca. 1 mm. For the measurements of the time-dependent local interfacial potentials on WE, eight microprobes were placed along the ribbon electrode (at the distance of 0.2 mm). The perturbation

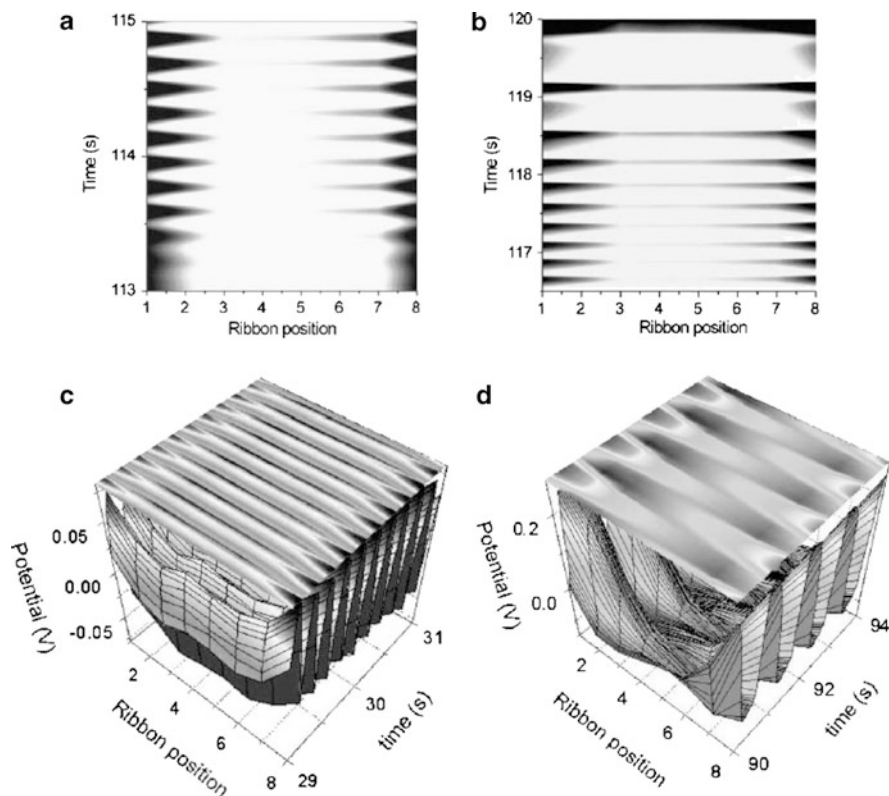


**Fig. 2.46** Experimentally observed spatiotemporal distribution of the double layer potential. (a) Distant RE (measured by the vertical distance of RE to the WE, normalized to the WE ribbon length,  $\beta = 1.5$ ) and low outer potential ( $E_0 = 540$  mV) leading to edge oscillations; cf. Fig. 2.45a. (b) Distant RE ( $\beta = 1.5$ ) and higher outer potential ( $E_0 = 580$  mV) with a larger oscillatory region; cf. Fig. 2.45b; (c) in-phase oscillations at a decreased distance of the RE ( $\beta = 0.5$ ); cf. Fig. 2.45c; (d) sufficiently small distance of the RE ( $\beta = 0.3$ ) inducing negative coupling and therefore creating antiphase oscillations,  $E_0 = 215$  mV (see [60] for more details). Reprinted from [60], Copyright 2009, with permission from Elsevier

of the steady state was achieved by applying a short pulse at appropriate position. Experimental results, shown in Fig. 2.46, were interpreted as revealing good concordance with essential theoretical predictions. Again, these modelings and experiments emphasize the necessity of consideration of the spatiotemporal inhomogeneities in the system dynamics, which effect would remain hidden, if only the variations of the average, total current or the effective electrode potential were considered. The reader interested in more detailed characteristics of the spatiotemporal self-organization on ribbon electrodes is advised to consult the original paper by Christoph et al. [60].

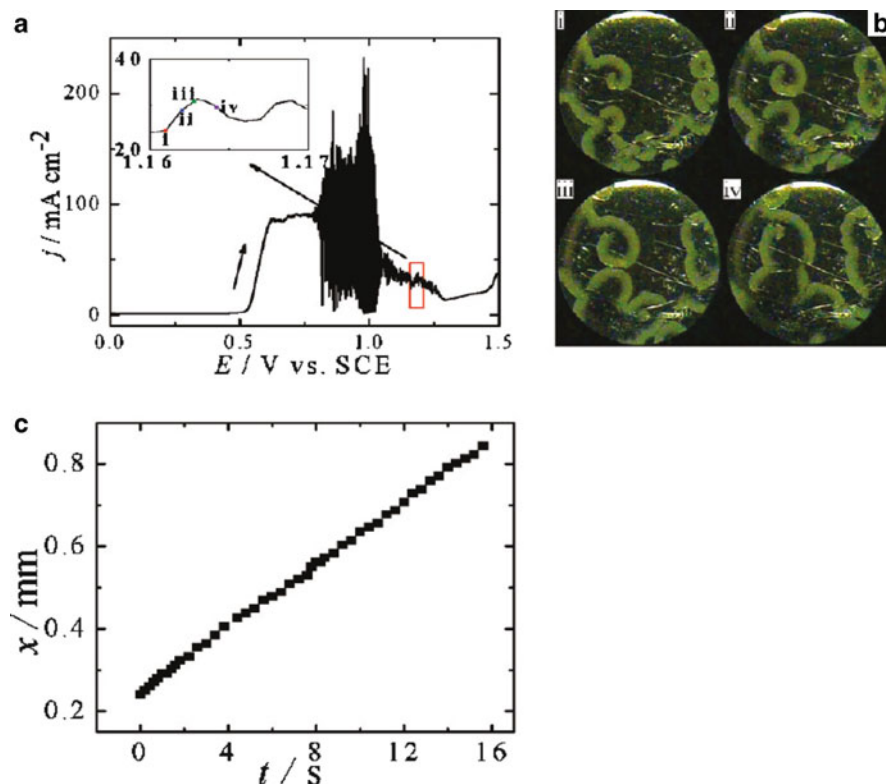


**Fig. 2.47** Linear potential sweep, snapshots of the evolution of pulses, and position–time plots of pulses. The scan rate of applied voltage is  $0.1 \text{ mV s}^{-1}$ . The time interval between i and ii is 9 s, ii and iii is 6 s, iii and iv is 16 s. Reprinted with permission from [61]. Copyright 2011 American Chemical Society

## 2.9 Spatiotemporal Patterns in Sulfide Electrooxidation

The complex oscillatory electrooxidation of  $\text{S}^{2-}$  ions, described in Sect. 5.7 of volume I, can become a source of various spatiotemporal patterns at the Pt electrode (2 or 5 mm diameter), as Varela, Epstein et al. have recently reported [61]. The Pt wire and SCE were employed as the counter and reference electrodes, respectively, and the solution studied was 1 M  $\text{Na}_2\text{S}$  at  $20^\circ\text{C}$ . During the electrochemical experiment, the working electrode surface was monitored with a CCD camera. Figure 2.47 shows representative experimental results: when the Pt potential entered the N-NDR oscillatory region, pulses and spirals emerged, which corresponded, respectively, to points i–iv in Fig. 2.47a. The propagation velocity of the pulses was estimated as  $0.039 \text{ mm s}^{-1}$ . Depending on experimental conditions also fronts, labyrinths, twinkling eye-like patterns (presumably observed for the first time as the experimental, not only theoretically predicted phenomena), and homogeneous oscillations were reported. High scan rates and high series resistances favored pulses, whereas low scan rates and external resistance led to

homogeneous oscillations of deposition and dissolution, with twinkling eyes and labyrinthine patterns occurring in parameter regions between synchronized oscillations and pulse waves [61].

## 2.10 Turing Patterns in Electrochemical Systems

One of the most recent impressive discoveries in the area of electrochemical systems is finding the conditions of the formation of stationary patterns of the Turing type. The principles of formation of such patterns due to the coupling of chemical kinetics with diffusion of reagents exhibiting various diffusion coefficients were described in Sect. 1.1.4. In terms of the concept of the activator–inhibitor dynamical system, the Turing patterns emerge when the inhibitor, the production of which is accelerated by the activator, diffuses faster than the activator and in this way the spatial progress of the activator becomes hindered. In electrochemical systems, as described in Sect. 1.2.3.4, such patterns can emerge as a consequence of the interaction between the electrochemical process with S-NDR characteristics and the long-range, migration coupling, as Mazouz and Krischer have predicted only in the year 2000 [62]. The principle of the concept was that the condition of different rate transport of the activator and the inhibitor is particularly easy to realize in electrochemical systems, when besides diffusion, the migration (usually much faster transport) is present. In S-NDR systems the electrode potential is typically a fast inhibitor, while the chemical species involved in the autocatalytic loop is an activator which is transported by diffusion.

At this point it is useful to realize that stationary character of the patterns observed in the experiment does not mean that the Turing patterns were formed, so not every stationary pattern is a Turing pattern. For example, stationary patterns observed during the reduction of  $\text{S}_2\text{O}_8^{2-}$ , which is not the S-NDR, but the N-NDR system (cf. Sect. 2.2) [24] cannot be classified as Turing ones. As described earlier, in the case of peroxodisulfate reduction, the formation of two spatial domains on the working electrode was due to the negative global coupling, caused by the external circuit, and not only by the migrations of ions in the electrolyte which is one of the major factors deciding the emergence of Turing patterns.

Coming back to Turing-like patterns, theoretical predictions of the conditions of their occurrence in electrochemical systems were soon followed by their experimental verification, reported in 2001 by the same group of researchers [63]. For the experimental detection of such patterns, the surface plasmon microscopy was applied using methodology described in [1] and in the setup shown in Fig. 2.48.

The periodate reduction on Au(111) electrodes in the presence of camphor as an adsorbing inhibitor was chosen as an electrochemical system. Camphor adsorbed on Au(111) surface exhibits two first-order phase transitions, one around +0.1 V and the other one around −0.75 V (vs. Hg–Hg<sub>2</sub>SO<sub>4</sub> reference electrode). In the potential region from −0.3 to −0.7 V, camphor forms a condensed film on the electrode surface, causing the strong inhibition of the reduction of periodate ions, while at more negative potentials the electrode coverage is very low. Upon

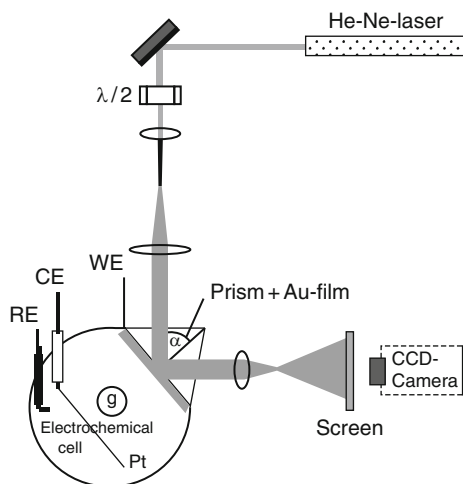


**Fig. 2.48** Experimental setup for imaging patterns at the electrode/electrolyte interface by means of surface plasmon microscopy (*top view*). WE: working electrode [a ~50-nm-thick Au film evaporated onto a glass plate (B270) that was brought into optical contact with a glass prism; the area of the WE exposed to the electrolyte was 8 mm by 30 mm]. CE: counter electrode (a Pt wire, wound to a spiral of the same size as the working electrode and placed parallel to it at a distance of ~4 cm). RE: Hg/Hg<sub>2</sub>SO<sub>4</sub> reference electrode. (All voltages are given with respect to this reference electrode). G: gas inlet for Ar bubbling. (The mass transport was achieved by means of gas bubbling). The electrode was irradiated from behind by a broadened, p-polarized He–Ne laser beam and imaged with a charge-coupled device (CCD) camera. Before each experiment, the film was flame annealed several times in a gentle butane flame, resulting in a film with a high degree of (111) facets, as revealed by electrochemical characterization. From [63]. Reprinted with permission of AAAS

cyclic variation of the electrode potential in the regions covering either the first or the second phase transition, one observes the hysteresis in cyclic voltammetry of periodate ions. According to the general characteristics of the S-NDR systems, the electrode coverage with camphor is here an activator, while the electrode potential is an inhibitor in this activator–inhibitor dynamical system. Experimentally it is manifested in the following way: upon the shift of the electrode potential from negative towards positive values, an increase of camphor coverage occurs until the critical value, at which sharp first-order transition to a dense camphor film takes place, due to attracting lateral interactions between the adsorbate particles. This causes the inhibition of periodate reduction, i.e., the decrease in its faradaic current which in turn, under potentiostatic conditions and *in the presence of uncompensated serial resistance*, makes the electrode potential more negative. At such potential camphor is desorbed, so the negative feedback loop is created: the autocatalytic growth of camphor film causes, through the changes of the electrode potential, the decrease in surface camphor concentration.

For this experimental system, *stationary patterns* were detected on the electrode surface, using surface plasmon microscopy for such diluted NaClO<sub>4</sub> solution as a supporting electrolyte that the ohmic potential drop exceeded the width of the bistable region on the *I–E* characteristics of periodates. Then, this

dependence took a quasi-linear shape of a positive slope (cf. concordance with the theoretical predictions of Turing patterns in Sect. 1.2.3.4 and Fig. 2.10, vol. I). In other words, patterns were observed indeed under conditions when the S-shaped  $I$ - $E$  region has deformed into the single-valued dependence. Representative examples of such “spot-like” patterns are shown in Fig. 2.49. It is important to note that these patterns remained unchanged for the fixed external potential, hence they were stationary and stable.

By varying the voltage and specific conductivity of the solution, the diagram of occurrence of those patterns was constructed, reasonably well concordant with theoretical calculations, made according to the model, outlined in Sect. 1.2.3.4.

It is here useful to remember that one of the essential features of the Turing patterns is the independence of their wavelength of the size of the system<sup>1</sup>, but the dependence only on the kinetic and diffusion parameters of the system. In the opinion of the authors of [63], the formation of such Turing patterns can find potential applications in manufacturing structured electrodes (like those developed for fabrication of (bio)sensors). In such procedure, one could adjust the wavelength of the designed patterns by choosing different faradaic reactions, adsorbates, or modifying the temperature (the faster the faradaic reaction and the dynamics of the adsorbate system, the smaller are the patterns). If successful, such an approach would be an example of application of nonlinear dynamics in the materials science. Also, of course, recognizing the mechanisms of formation of Turing patterns in electrochemical systems can deepen our understanding of pattern formation in biological systems, in which the gradient of electric potential exist. This problem was not existing in the description of Turing patterns for purely chemical systems without migration transport explicitly considered.

The next example of Turing-like patterns in electrochemical systems was found in 2003, also by the group of Krischer [64, 65], for the CO electrooxidation on Pt which also exhibits the S-shaped stationary  $I$ - $E$  dependence under potential control. As described in Sect. 5.2 of volume I, in this case the S-NDR characteristics were explained in terms of an autocatalytic reaction cycle, caused by the competitive Langmuir–Hinshelwood mechanism between surface-bonded CO and OH species. The experimental setup [65] involved a rotating ring polycrystalline Pt electrode ( $\omega = 1,200$  rpm), of a 1 mm width and 85 mm mean circumference, embedded in cylindrical Teflon pieces. The local electric potential in the electrolyte close to WE was recorded along the angular direction by means of a stationary microprobe. The WE rotated over the microprobe, which allowed the temporal evolution of the angular potential distribution in front of the Pt ring to be obtained in situ. Experiments were performed for low-conductivity electrolytes, e.g., 2 mM perchloric acid [64, 65] which ensured relatively high ohmic drops and appropriate deformation of the  $I$ - $U$  dependence, being in certain range even quasi-linear, as controlled predominantly by the solution resistance. In this way, the conditions for the formation of spatial Turing patterns were achieved. In fact, at  $U = 0.2$  V (vs. Hg–Hg<sub>2</sub>SO<sub>4</sub> electrode) when the rate of electrooxidation of CO attained significant

---

<sup>1</sup> An extension of the Turing model for the case when the system's size affects the pattern formation, was described by Murray [9].

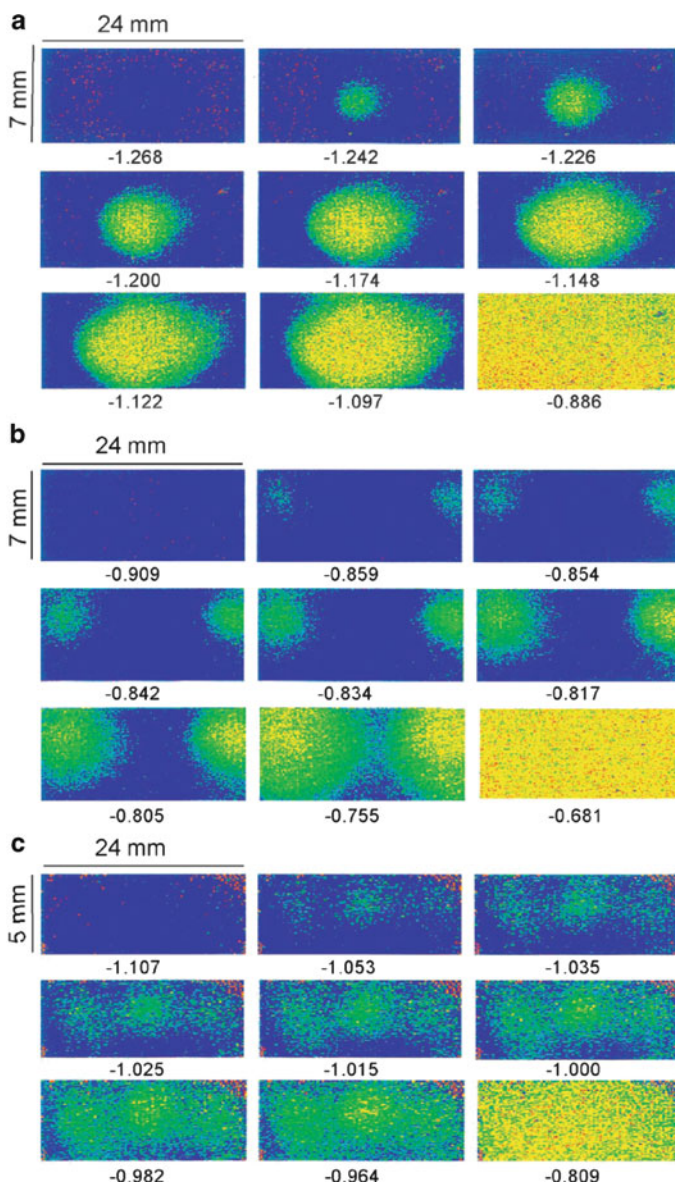


**Fig. 2.49** Patterns emerging in different electrolyte compositions: (a) 5 mM camphor, 0.5 mM  $\text{NaClO}_4$ , and 0.5 mM  $\text{NaIO}_4$ ; (b) 5 mM camphor, 1 mM  $\text{NaClO}_4$ , and 1 mM  $\text{NaIO}_4$ ; and (c) 5 mM camphor, 0 mM  $\text{NaClO}_4$ , and 1 mM  $\text{NaIO}_4$ . In all three cases, the corresponding  $I-U$  curve was single valued. The numbers given below the images are the potential values at which the images were obtained during a potential scan. When holding the potential at those values, the patterns did not change with time, i.e., under these conditions, stationary patterns existed on the electrode. *Blue colors* indicate a nearly camphor-free electrode; orange and *yellow colors* indicate a high camphor coverage (The measured intensities are normalized at each point). From [63]. Reprinted with permission of AAAS

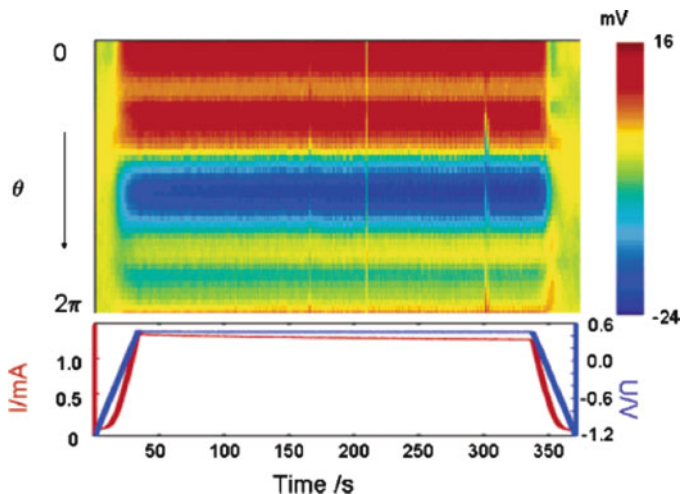


**Fig. 2.50** *Top:* Position–time plot of the inhomogeneous part of the potential probe signal during bulk CO electrooxidation in 2 mM KOH. *Bottom:* Corresponding applied voltage (blue line) and total current (red line) vs. time. Rotation speed of the electrode  $\omega = 1,200$  rpm. Reprinted with permission from [65]. Copyright 2005 American Chemical Society

values, stationary potential patterns formed spontaneously. Both small (ca. 15 mV peak to peak) and large amplitude (up to 200 mV) potential patterns were found depending on the applied voltage. It was also possible to model these patterns in terms of spatially extended mechanism for CO electrooxidation proposed by Koper et al. [49] and outlined in Sect. 5.2 of volume I. These phenomena were studied more thoroughly for both diluted acidic and basic supporting electrolytes [65]. Figure 2.50 shows representative experimental result, whereas Fig. 2.51 shows successful modeling of relevant phenomena. In the model, based again on achievements by Koper et al. [49] and Strasser et al. [66], the diffusion transport of CO was implemented in a way involving two diffusion coefficients:  $D_1$  for the transport from the bulk solution and  $D_2$  for its radial diffusion at the electrode, with  $D_2/D_1 = 100$ :

$$\frac{\partial c_s}{\partial t} = -\frac{2S_{\text{tot}}}{\delta} v_{\text{CO,ads}} + \frac{2D_1}{\delta^2} (c_b - c_s) + D_2 \frac{\partial^2 c_s}{\partial x^2} \quad (2.11)$$

where  $c_s$ —surface concentration of CO on the solution side,  $c_b$ —bulk concentration of CO,  $v_{\text{CO,ads}}$ —the rate of CO adsorption,  $S_{\text{tot}}$ —maximum surface concentration of adsorption sites ( $2.2 \times 10^{-9}$  mol cm $^{-2}$ ),  $\delta$ —thickness of the diffusion layer,  $D_1 = 5 \times 10^{-5}$  cm $^2$  s $^{-1}$  and  $D_2 = 5 \times 10^{-3}$  cm $^2$  s $^{-1}$ ; coordinate  $x$  is parallel to the surface of the working electrode, while the concentration gradient in the solution developed along the perpendicular  $z$  coordinate. The other three partial differential equations describe the surface dynamics of the interfacial potential drop  $\phi_{\text{dl}}(x, t)$ , the electrode coverage  $\theta_{\text{CO}}(x, t)$ , and the electrode coverage  $\theta_{\text{OH}}(x, t)$ , respectively. Further details of the model the reader can find in original reference [65].

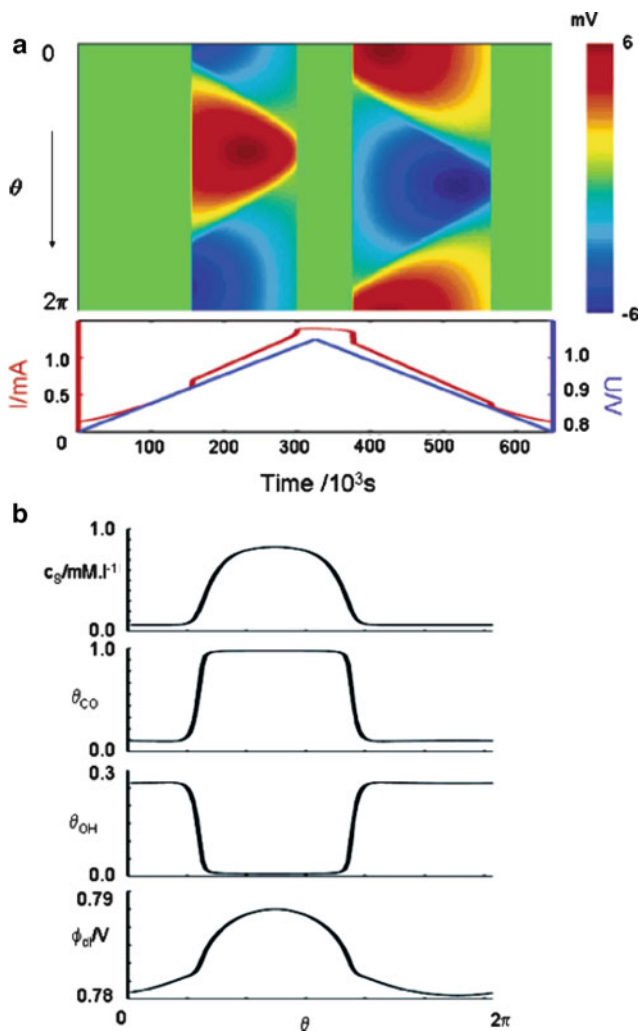


**Fig. 2.51** (a) *Top*: Position–time plot of the inhomogeneous part of the calculated stationary electrode potential,  $\phi_{dl}$ , during a cyclic change in  $U$ .  $\delta = 0.0067$  cm (diffusion layer thickness). See [65] for remaining parameters. *Bottom*: corresponding total current in red and of  $U$  in blue. (b) Calculated spatial distribution of the different variables:  $c_s(\theta)$ ,  $\phi_{dl}(\theta)$ ,  $\theta_{OH}(\theta)$  and  $\theta_{CO}(\theta)$  and plotted for  $U = 0.975$  V. Reprinted with permission from [65]. Copyright 2005 American Chemical Society

## 2.11 Dendritic Patterns in Metal Electrodeposition

### 2.11.1 Dendritic Deposition on Solid Surfaces

Studies of electrodeposition of metals on different surfaces are obviously an important problem in electrochemical industry, and finding the factors determining the

morphology of the deposits is of primary importance. Here we shall focus on the self-organized patterns of deposits, which can take, among others, the fractal shape. Such patterns can be important also for understanding of biological morphogenesis, as they resemble some structures observed in a living nature. Since they develop under nonequilibrium conditions, i.e., in a mass diffusion field, a thermal diffusion field, or an electrostatic potential field, etc., generally described in terms of Laplace equations, the phenomena described below can be understood as electrochemical model of morphogenesis in the Laplacian field [67, 68]. With respect to biological systems, the growth of bacterial colonies in Petri dish is a representative example of such patterns [69, 70].

The formation of fractal- or dendrite-like patterns of electrodeposited metals is a well-known phenomenon. Systematic studies of them, reported for the electrochemical cells of radial geometry, have been published, among others, by Sawada et al. [71] and Grier et al. [72]. More recently, Kuhn and Argoul [73] have described, both experimentally and theoretically (in terms of the diffusion-limited aggregation approach, see also below), the ramified silver aggregates produced in thin-gap cells using a redox reaction between metallic copper and  $\text{Ag}^+$  ions in solution. In turn, Trigueros et al. [74] have presented a study of dendritic patterns formed during the zinc electrodeposition for parallel arrangement of flat electrodes. Depending on experimental conditions, e.g., voltage applied, electrolyte concentration, solution thickness, electrode geometry, etc., different morphologies of electrodeposits were obtained, ranging from largely disordered fractals to well-ordered anisotropic dendritic structures. These results will be briefly summarized here.

The thin-layer electrolytic cell consisted of the electrolyte ( $\text{Zn}^{2+}$  salt) solution sandwiched between two 5 mm thick glass plates, and confined between the cathode and anode, being two parallel copper wires 3.5 cm long, separated by a distance of 3 cm. The growth of zinc electrodeposits occurred after applying an appropriate constant voltage between these electrodes. The deposited patterns were recorded through a stereo zoom microscope connected to a standard video camera and transferred to a PC-based image analysis system. The digitization was performed by means of real-time image digitizer. Figures 2.52–2.54 show exemplary patterns of deposited Zn: the so-called homogeneous ones, meaning the tree-like, densely branched deposits with a well-defined front and more complex, dendritic patterns.

Systematic studies of these patterns allowed to elaborate the morphology diagram shown in Fig. 2.55. Also mixtures of those patterns and transitions between them, during prolonged electrolysis, were reported. The review of all possible patterns of electrodeposited zinc includes its following types [74]: (a) compact deposits obtained at low potentials; (b) ramified structures with a well-defined outer front, called above as “homogeneous” ones, and formed at low  $\text{Zn}^{2+}$  concentrations over a wide range of applied potentials; (c) dendrites, formed at higher  $\text{Zn}^{2+}$  concentrations; and either (d) open ramified, fractal-like deposits, or (e) mixed patterns with characteristics of dendritic backbones and disorderly ramified side branches, both observed at the highest  $\text{Zn}^{2+}$  concentrations. Calculations of the

**Fig. 2.52** Dendritic pattern observed at  $[\text{Zn}^{2+}] = 0.07 \text{ M}$  and  $\Delta V = 9.0 \text{ V}$ ; growth time  $t = 5 \text{ min}$ . Reprinted from [74], Copyright 1991, with permission from Elsevier

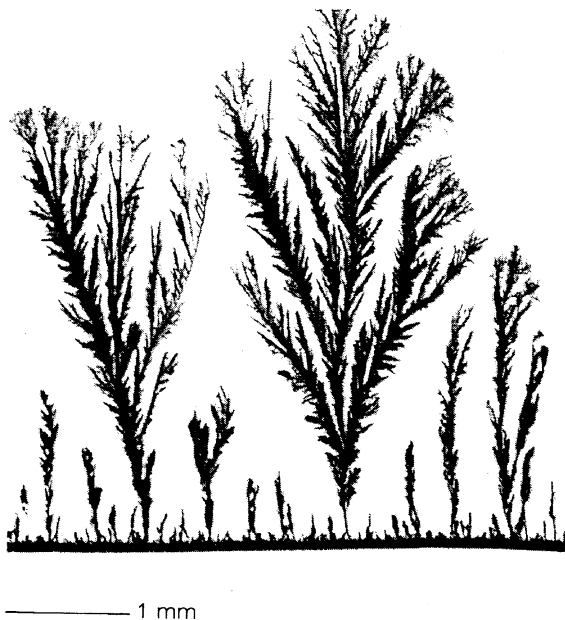
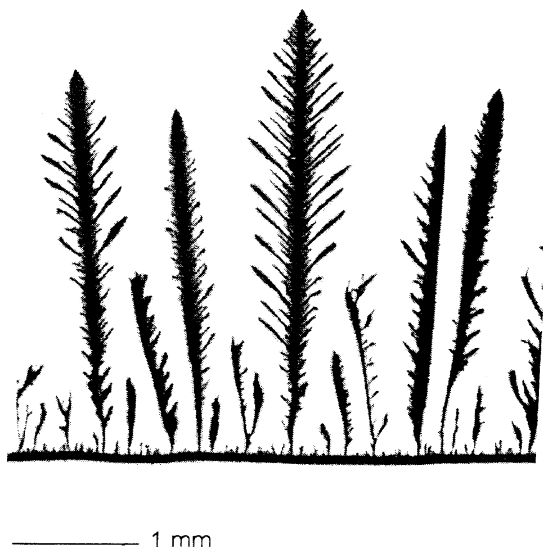


**Fig. 2.53** Self-similar, open ramified pattern observed at  $[\text{Zn}^{2+}] = 0.4 \text{ M}$  and  $\Delta V = 6.0 \text{ V}$ ; growth time  $t = 20 \text{ min}$ . Reprinted from [74], Copyright 1991, with permission from Elsevier

fractal dimensions for various patterns yielded the (typical for this phenomena) average value  $D_q = 1.61 \pm 0.02$ .

Deposited patterns of such morphology are typically numerically modeled in terms of the DLA (*Diffusion Limited Aggregation*) formalism based on the



**Fig. 2.54** Mixed pattern observed at  $[\text{Zn}^{2+}] = 0.4 \text{ M}$  and  $\Delta V = 10 \text{ V}$ ; growth time  $t = 10 \text{ min}$ . Reprinted from [74], Copyright 1991, with permission from Elsevier

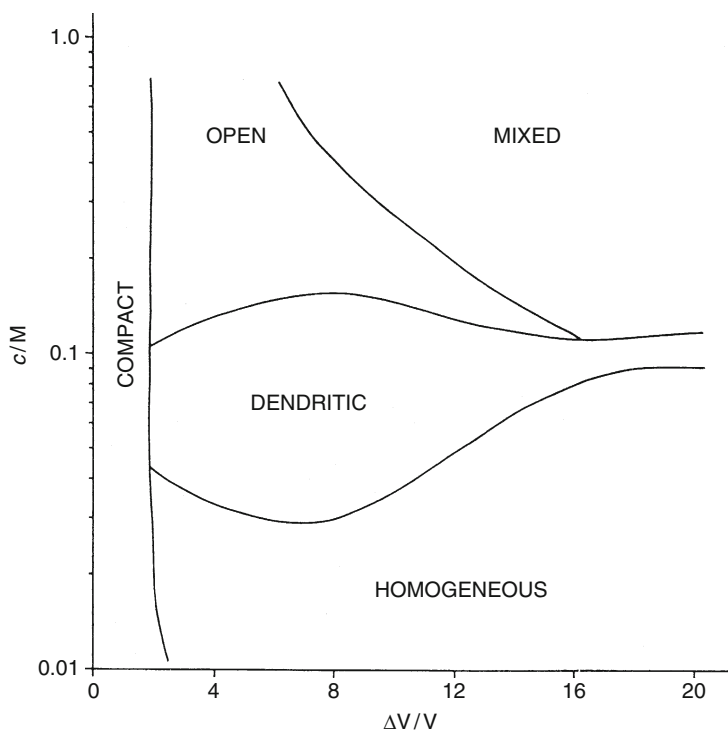


**Fig. 2.55** Morphological diagram for the various patterns obtained in the zinc electrodeposition under appropriate experimental conditions. Reprinted from [74], Copyright 1991, with permission from Elsevier

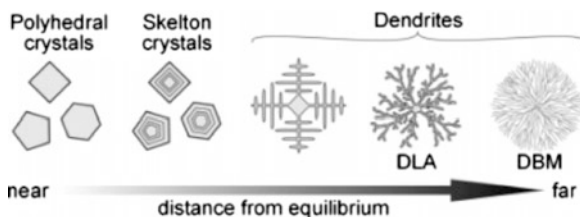


**Fig. 2.56** Schematic illustration of a correlation between the distance of the formation conditions from the equilibrium and the morphologies of formed crystals. Reprinted with permission from [83] Copyright 2007 American Chemical Society

following two assumptions. The first one postulates the random walk of ions on the two-dimensional plane, while the second one claims that at every collision between the walking ion and the electrode, the ion is immediately reduced and stays there in a form of neutral atom, composing the metal phase (cf. e.g., [71, 75–77]).

One can pose a question, whether it is possible to report synchronization of the dendrite electrodeposition with the oscillatory course of the electrode process. Recently, Nakanishi et al. have reported that the electrodeposition of some metals under diffusion-limited conditions gives rise to nonlinear electrochemical oscillations, accompanied by formation of dendrites with ordered microstructures, which occur in synchronization with cycles of the oscillations [78–81]. In addition, the spatial period (size) of the ordered microstructures could be tuned by changing the oscillation amplitude and/or period, through variation in the current density or the concentration of the electroactive species [82]. These results led later to the elaboration of a general mechanism for such synchronization, causing the formation of ordered two- and three-dimensional microstructures [83].

As an introduction to such considerations it is useful to realize a more general, typical assumption that the morphology of crystals strongly depends on the “thermodynamic distance” between the actual conditions of crystallization and the thermodynamic equilibrium [84, 85]. Schematically this dependence is shown in Fig. 2.56 which also indicates that the dendrites are formed at extremely nonequilibrium conditions, and the growth of such patterns occurs via diffusion-limited aggregation (DLA) or dense branching morphologies (DBM). This sequence is explained by the fact that with increasing driving force for crystallization, the growing fronts of crystals with flat surfaces become destabilized due to an increasing contribution of mass and heat diffusion; the increasing surface instability leads then to formation of dendrites [83].

Experimental conditions of formation of such patterns involved both potentiostatic and galvanostatic conditions. For the *potentiostatic* mode of operation, representative examples of experimentally obtained three different types of deposits are shown in Fig. 2.57 (where OM stands for optical digital microscopy and SEM—for a high-resolution scanning electron microscope as the methods of obtaining the

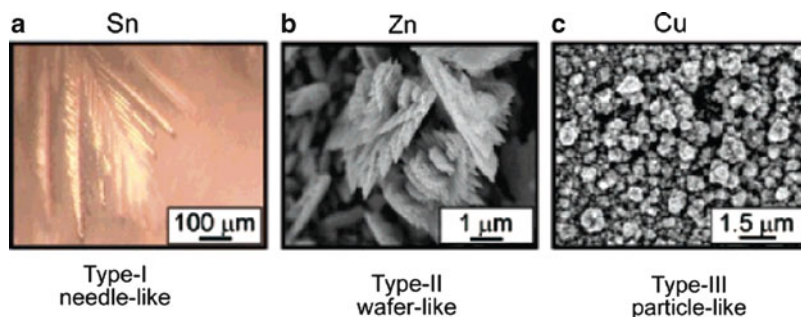


**Fig. 2.57** Dendrites of (a) tin (Sn), (b) zinc (Zn), and (c) copper (Cu), formed in the electrodeposition under the diffusion-limited conditions, where (a) is an OM image and (b) and (c) are SEM images. The electrolyte: (a) 0.2 M Sn(II) + 4.0 M NaOH, (b) 0.2 M Zn(II) + 4.0 M NaOH, and (c) 0.6 M CuSO<sub>4</sub> + 3.0 M lactic acid + a small amount of NaOH to adjust the pH to 9.0. The applied potential: (a)  $-1.7$  V, (b)  $-1.9$  V, and (c)  $-1.5$  V vs. Ag–AgCl. Reprinted with permission from [83] Copyright 2007 American Chemical Society

images). Type I (needle-like) pattern can be qualified as one-dimensional patterns, type II (wafer-like) as two-dimensional patterns, and type III (round-particle like) as three-dimensional patterns (note the different in the characteristic sizes).

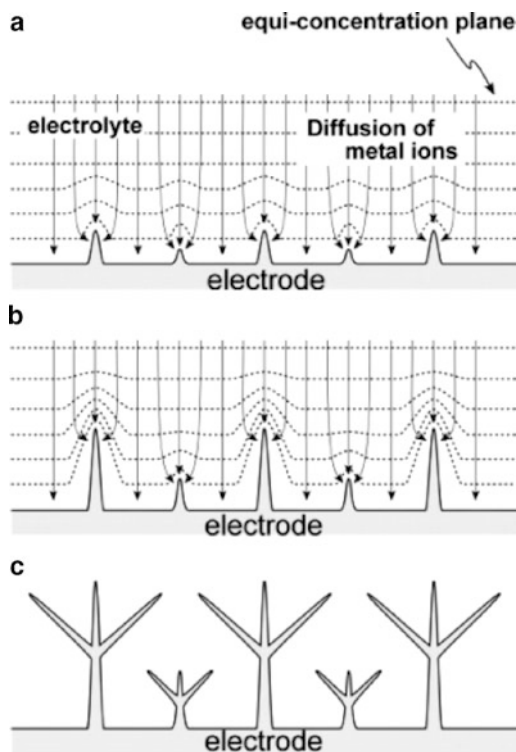
In the explanation of the growth of such patterns under diffusion-limited conditions, one should realize its *autocatalytic nature*, caused by the faster spherical diffusion of ions near the peaked parts of the substrate, caused in turn by steeper concentration gradient, compared to flat regions of the electrode (Fig. 2.58). As a consequence, peak parts grow autocatalytically more and more, which effect means, in other words, the destabilization of the flat surface.

In turn, under *galvanostatic* conditions, formation of dendritic patterns can occur also if the imposed current exceeds the diffusion-limited value and is often accompanied with the oscillations of the electrode potential. Furthermore, patterns occurring in this oscillatory regime often exhibit periodic spatial structure, indicating some kind of synchronization with those oscillations. Then one stage of the lattice is produced by one cycle of the oscillation. Figure 2.59 shows representative examples of such correlation between the galvanostatic oscillations of the electrode potential and simultaneous formation of patterns on the electrode surface [83].

These results suggest the existence of essentially common mechanism of synchronization for various metals, which was further studied using also in situ phase-contrast optical microscopic (POM) measurements of the electrode–electrolyte interface and electron backscattering diffraction (EBSD) analysis of the deposit structure. The essential construction of the proposed mechanism is briefly described below, taking Sn deposition as the process considered in detail.

The autocatalytic needle growth was observed to occur at the diffusion-limited conditions. Due to this pattern growth, the effective electrode area (roughness)

**Fig. 2.58** Schematic illustration of autocatalytic crystal growth producing dendrites under diffusion-limited conditions. (a) Spherical diffusion layers for deposited metal ions are formed near the peaked parts on the substrate, where the concentration gradient is thus steeper than in the electrolyte near flat parts; (b) in consequence, much faster diffusion of the metal ions to the peaked parts results in much faster (autocatalytic) growth of those parts; (c) the sharp crystal growth, causing roughening of the initial substrate surface, is accompanied with bifurcations in crystallographically equivalent directions, which leads to the formation of dendrites. Reprinted with permission from [83] Copyright 2007 American Chemical Society



increases, and therefore the electrode potential shifts to more positive values, in order to maintain the imposed fixed (total) current. This positive potential shift continues until the conditions become no longer diffusion controlled. Then the autocatalytic growth of needles is stopped and, instead of needles, the Sn cuboid crystals are formed, surrounded with the thermodynamically stable (100) and (010) faces. The reader interested in further details of this mechanism is advised to consult [83].

The explanation of the mechanism underlying the return of the electrode potential back to negative values is the following. Based on inspection of video movies showing the growth of Sn latticework and numerical simulations, involving finite difference model, it was suggested that the negative potential shift is caused by the exhaustion of Sn(II) ions in the electrolyte, near (or a little inside) the tip of the latticework. This should cause the decrease of the current inside the latticework, the effect equivalent to the decrease in the effective surface area which causes the negative potential shift, in order to maintain the fixed current. The extension of the above discussion on other types of deposits the reader can find in an original reference [83]. One should emphasize that the understanding of the mechanism of

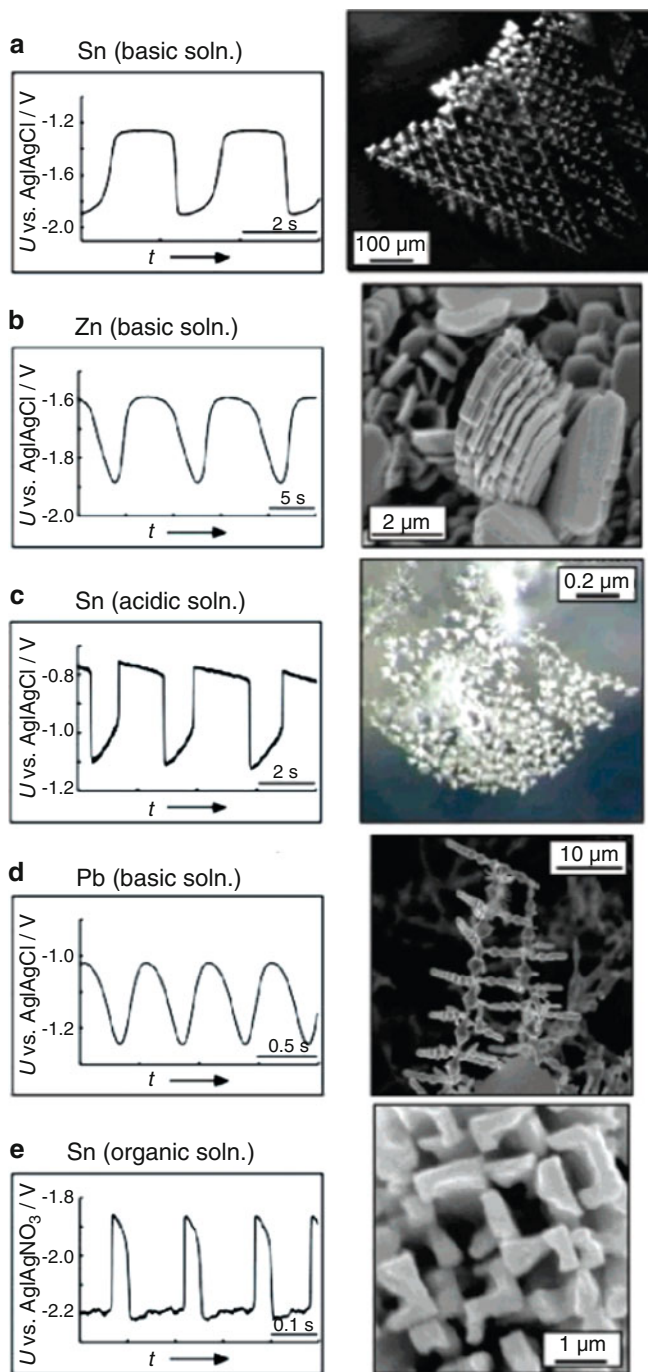


**Fig. 2.59** Examples of (*left*) potential oscillations under the constant-current conditions and (*right*) dendrites formed during the oscillations. The electrolyte and the applied current density:

formation of such deposits and the control of their shape and characteristic size should have important potential applications in the materials science for the preparation of designed and controlled micro- and nanostructures at solid surfaces.

Similar studies of pattern formation were conducted also for other metals (including their alloys). Nakanishi et al. [86] have studied the layer-by-layer electrodeposition of copper at a polycrystalline Au electrode, in the presence of *o*-phenanthroline (*o*-phen). This system exhibits the NDR region caused by the adsorption of the reduced form of  $[\text{Cu(II)}(\text{o-phen})_2]^{2+}$  complex,  $[\text{Cu(I)}(\text{o-phen})_2]^+$ , which suppresses the Cu electrodeposition. Under such conditions the electrodeposition exhibits both potential and current oscillations, suggesting that the system can be classified as the hidden NDR (HN-NDR) oscillator. Simultaneously with these oscillations, the color and surface morphology of Cu deposits varied synchronically. Microscopic investigations allowed to correlate the morphology of deposits with the stage of the oscillation cycle: in the positive side of the potential oscillations (high-current state of the current oscillation) the dense round Cu leaflets, which look gray, grow, while in the opposite-side stages of the oscillations, thin Cu leaflets form, which sequence of events produces a layered Cu deposit with the layer thickness of ca. 5  $\mu\text{m}$ . One should note that a way in which the NDR region is partly hidden is very specific: due to growth of thin Cu leaflets there increases the effective electrode area and this causes a current increase that masks the NDR. Since this mechanism of hiding the NDR is different from the previously proposed ones (see Sect. 3.4, volume I), the authors consider the system studied as the *new type* of the HN-NDR oscillator. In others words, the former classification of oscillators, which assumed implicitly that the electrode surface is geometrically uniform, is now extended for the systems in which the effective electrode surface area, considered a key variable, increases. A detailed description of processes composing this mechanism is given in [86].

As another example of the dendritic growth one can invoke deposition of metallic lithium in symmetrical lithium/polymer/lithium cells, as Chazalviel et al. have reported [87]. In this case, however, the formation of dendrites is a highly undesirable phenomenon, since it affects the charge efficiency of the lithium anode. Thus, the understanding of this process, attributed to the existence and/or formation of local inhomogeneities on the electrode surface, served here as a way to determine the conditions, under which the dendrites are *not* formed. In more recent work, Chazalviel et al. [88] have presented the experimental and theoretical study of the onset of the growth of copper deposit from  $\text{CuSO}_4$  solution. It was found that, in order to avoid (as above) irregularity in the deposit morphology (e.g., formation of the dendrites), the vertical, thin-layer cell, with the

---

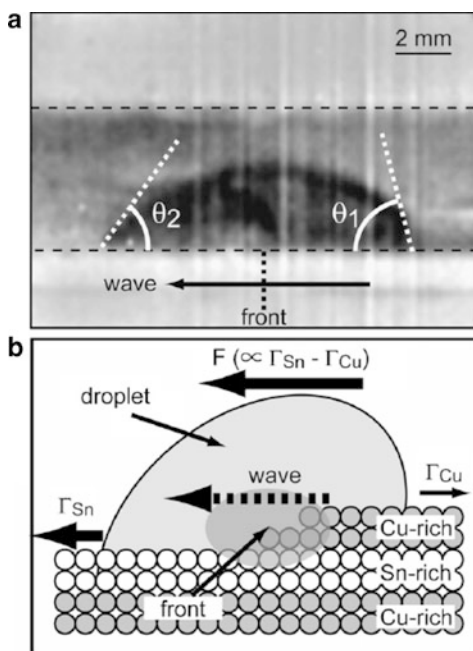
**Fig. 2.59** (continued) (a) 0.2 M  $\text{Sn(II)}$  + 4.0 M  $\text{NaOH}$ ,  $-36 \text{ mA cm}^{-2}$ ; (b) 0.2 M  $\text{Zn(II)}$  + 4.0 M  $\text{NaOH}$ ,  $-21 \text{ mA cm}^{-2}$ ; (c) 0.3 M  $\text{SnSO}_4$  + 0.3 M  $\text{H}_2\text{SO}_4$  + 1.0 g  $\text{L}^{-1}$  gelatin, scan rate  $1.67 \text{ mA s}^{-1}$ ; (d) 0.15 M  $\text{PbSO}_4$  + 4.0 M  $\text{NaOH}$ ,  $-14 \text{ mA cm}^{-2}$ ; (e) 0.1 M  $\text{SnCl}_2$  + 0.1 M  $\text{NaClO}_4$ ,  $-7.2 \text{ mA cm}^{-2}$ . The solvent for the electrolytes was water, except that dimethylformamide is used in (e). Reprinted with permission from [83] Copyright 2007 American Chemical Society

cathode on top, should be used, since in this configuration the stability of the electrochemical system is enhanced. However, when the imposed current was increasing, close to the limiting current density, the cell voltage exhibited oscillatory variations of rather unclear origin. In his theoretical work, Chazalviel [89] has shown earlier that the growth of ramified metallic deposits by electrodeposition from dilute salt solutions and in a high electric field is a direct consequence of the creation, under such conditions, of a space charge upon anion depletion in the vicinity of the cathode. The front of the ramified deposit was predicted to advance at a speed just equal to the velocity of the anions in the applied electric field:  $v_a = -\mu_a E_0$ , meaning the product of the ionic mobility and the electric field intensity, respectively. Of course, such dilute electrolyte solutions are not often encountered in electrochemical practice [for examples related to nonlinear dynamics, cf. Sects. 4.1 (volume I), 2.10, and 5.9.4].

Concerning further the alloys, Nakanishi et al. [90] have studied the electrodeposition from an acidic solution containing  $\text{Cu}^{2+}$ ,  $\text{Sn}^{2+}$ , and a cationic surfactant. The  $I$ - $E$  characteristic of such system exhibited negative differential resistance, caused by the potential-dependent adsorption of the surfactant (acting as an inhibitor for diffusion of metal ions) on the alloy surface. Based on scanning Auger microscopic measurements it was found that alloy films deposited during the oscillations had an alternate multilayer structure composed of two alloy layers of different compositions. The multilayer had the period of thickness of 40–90 nm and was uniform over an area of ca.  $1 \times 1$  mm. In another work, the formation of nano-scale layered structures in induced co-deposition of unique, widely used in industries, Ni–P, Ni–W, and Co–W alloys was investigated using an in situ electrochemical quartz crystal microbalance technique [91]. Also in this case the negative differential resistance and its crucial role in the onset of oscillations, and in consequence in the layer-structure formation, were found. Strictly speaking, the NDR region could overlap with the hydrogen evolution current and then the oscillator could be qualified as the hidden (HN-NDR) one. In this case, the important role is played by such electrolyte components as  $\text{H}_2\text{PO}_2^-$  and  $\text{WO}_4^{2-}$  which adsorb on the electrode and act as a promoter for the co-deposition reaction; also the NDR arises from desorption of adsorbed promoter, when the potential moves into negative direction. In the opinion of the authors, the detailed scheme of processes elaborated by them constitutes the general mechanism for the induced co-deposition of some iron-group alloys. Furthermore, understanding of such processes should allow to control the chemical composition, the size of the layered structures, and various properties of the alloys for high performances in industrial applications [91].

Recently, Ihara et al. [92] have described a large interfacial energy gradient produced at a front of electrochemical wave appearing during the CuSn alloy oscillatory electrodeposition from an aqueous solution. This was observed as the directional lateral motion of an oil (nitrobenzene) droplet put on an electrode surface. During the oscillation, the surface composition of the electrodeposit changed periodically between Cu- and Sn-rich alloys, and the transition between these phases initiated the propagation of the electrochemical wave over the entire

**Fig. 2.60** (a) Picture taken at the moment when the wave just reaches to the right edge of the droplet. (b) Schematic illustration of the mechanism of the droplet motion. Reprinted from [92], Copyright 2009, with permission from Elsevier



electrode surface. The fact that the force produced is able to transport such macroscopic object, like the oil droplet, proves the existence of extremely large imbalance of the interfacial energy (interfacial tension)—see Fig. 2.60. In this way, the reaction–diffusion (migration) system exhibits coupling with convection.

### 2.11.2 Dendritic Deposition on Liquid/Liquid Interface

In recent studies, the traditional solid/liquid interface was replaced by liquid/liquid interface. For example, Efrima et al. [93–96] have studied the patterns of silver electrodeposited at the water–air and water–organic liquid interfaces, under both dc and ac conditions, showing e.g., the formation of fractal “metal leaves” (Fig. 2.61) [93]. In turn, Fig. 2.62 shows reported shapes of Ag deposit at the water/air interface [96].

The morphology of patterns was discussed in terms of the Wagner number which in its original form is defined as  $W = R_f/R_s$  [97], where  $R_f$  is the faradaic (charge-transfer) resistance of the electrode process and  $R_s$  is the ohmic resistance of the solution across a characteristic distance in the electrochemical cell. The small Wagner number means that the morphology of the deposit is controlled by the ohmic resistance of the solution, and then the instabilities set in, causing that the deposits tend to be ramified. In contrast, when the Wagner number is large, the

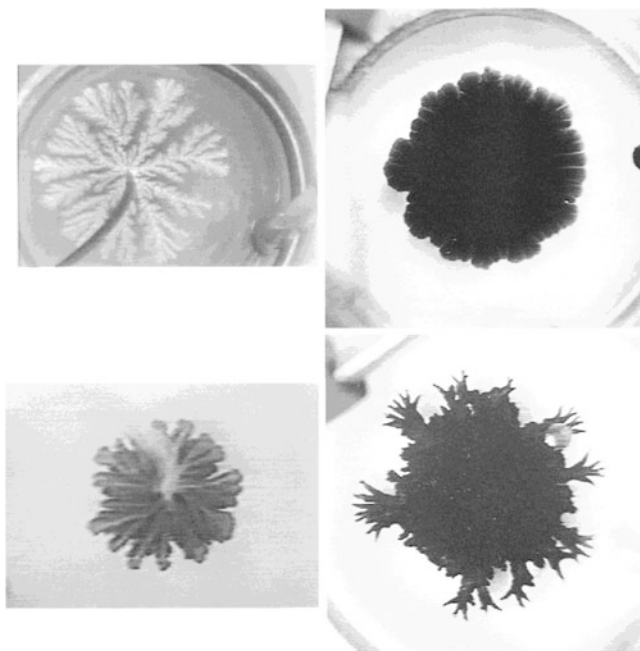


**Fig. 2.61** Typical deposits at 5 V for different solvents with a water phase containing ammoniacal 0.05 M  $\text{AgNO}_3$ , 0.1% anisic acid, and 0.03% FC143 surfactant, for (a, top left) air, (b, bottom left) carbon tetrachloride, (c, top right) dichloromethane, and (d, bottom right) bromobenzene. Reprinted with permission from [93]. Copyright 1996 American Chemical Society

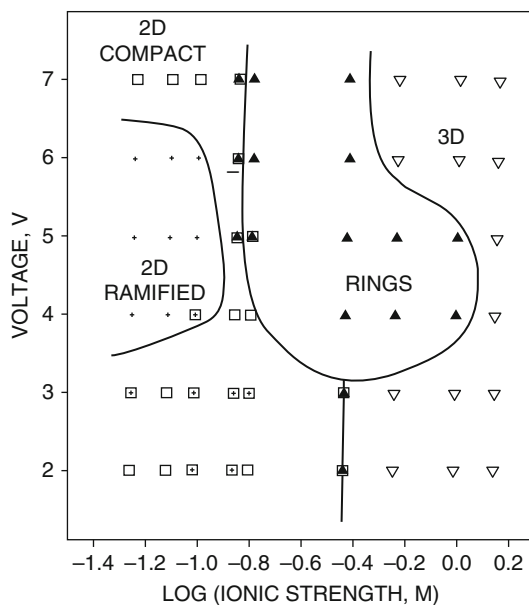
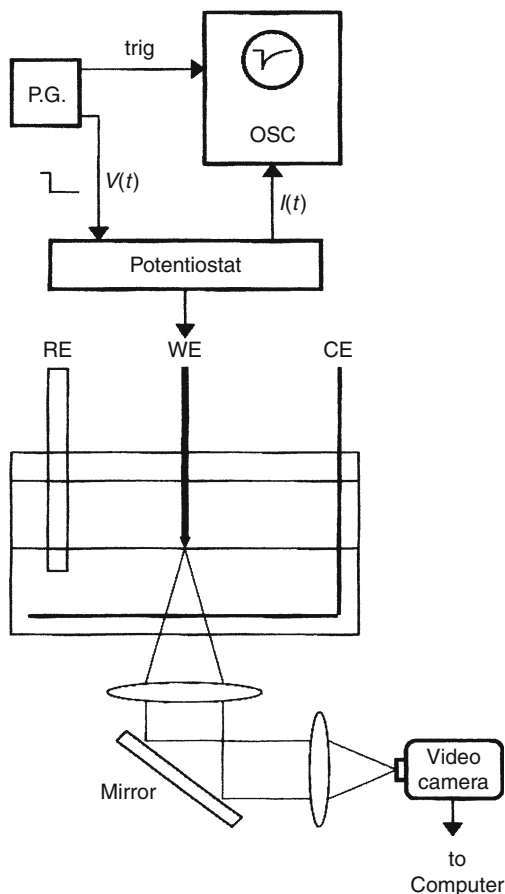


**Fig. 2.62** Shape diagram for silver electrodeposition at the water/air surface. The silver ion concentration is 0.05 M. Reprinted with permission from [96]. Copyright 1997 American Chemical Society

**Fig. 2.63** Schematic representation of the experimental setup for the electrochemical and the magneto-electrochemical measurements. PG and OSC represent pulse generator and oscilloscope, respectively. Reprinted from [99], Copyright 1999, with permission from Elsevier



electron-transfer step at the interface controls the current distribution and then the deposit turns out to be compact [96]. For the description of the morphology of such patterns, Efrima has derived a generalized Wagner number, which indicates whether the pattern will be a compact deposit or whether it will be irregular, ramified, and dendritic (for details, see the original reference [98]).

As a continuation of these works, Nakabayashi et al. [99] have studied the patterns of zinc electrodeposited at the interface between two practically immiscible liquids: 4-methyl-2-pentanone and aqueous electrolyte solution (for the oscillators based on the characteristics of such interfaces, cf. Chap. 6). The aim of these studies was to explain the details of the anisotropic growth of the metal phase, by investigating the effect of the electrode potential and of the magnetic field, causing magnetohydrodynamic effects. The experimental setup that allowed the studies for both the air-liquid and the liquid-liquid interfaces is shown in Fig. 2.63. In particular, the time course of the shape change of the metal deposit was observed through the magnification optics focused on the top of the working

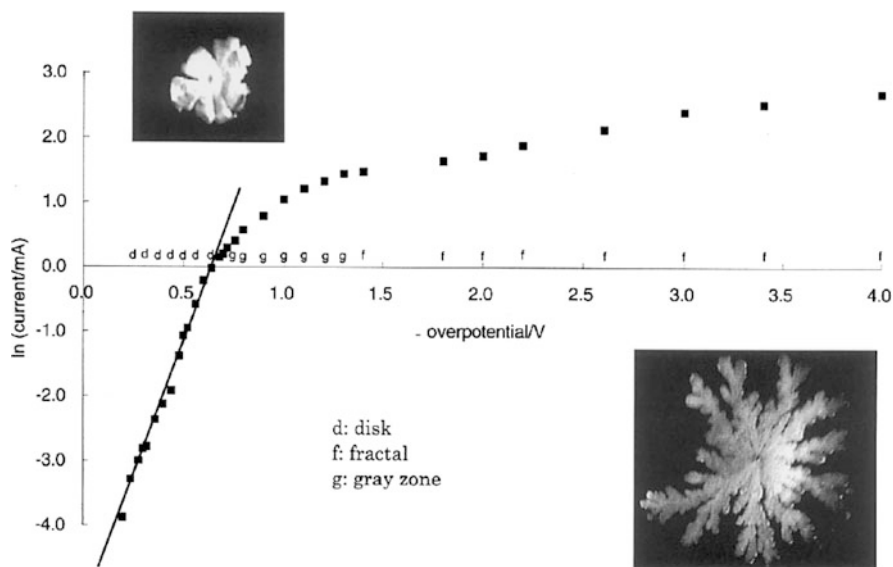


**Fig. 2.64** Logarithm of the sampling current as a function of the final potential. “d,” “f,” and “g” above the potential axis represent the pattern of the deposit and the pictures at the upper and lower right are typical shapes of the deposit, disk (d) and fractal (f), respectively. Reprinted from [99], Copyright 1999, with permission from Elsevier

electrode from the bottom of the cell, and recorded with the video camera. As the working electrode (cathode) the carbon rod with a diameter of 0.5 mm was used, sharpened to ca. 0.1 mm in diameter at the top. The counter electrode was a ring of zinc wire dipped in the aqueous phase and as a reference electrode, the conventional SCE was used. The aqueous solution contained 2 M zinc sulfate and this was the lower phase in the experiments with the liquid/liquid interface (the upper phase being then 4-methyl-2-pentanone).

In the series of experiments performed for the liquid–liquid interface, the potential was stepped from  $-1.2$  V (where the deposition of zinc began) to more negative values. In Fig. 2.64, the logarithm of current was plotted as a function of the final potential of the step, expressed versus the initial  $-1.2$  V (the current flowing through the first 5 ms was neglected, in order to eliminate the capacitive current). This plot indicates simultaneously the shape of the zinc deposits, varying from the disk, through gray zone, up to fractal dendrites at sufficiently negative potentials. Since the disk shape occurred for the logarithmic dependence of the current on the potential (Butler–Volmer kinetics), one can conclude that this shape corresponds to the conditions, under which the rate of zinc deposition is controlled by the rate of the electron-transfer step. In turn, since fractal shapes were formed under more negative potentials, they were associated with the process of zinc deposition controlled by the rate of mass ( $\text{Zn}^{2+}$  ions) transport, in concordance with the assumption underlying the applicability of the DLA formalism.

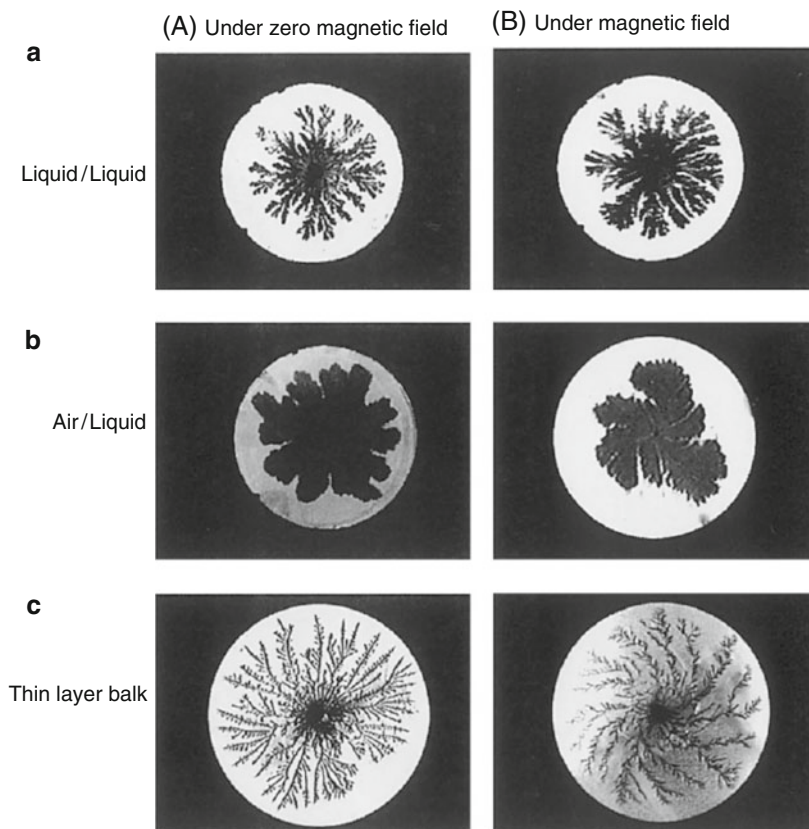


**Fig. 2.65** Typical two-dimensional fractal deposit at (a) the 4-methyl-2-pentanone–aqueous electrolyte interface, (b) the air–aqueous electrolyte interface and in (c) the thin layer electrolyte. The magnetic field strengths are 1,200, 80, and 320 G for (a)–(c), respectively. Reprinted from [99], Copyright 1999, with permission from Elsevier

Placing the electrochemical cell in the magnetic field affects the motion of the electrolyte. Such magnetohydrodynamic effects were studied after the placing of the electrochemical cell just above the bore of the helium-free superconducting magnet; in this configuration, the direction of magnetic field was vertical and upward. In some experiments, oriented on the formation of quasi-two-dimensional deposits, the reaction proceeded in a thin (0.5 mm) 0.05 M zinc sulfate solution layer, placed between two plastic plates. In the presence of magnetic field, the Lorenz force acts on the ions towards the tangential direction, causing the spiral distortion of the deposited zinc patterns. Figure 2.65 shows such effects for different experimental conditions, but in each case for the electrode potential so negative that the deposition is controlled by the rate of mass transfer.

A bit surprising is the fact that of all interfaces studied, the liquid–liquid one was most resistant to the effect of the magnetic field (the morphology of the zinc pattern

remained practically intact up to the field of 1,200 G, but above this value the whole pattern was destroyed by rotational flow).

The liquid–liquid interface as the localization of electrodeposition of metal films was a subject of also more recent studies by Nakanishi et al. [100]. In this work there was studied the electrodeposition of zinc at an aqueous  $\text{ZnSO}_4$ –*n*-butylacetate (BuAc) interface, under conditions when potential oscillations were observed in the region of the current density exceeding the diffusion-limited value (first reported by Tada et al. [101]). In situ optical microscopic observations showed that the formation of two-dimensional Zn film with a concentric pattern at the liquid–liquid interface was accompanied with the synchronic meniscus oscillation of this interface. Furthermore, the vigorous growth of the deposits occurred only when the shape of the meniscus became hollow on the negative potential side of the potential oscillation, while on the positive side, the meniscus became almost flat and the deposits formed in the preceding stage were thickened. The mechanism of those phenomena invoked the fact that the interfacial tension at the growing metal/aqueous solution interface was extremely large. In brief, the electrochemical oscillations were found to occur due to the cooperation of various processes: autocatalytic electrodeposition under diffusion-controlled conditions, increase and decrease of the electrode/aqueous phase interfacial tension and meniscus oscillation. For description of analogous interface dynamics, see also Sect. 6.1.

In turn, the oscillatory gold electrodeposition, occurring in the form of thin film formed at a liquid/air interface was described first by Saliba et al. [102]. It was further studied by Fukami et al. [103], using the Raman scattering spectroscopy (SERS) under in situ conditions. This technique allowed to monitor the dynamic nanostructural changes of the deposit. This system exhibited only potential oscillations under galvanostatic conditions. It was found that the oscillations occurred when the applied current exceeded the diffusion-limited current for Au electrodeposition, with this process being charge-transfer limited when the potential corresponded to the positive side of the oscillation (then the dendritic growth of crystals occurs) and switching to the control by diffusion, when the potential moved to negative values in the oscillatory peak (then the thickening of dendritic crystals occurs). The mechanism of oscillations involves, starting from the diffusion-limited conditions, the autocatalytic character of electrodeposition, caused by enhanced diffusion of  $\text{AuCl}_4^-$  ions to the circular or spherical diffusion layer formed at the interface and resulting in the growth of dendritic needle-like crystals. This leads to a large increase in the effective surface area of the Au film and thus to a large decrease in the effective current density, causing a positive shift in the electrode potential, until the diffusion-controlled conditions switch into the control by the charge-transfer rate at the interface. Then the needle growth stops and the electrodeposition proceeds steadily. The needles are thickened and coalesced with each other, resulting in a rather continuous film. The corresponding decrease in the effective electrode surface area causes a back increase of the effective current density, until the electrode potential shifts to so negative values that the maintaining of the externally imposed current requires the contribution from the evolution of

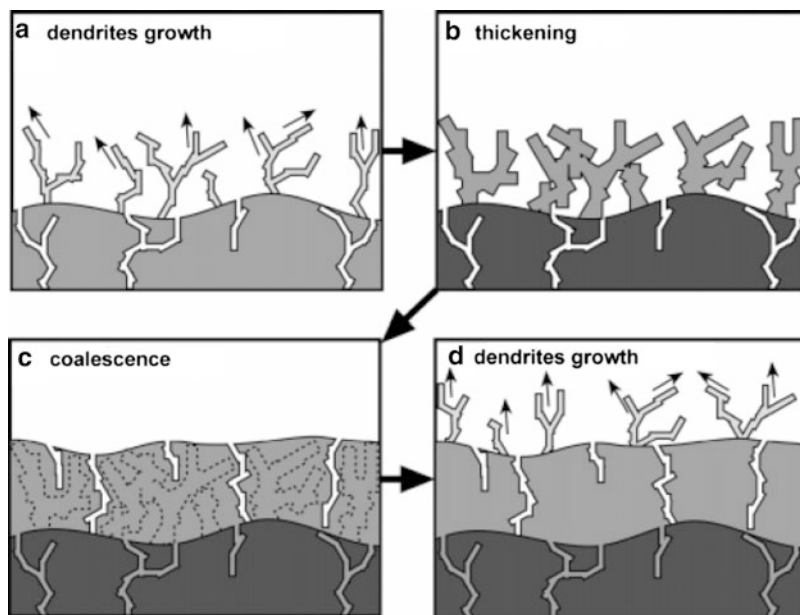


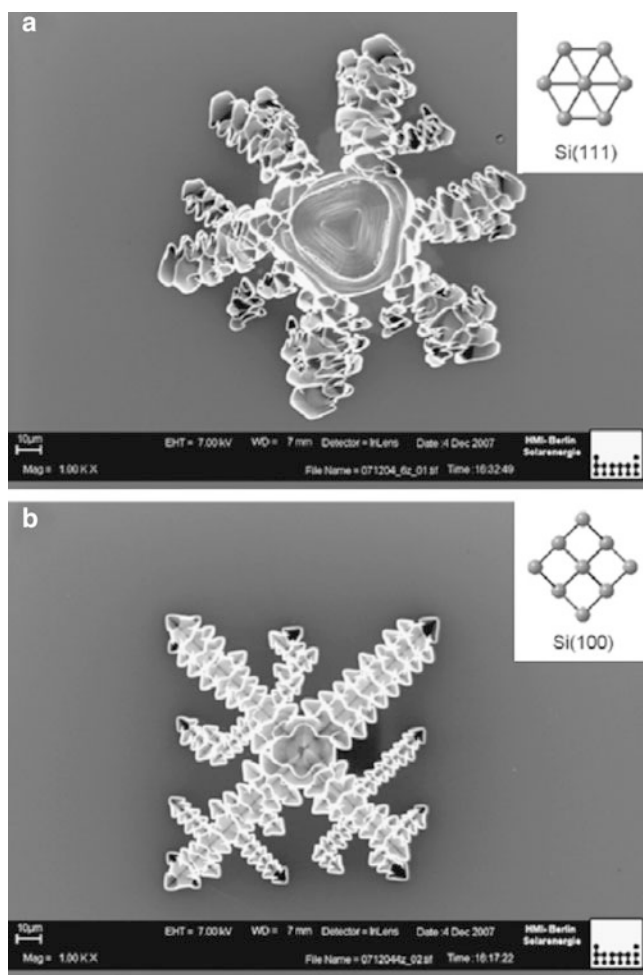
**Fig. 2.66** Schematic drawings for explaining the mechanism for the oscillatory growth of the Au film and associated oscillations of the electrode potential under galvanostatic conditions. (a) Very fast, diffusion-limited electrodeposition of Au at the negative end of the potential oscillation leads to autocatalytic growth of the dendrites. The associated growth of effective surface area, causing the decrease in effective current density  $|j_{\text{eff}}|$ , results in continuous positive shift in the electrode potential; (b,c) At the attained high-potential state, when the electron transfer-limited condition is attained, the dendritic needles stop to grow and, instead, they are thickened (b) and coalesced (c) with each other, resulting in a rather continuous film; (d) Due to decrease in effective surface area, the effective current density  $|j_{\text{eff}}|$  increases and when exceeds the diffusion-limited current density of  $\text{AuCl}_4^-$  electroreduction, the electrode potential suddenly shifts to negative direction in order to maintain the externally controlled current by addition of hydrogen evolution current; in this way, the low-potential state, characterized with the growth of dendrites, is reached again, Reprinted with permission from [103] Copyright 2007 American Chemical Society

hydrogen. The sequence of these steps of the oscillations is schematically shown in Fig. 2.66.

Other examples of dendritic morphology of deposited metals, associated with the oscillations driven by convective motion, are described in Sect. 5.8.3.

## 2.12 Dendritic Patterns in Silicon Electrodeposition

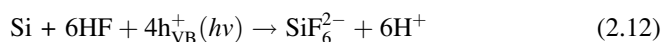
Fractal patterns are not specific for metallic deposits only. Recently, Lublow and Lewerenz [104] have described the fractal etch structures formed on *n*-type Si photoelectrodes under anodic polarization in concentrated ammonium fluoride



**Fig. 2.67** HR-SEM images of structures obtained on (a) Si(111) and (b) Si(100) after dissolution in 40%  $\text{NH}_4\text{F}$  for 10 min using a light intensity of about  $7 \text{ mW cm}^{-2}$ . The insets indicate the surface lattice and the relative orientation of the structures to the lattice. Reprinted from [104], Copyright 2009, with permission from Elsevier

solutions. However, in this case the propagating branches of these structures generally reflect the surface lattice geometry of the substrates on a micrometer scale while inner topographies are characterized by ensembles of slow-etching planes. Figure 2.67 shows the images of exemplary patterns formed on Si(111) and Si(100) surfaces.

In the mechanism of formation of these patterns, not only the dissolution of illuminated  $n$ -Si:



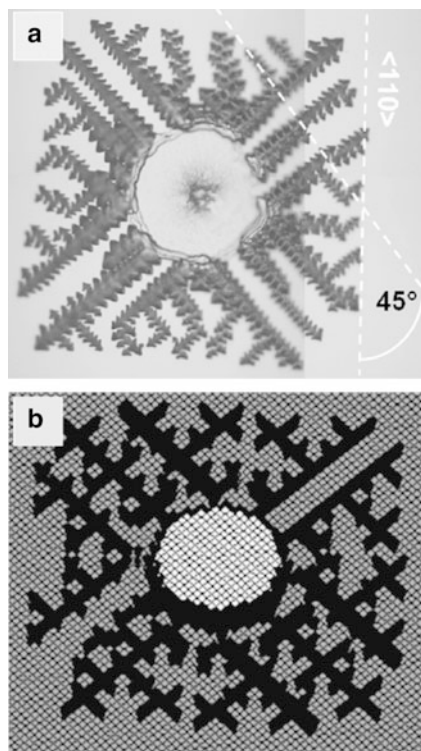


**Fig. 2.68** Comparison of an experimental structure obtained in 40%  $\text{NH}_4\text{F}$  after 10 min at  $U = 6 \text{ V}$  (light intensity  $7 \text{ mW cm}^{-2}$ ) with a simulated structure. (a) The orientation of the fractal structure with respect to the surface lattice is indicated by an angle which refers to the primary flat of the wafer. (b) Simulated structure assuming uniform propagation of the branches which extend from initially cracked sites located at the boundary of an adsorbed oxygen bubble (see [104]). Reprinted from [104], Copyright 2009, with permission from Elsevier

comprising first electrochemical formation of  $\text{SiO}_2$ , followed by its pH-dependent dissolution by  $\text{HF}$  and  $\text{HF}_2^-$  to  $\text{SiF}_6^{2-}$ , was taken into account. Also, the parallel oxygen evolution reaction (OER):



was assumed to play an important role for the topographical structure formation. Oxygen gas bubbles are rapidly forming in the initial phase of the photoelectrochemical decomposition process and they are adsorbed to surface sites which coincide with the centers of fractal structures. In order to model such phenomena, simplified simulation procedures were derived from quantitative in-plane stress analysis. Comparison of experimental and simulated patterns is shown in Figs. 2.68 and 2.69. Other types of spatial patterns emerging during etching of semiconductors are described in Chap. 4.

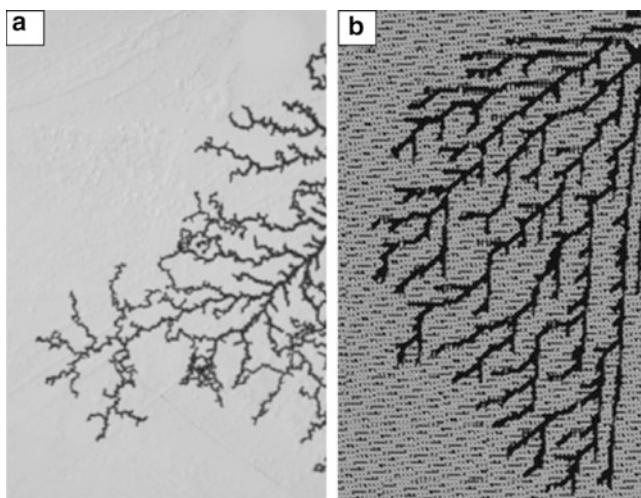


**Fig. 2.69** Comparison of an experimental and simulated structure for the case of lower light intensity (below  $1 \text{ mW cm}^{-2}$ ). According to model considerations, the lateral propagation velocities of the branches are varying with time and resulting thus in less regular structures. Reprinted from [104], Copyright 2009, with permission from Elsevier

## References

1. Flätgen G, Krischer K, Pettinger P, Doblhofer K, Junkes H, Ertl G (1995) Two-dimensional imaging of potential waves in electrochemical systems by surface plasmon microscopy. *Science* 269:668–671
2. Bonhoeffer KF (1948) Activation of passive iron as a model for the excitation of nerve. *J Gen Physiol* 32:69–91
3. Heatcote HL (1902) *Z physik Chem* 37:368
4. Heatcote HL (1907) *J Chem Soc Ind* 26:899
5. Lillie RS (1918) *Science* 48:51
6. Lillie RS (1930) *J Gen Physiol* 14:344
7. Lillie RS (1936) *Biol Rev Camb Philos Soc* 16:216
8. Murray JD (2002) *Mathematical biology. I. An introduction*, 3rd edn. Springer, New York, NY
9. Murray JD (2003) *Mathematical biology. II. Spatial models and biomedical applications*, 3rd edn. Springer, New York, NY
10. Franck UF (1989) Periodische Strukturen und Vorgänge in gleichgewichtsfernen physikalisch-chemischen Systemen. *Nova Acta Leopoldina NF* 60:109–131
11. Nakabayashi S, Baba R (1998) Spatiotemporal propagation of a non-linear electrochemical reaction over an iron electrode. *Chem Phys Lett* 287:632–638
12. Baba R, Shiomi Y, Nakabayashi S (2000) Spatiotemporal reaction propagation of electrochemically controlled non-linear iron current oscillator. *Chem Eng Sci* 55:217–222
13. Agladze K, Steinbock O (2000) Waves and vortices of rust on the surface of corroding steel. *J Phys Chem A* 104:9816–9819
14. Agladze K, Thouvenel-Romans S, Steinbock O (2001) Electrochemical waves on patterned surfaces: propagation through narrow gaps and channels. *J Phys Chem A* 105:7356–7363
15. Hudson JL, Tabora J, Krischer K, Kevrekidis IG (1993) Spatiotemporal period doubling during the electrodisolution of iron. *Phys Lett A* 179:355–363

16. Koper MTM, Sluyters JH (1993) A simplified approach to the modeling of wave propagation at electrode/electrolyte interfaces. *Electrochim Acta* 38:1535–1544
17. Kristev I, Nikolova M, Nakada I (1989) Spiral structures in electrodeposited silver-antimony alloys. *Electrochim Acta* 34:1219–1223
18. Gladyshev VP, Kovaleva SV (1997) Autooscillatory processes and surface periodic patterns, emerging at anodic oxidation of amalgams of alkaline metals. *Zh Obshch Khim* 67:1743, in Russian
19. Krischer K (2001) Spontaneous formation of spatiotemporal patterns at the electrode–electrolyte interface. *J Electroanal Chem* 501:1–21
20. Krischer K (1999) Principles of temporal and spatial pattern formation in electrochemical systems. In: Conway BE, Bockris JO'M, White R (eds) *Modern aspects of electrochemistry*. Plenum, New York, NY
21. Krischer K (2003) Nonlinear dynamics in electrochemical systems. In: Alkire RC, Kolb DM (eds) *Advances in electrochemical science and engineering*. Wiley-VCH, Weinheim
22. Flätgen G, Krischer K (1995) Accelerating fronts in an electrochemical system due to global coupling. *Phys Rev E* 51:3997–4004
23. Flätgen G, Krischer K, Ertl G (1996) Spatio-temporal pattern formation during the reduction of peroxodisulfate in the bistable and oscillatory regime: a surface plasmon microscopy study. *J Electroanal Chem* 409:183–194
24. Grauel P, Christoph J, Flätgen G, Krischer K (1998) Stationary potential patterns during the reduction of peroxodisulfate at Ag ring electrodes. *J Phys Chem B* 102:10264–10271
25. Otterstedt R, Plath PJ, Jaeger NI, Sayer JC, Hudson JL (1996) Accelerating fronts during the electrodisolution of cobalt. *Chem Eng Sci* 51:1747–1756
26. Otterstedt R, Plath PJ, Jaeger NI, Hudson JL (1996) Modulated electrochemical waves. *Phys Rev E* 54:3744–3751
27. Otterstedt RD, Plath PJ, Jaeger NI, Hudson JL (1996) Rotating waves on disk and ring electrodes. *J Chem Soc Faraday Trans* 92:2933–2939
28. Lev O, Sheintuch M, Pismen LM, Yarnitzky Ch (1988) Standing and propagating wave oscillations in the anodic dissolution of nickel. *Nature* 336:458–459
29. Lev O, Sheintuch M, Yarnitsky H, Pismen LM (1990) Spatial current distribution during nickel anodic dissolution in sulfuric acid. *Chem Eng Sci* 45:839–847
30. Haim D, Lev O, Pismen LM, Sheintuch M (1992) Modelling spatiotemporal patterns in anodic nickel dissolution. *Chem Eng Sci* 47:3907–3913
31. Bîrzu A, Green BJ, Otterstedt RD, Jaeger NI, Hudson JL (2000) Modeling of spatiotemporal patterns during metal electrodisolution in a cell with a point reference electrode. *Phys Chem Chem Phys* 2:2715–2724
32. Bîrzu A, Green BJ, Jaeger NI, Hudson JL (2001) Spatiotemporal patterns during electrodisolution of a metal ring: three-dimensional simulations. *J Electroanal Chem* 504:126–136
33. Jaeger NI, Otterstedt RD, Bîrzu A, Green BJ, Hudson JL (2002) Evolution of spatiotemporal patterns during the electrodisolution of metals: experiments and simulations. *Chaos* 12:231–239
34. Bîrzu A, Plenge F, Jaeger NI, Hudson JL, Krischer K (2003) Excitable dynamics during electrodisolution of a metal disk electrode: model calculations. *Phys Chem Chem Phys* 5:3724–3731
35. Bîrzu A, Krischer K (2006) Two-dimensional electrochemical turbulence during the electrodisolution of metal disk electrodes: model calculations. *Phys Chem Chem Phys* 8:3659–3668
36. Holmes P, Lumley J, Berkooz G (1996) *Turbulence, coherent structures, dynamical systems and symmetry*. Cambridge University Press, Cambridge, MA
37. Grauel P, Krischer K (2001) Fronts and stationary domains during electrochemical H<sub>2</sub> oxidation on Pt: the impact of the position of the reference electrode on the spatiotemporal behavior. *Phys Chem Chem Phys* 3:2497–2502
38. Grauel P, Varela H, Krischer K (2001) Spatial bifurcations of fixed points and limit cycles during the electrochemical oxidation of H<sub>2</sub> on Pt ring-electrodes. *Faraday Discuss* 120:165–178

39. Varela H, Beta C, Bonnefont A, Krischer K (2005) A hierarchy of global coupling induced cluster patterns during the oscillatory  $\text{H}_2$ -electrooxidation reaction on a Pt ring-electrode. *Phys Chem Chem Phys* 7:2429–2439
40. Plenge F, Varela H, Krischer K (2005) Asymmetric target patterns in one-dimensional oscillatory media with genuine nonlocal coupling. *Phys Rev Lett* 94:198301-1–198301-4
41. Varela H, Beta C, Bonnefont A, Krischer K (2005) Transitions to electrochemical turbulence. *Phys Rev Lett* 94:174104-1–174104-4
42. Mikhailov AS (1994) *Foundation of synergetics I*. Springer, Berlin
43. Benjamin TB, Feir J (1967) The disintegration of wave trains on deep water. Part 1. Theory. *J Fluid Mech* 27:417–430
44. Shraiman BI, Pumir A, van Saarloos W, Hohenberg PC, Chaté H, Holen M (1992) Spatiotemporal chaos in the one-dimensional complex Ginzburg-Landau equation. *Physica D* 57:241–248
45. Krischer K, Varela H, Bîrzu A, Plenge F, Bonnefont A (2003) Stability of uniform electrode states in the presence of ohmic drop compensation. *Electrochim Acta* 49:103–115
46. Plenge F, Li YJ, Krischer K (2004) Spatial bifurcations in the generic N-NDR electrochemical oscillator with negative global coupling: theory and surface plasmon experiment. *J Phys Chem B* 108:14255–14264
47. Baba N, Krischer K (2008) Mixed-mode oscillations and cluster patterns in an electrochemical relaxation oscillator under galvanostatic control. *Chaos* 18:015103-1–015103-9
48. Bonnefont A, Morschl R, Bauer P, Krischer K (2009) Electrochemical impedance spectroscopy of patterned steady-states on electrode surfaces. *Electrochim Acta* 55:410–415
49. Koper MTM, Schmidt TJ, Marković RPN (2001) Potential oscillations and S-shaped polarization curve in the continuous electro-oxidation of CO on platinum single-crystal electrodes. *J Phys Chem B* 105:8381–8386
50. Morschl R, Bolten J, Bonnefont A, Krischer K (2008) Pattern formation during CO electrooxidation on thin Pt films studied with spatially resolved infrared absorption spectroscopy. *J Phys Chem C* 112:9548–9551
51. Christoph J, Strasser P, Eiswirth M, Ertl G (1999) Remote triggering of waves in an electrochemical system. *Science* 284:291–293 doi:[10.1126/science.284.5412.291](https://doi.org/10.1126/science.284.5412.291)
52. Christoph J, Otterstedt R, Eiswirth M, Jaeger NI, Hudson JL (1999) Negative coupling during oscillatory pattern formation on a ring electrode. *J Chem Phys* 110:8614–8621
53. Strasser P, Christoph J, Lin WF, Eiswirth M, Hudson JL (2000) Standing wave oscillations in an electrocatalytic reaction. *J Phys Chem A* 104:1854–1860
54. Christoph J, Eiswirth M (2002) Theory of electrochemical pattern formation. *Chaos* 12:215–230
55. Turing AM (1952) The chemical basis for morphogenesis. *Phil Trans R Soc London B* 327:37–72
56. Krömker S (1998) Wave bifurcation in models for heterogeneous catalysis. *Acta Math Univ Comenianae* 67:83–100
57. Zhabotinsky AM, Dolnik M, Epstein IR (1995) Pattern formation arising from wave instability in a simple reaction–diffusion system. *J Chem Phys* 103:10306–10314
58. Dolnik M, Zhabotinsky AM, Epstein IR (1996) Modulated standing waves in a short reaction–diffusion system. *J Phys Chem* 100:6604–6607
59. Lee J, Strasser P, Eiswirth M, Ertl G (2001) On the origin of oscillations in the electrocatalytic oxidation of HCOOH on a Pt electrode modified by Bi deposition. *Electrochim Acta* 47:501–508
60. Christoph J, Noh T-G, Lee J, Strasser P, Eiswirth M (2009) Spatiotemporal self-organization in the oscillatory HCOOH oxidation on a Pt ribbon electrode—theory and experiments. *Surf Sci* 603:1652–1661
61. Zhao Y, Wang S, Varela H, Gao Q, Hu X, Yang J, Epstein IR (2011) Spatiotemporal pattern formation in the oscillatory electro-oxidation of sulfide on a platinum disk. *J Phys Chem C* 115:12965–12971

62. Mazouz N, Krischer K (2000) A theoretical study on Turing patterns in electrochemical systems. *J Phys Chem B* 104:6081–6090
63. Li YJ, Oslonovitch J, Mazouz N, Plenge F, Krischer K, Ertl G (2001) Turing-type patterns on electrode surfaces. *Science* 291:2395–2398 doi:[10.1126/science.1057830](https://doi.org/10.1126/science.1057830)
64. Bonnefont A, Varela H, Krischer K (2003) Stationary small and large amplitude patterns during bulk CO electrooxidation on Pt. *Chem Phys Chem* 4:1260–1263
65. Bonnefont A, Varela H, Krischer K (2005) Stationary spatial patterns during bulk CO electrooxidation on Pt. *J Phys Chem B* 109:3408–3415
66. Strasser P, Eiswirth M, Ertl G (1997) Oscillatory instabilities during formic acid oxidation on Pt(100), Pt(110) and Pt(111) under potentiostatic control. II. Model calculations. *J Chem Phys* 107:991–1003
67. Ihle T, Müller-Krumbhaar H (1994) Fractal and compact growth morphologies in phase transitions with diffusion transport. *Phys Rev E* 49:2972–2991
68. Arneodo A, Argoul F, Couder Y, Rabaud M (1991) Anisotropic Laplacian growths: from diffusion-limited aggregates to dendritic fractals. *Phys Rev Lett* 66:2332–2335
69. Matsuyama T, Matsushita M (1993) Fractal morphogenesis by a bacterial cell population. *Crit Rev Microbiol* 19:117–135
70. Ben-Jacob E, Cohen I, Gutnick DL (1998) Cooperative organization of bacterial colonies: from genotype to morphotype. *Annu Rev Microbiol* 52:779–806
71. Sawada Y, Dougherty A, Gollub JP (1986) Dendritic and fractal patterns in electrolytic metal deposits. *Phys Rev Lett* 56:1260–1263
72. Grier DG, Ben-Jacob E, Clarke R, Sander LM (1986) Morphology and microstructure in electrochemical deposition of zinc. *Phys Rev Lett* 56:1264–1267
73. Kuhn A, Argoul F (1995) Diffusion-limited kinetics in thin-gap electroless deposition. *J Electroanal Chem* 397:93–104
74. Trigueros PP, Claret J, Mas F, Sagués F (1991) Pattern morphologies in zinc electrodeposition. *J Electroanal Chem* 312:219–235
75. Garik P, Barkey D, Ben-Jacob E, Bochner E, Broxholm N, Miller B, Orn B, Zamir R (1989) Laplace- and diffusion-field-controlled growth in electrochemical deposition. *Phys Rev Lett* 62:2703–2706
76. Matsushita M, Sano M, Hayakawa Y, Honjo H, Sawada Y (1984) Fractal structures of zinc metal leaves grown by electrodeposition. *Phys Rev Lett* 53:286–289
77. Hurd AJ, Schaefer DW (1985) Diffusion-limited aggregation in two dimensions. *Phys Rev Lett* 54:1043–1046
78. Nakanishi S, Fukami K, Sakai SI, Nakato Y (2002) New autocatalytic mechanism for metal electrodeposition leading to oscillations and fern-leaf-shaped deposits. *Chem Lett (Japan)* 31:636–637
79. Fukami K, Nakanishi S, Sakai SI, Nakato Y (2003) Mechanism of oscillatory electrodeposition of zinc, revealed by microscopic inspection of dendritic deposits during the oscillation. *Chem Lett* 32:532–533
80. Fukami K, Nakanishi S, Tada T, Yamasaki H, Fukushima S, Sakai SI, Nakato Y (2005) Self-organized periodic growth of stacked hexagonal wafers in synchronization with a potential oscillation in zinc electrodeposition. *J Electrochem Soc* 152:C493–C497
81. Nakanishi S, Fukami K, Tada T, Nakato Y (2004) Metal latticeworks formed by self-organization in oscillatory electrodeposition. *J Am Chem Soc* 126:9556–9557
82. Tada T, Fukami K, Nakanishi S, Yamasaki H, Fukushima S, Nagai T, Sakai SI, Nakato Y (2005) Tuning of the spacing and thickness of metal latticeworks by modulation of self-organized potential oscillations in tin (Sn) electrodeposition. *Electrochim Acta* 50:5050–5055
83. Fukami K, Nakanishi S, Yamasaki H, Tada T, Sonoda K, Kamikawa N, Tsuji N, Sakaguchi H, Nakato Y (2007) General mechanism for the synchronization of electrochemical oscillations and self-organized dendrite electrodeposition of metals with ordered 2D and 3D microstructures. *J Phys Chem C* 111:1150–1160

84. Kuroda T, Irisawa T, Ookawa A (1977) Growth of a polyhedral crystal from solution and its morphological stability. *J Cryst Growth* 42:41–46
85. Oaki Y, Imai H (2003) Experimental demonstration for the morphological evolution of crystals grown in gel media. *Cryst Growth Des* 3:711–716
86. Nakanishi S, Sakai S, Nishimura K, Nakato Y (2005) Layer-by-layer electrodeposition of copper in the presence of *o*-phenanthroline, caused by a new type of hidden NDR oscillation with the effective electrode surface area as the key variable. *J Phys Chem B* 109:18846–18851
87. Rosso M, Gobron T, Brissot C, Chazalviel JN, Lascaud S (2001) Onset of dendritic growth in lithium/polymer cells. *J Power Sources* 97–98:804–806
88. González G, Rosso M, Chassaing E, Chazalviel JN (2007) Experimental and theoretical study of the onset of the growth of an irregular metal electrodeposit. *Electrochim Acta* 53:141–144
89. Chazalviel JN (1990) Electrochemical aspects of the generation of ramified metallic electrodeposits. *Phys Rev A* 42:7355–7367
90. Nakanishi S, Sakai S, Nagai T, Nakato Y (2005) Macroscopically uniform nanoperiod alloy multilayers formed by coupling of electrodeposition with current oscillations. *J Phys Chem B* 109:1750–1755
91. Sakai S, Nakanishi S, Nakato Y (2006) Mechanisms of oscillations and formation of nano-scale layered structures in induced co-deposition of some iron-group alloys (Ni–P, Ni–W, and Co–W), studied by an in situ electrochemical quartz crystal microbalance technique. *J Phys Chem B* 110:11944–11949
92. Ihara D, Nagai T, Yamada R, Nakanishi S (2009) Interfacial energy gradient at a front of an electrochemical wave appearing in CuSn-alloy oscillatory electrodeposition. *Electrochim Acta* 55:358–362
93. Zeiri L, Efrima S, Deutsch M (1996) Interfacial electrodeposition of silver: the role of wetting. *Langmuir* 12:5180–5187
94. Zeiri L, Efrima S (1997) Ac driven interfacial electrodeposition of silver. *Langmuir* 13:4722–4728
95. Zeiri L, Efrima S, Deutsch M (1997) Electroaggregation of silver interfacial colloids. *J Phys Chem B* 101:9757–9766
96. Zeiri L, Younes O, Efrima S, Deutsch M (1997) Interfacial electrodeposition of silver. *J Phys Chem B* 101:9299–9308
97. Wagner C (1954) Contribution to the theory of electropolishing. *J Electrochem Soc* 101:225–228
98. Efrima S (1997) Morphology of quasi-two dimensional electrodeposits—a generalized Wagner number. *Langmuir* 13:3550–3556
99. Nakabayashi S, Aogaki R, Karantonis A, Iguchi U, Ushida K, Nawa M (1999) Two-dimensional metal deposition at the liquid–liquid interface; potential and magnetohydrodynamic pattern transition. *J Electroanal Chem* 473:54–58
100. Nakanishi S, Nagai T, Fukami K, Sonoda K, Oka N, Ihara D, Nakato Y (2008) Oscillatory electrodeposition of metal films at liquid/liquid interfaces induced by the large surface energy of growing deposits. *Langmuir* 24:2564–2568
101. Tada E, Oishi Y, Kaneko H (2007) Electrochemical oscillation during electrodeposition of zinc at the interface between two immiscible liquids. *Electrochemistry (Japan)* 75:731–733
102. Saliba R, Mingotaud C, Argoul F, Ravaine S (2002) Spontaneous oscillations in gold electrodeposition. *Electrochem Commun* 4:629–632
103. Fukami K, Nakanishi S, Sawai Y, Sonoda K, Murakoshi K, Nakato Y (2007) In situ probing of dynamic nanostructural change of electrodeposits in the course of oscillatory growth using SERS. *J Phys Chem C* 111:3216–3219
104. Lublow M, Lewerenz HJ (2009) Scaling effects upon fractal etch pattern formation on silicon photoelectrodes. *Electrochim Acta* 55:340–349

Self-Organization in Electrochemical Systems II  
Spatiotemporal Patterns and Control of Chaos

Orlik, M.

2012, XX, 448 p., Hardcover

ISBN: 978-3-642-27626-2